Flow Losses in Supersonic Compressor Cascades

by

Gregory S. Bloch

Dissertation submitted to the Faculty of the

Virginia Polytechnic Institute and State University

in partial fulfillment of the requirements for the degree of

DOCTOR OF PHILOSOPHY

in

Mechanical Engineering

APPROVED:

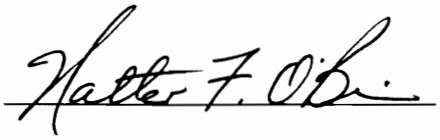

W. F. O'Brien, Chairman

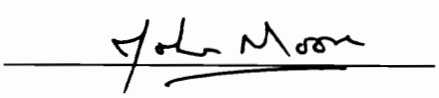

J. Moore

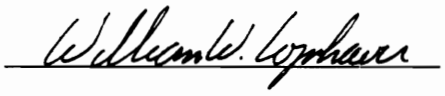

W. W. Copenhaver

C. L. Dancey

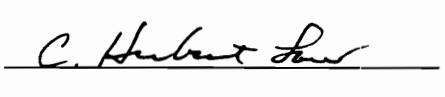

C. H. Law

July 1996

Blacksburg, Virginia

Key words: Compressor, Cascade, Shock, Loss, Model

Flow Losses in Supersonic Compressor Cascades

by

Gregory S. Bloch

W. F. O'Brien, Chairman

Mechanical Engineering

(ABSTRACT)

Loss models used in compression system performance prediction codes are often developed from the study of two-dimensional cascades. The physical mechanisms that affect the flow in supersonic compressor cascades have been reviewed, including the changes in shock geometry that will occur with back pressure for both started and unstarted operation. Compressible fluid mechanics has been applied to the known shock geometry to obtain a physics-based engineering shock loss model that is applicable over the entire supersonic operating range of the cascade.

Predictions from the present method have been compared to measurements and Navier-Stokes analyses of the L030-4 and L030-6 cascades, and very good agreement was demonstrated for unstarted operation. Some of the started comparisons exhibited good agreement, while others did not. A clear improvement has been demonstrated over previously published shock loss models, both in the accuracy of the predictions and in the range of applicability.

The dramatic increase in overall loss with increasing inlet flow angle is shown to be primarily the result of increased shock loss, and much of this increase is caused by the detached bow shock. For a given Mach number, the viscous profile loss is nearly constant over the entire unstarted operating range of the cascade, unless a shock-induced

boundary layer separation occurs near stall. Shock loss is much more sensitive to inlet Mach number than is viscous profile loss.

The present shock loss model has been used as the basis of an overall loss prediction method by adding a constant value, representative of the viscous profile loss, to the predicted shock loss characteristics. The overall loss characteristics obtained in this manner showed good agreement with the experimental values over the most useful operating range of the cascade.

Acknowledgments

The author wishes to thank the members of his Ph.D. advisory committee for their contributions to the present investigation. In particular, Walt O'Brien and Bill Copenhaver are recognized for their continuous advice and direction, and John Moore for obtaining the overall performance results for the L030 cascade experiments.

All of the members of the Compressor Aerodynamics Research Lab team have also made important, though often unsung, contributions to the present effort. Some of this assistance has been in the form of technical discussions, and some has been computer systems support. While it is not possible to recognize each of these contributions individually, it is clearly stated that this dissertation could not have been completed without them.

Rod Chima of the NASA Lewis Research Center is recognized for providing the quasi-3-D Navier-Stokes solver used in the present investigation, for explanation of the appropriate boundary conditions, and for general advice on interpretation of the solutions. Gratitude is also expressed to Dan Tweedt of NASA Lewis for some fairly lengthy discussions on the difficult nature of supersonic compressor cascade testing and the limitations of these test results.

Heinz-Adolf Schreiber of the DLR has provided the measured blade coordinates from the L030 cascade tests. While these are available in the published literature, the electronic transfer of these coordinates allowed the author to avoid the tedious and error-prone process of typing them in by hand.

The U.S. Air Force has provided financial support for the present research program. The author wishes to thank the Palace Knight program office in particular, and the millions of U.S. taxpayers in general.

The author owes an especially large debt of gratitude to his parents for all of the support they have provided over the years. It is truly amazing how much smarter they have become since the author's teenage years.

Most importantly, however, the author thanks his wife for taking care of everything and tolerating his absence during the seeming eternity taken to complete this dissertation.

Table of Contents

List of Figures

List of Tables

List of Symbols

a chordwise location of maximum suction surface velocity
constant in various equations

A area

$AVDR$ axial velocity density ratio, $\Omega = \dfrac{\rho_2 V_{x2}}{\rho_1 V_{x1}}$

b constant used in various equations

c blade chord
constant in various equations

c_p specific heat at constant pressure

d constant used in various equations

D diffusion factor (sometimes called the D-factor)

DCA double circular arc

D_{eq} equivalent diffusion ratio

h effective blade height

H boundary layer form factor, $H = \delta^*/\theta$

i incidence angle
axial location of an arbitrary downstream measuring plane

I momentum

IGV inlet guide vane

k boundary layer pseudo-energy thickness

K boundary layer pseudo-energy factor, $K = k/\theta$
constant used in calculation of equivalent diffusion ratio (Koch and Smith, 1976)

LER leading edge radius

$\dot{m}$ mass flow

M Mach number

MCA multiple circular arc

n	exponent in boundary layer velocity profile
N	number of blades
P	pressure
r	radius
R	ideal gas constant
s	blade spacing entropy
t	blade thickness
T	temperature
U	wheel speed
V	absolute velocity
W	relative velocity
x	axial coordinate
y	cascade coordinate normal to axial in the blade-to-blade direction

GREEK SYMBOLS

α angle of attack

β flow angle

δ boundary layer thickness

δ^* boundary layer displacement thickness

ε angle through which flow is turned by passing through an oblique shock

γ ratio of specific heats

Γ blade row circulation

φ angle between the meridional flow direction and the axial direction

μ Mach angle, $\mu = \sin^{-1}(1/M)$

ν Prandtl-Meyer function

θ boundary layer momentum thickness

ρ density

σ cascade solidity, *c/s*
contraction ratio required to decelerate a supersonic stream to sonic velocity isentropically

τ shear stress

ω rotational speed, rad/sec
local total pressure loss coefficient, $\omega_2 = \dfrac{P_{01} - P_{02}}{P_{01} - P_1}$

$\overline{\omega}$ mass-averaged total pressure loss coefficient, $\overline{\omega}_2 = \dfrac{P_{01} - \overline{P}_{02}}{P_{01} - P_1}$

Ω axial velocity density ratio, $\Omega = \dfrac{\rho_2 V_{x2}}{\rho_1 V_{x1}}$

$\overline{\Omega}$ mass-averaged total pressure loss coefficient, alternative form

ψ angle between shock surface and upstream flow ($\psi = 90°$ for normal shock)

SUBSCRIPTS

a	annulus
A	conditions along the first captured Mach wave
avg	average
c	mass centroid of flow passing the sonic line in Moeckel (1949) detached shock model
ch	choked, choking
cr	critical condition (from isentropic expansion or deceleration to sonic velocity)
fs	free stream
i	arbitrary measuring plane, 0 to 1.5 chords downstream of the blade trailing edge
LE	blade leading edge
m	mean meridional
max	maximum corresponds to shock angle which produces maximum flow deflection
ps	edge of wake on pressure side of blade
ss	edge of wake on suction side of blade
R	rotor relative frame
s	conditions along sonic line in Moeckel (1949) detached shock model
S	stator
sb	location of sonic point on the body in Moeckel (1949) detached shock model
te	trailing edge
th	throat
x	axial direction
y	normal to the axial direction

θ	tangential direction
0	total property
1	inlet station
2	exit station station downstream of weak passage shock, but upstream of normal shock (for started operating conditions)
3	station downstream of normal shock (for started operation)

EMBELLISHMENTS

*	at minimum-loss incidence
$'$	relative to the blade
$''$	corrected for inlet Mach number
$\bar{}$	mass-averaged quantity

1. Introduction

A successful aircraft gas turbine engine must be lightweight, compact, fuel efficient, reliable, and cost-effective. Clearly, an improvement in one area can cause a penalty in another and acceptable tradeoffs are mission dependent. Engine weight can be reduced, for example, through the use of advanced composite materials which will increase the purchase price of the engine. For long-range commercial transports such as the Boeing 747, which spend roughly 3/4 of their service life in the air, an increase in purchase cost might be acceptable if it provides a corresponding increase in fuel efficiency. For regional transports, which spend significantly less time in the air and have a significantly shorter service life, initial purchase price is far more critical than marginal improvements in fuel consumption. For a military fighter, increased cost and fuel consumption might be acceptable if they provide a sufficient increase in thrust for a fixed engine size.

These tradeoffs must be evaluated, however, at the multiple operating conditions which comprise a complete mission. Operation of the fan of a bypass engine serves as an example. Upon initial startup and while taxiing before takeoff, the engine is operating near the idle condition, labeled point *A* on the fan map shown in Figure 1. For takeoff and the climb-out portion of the flight, maximum thrust is required and the engine operating point will be near point *B*. Once cruise altitude and speed have been obtained, the pilot will throttle back to a flight cruise condition near point *C*. For approach, landing, and taxiing on the ground, the engine will again operate near idle.

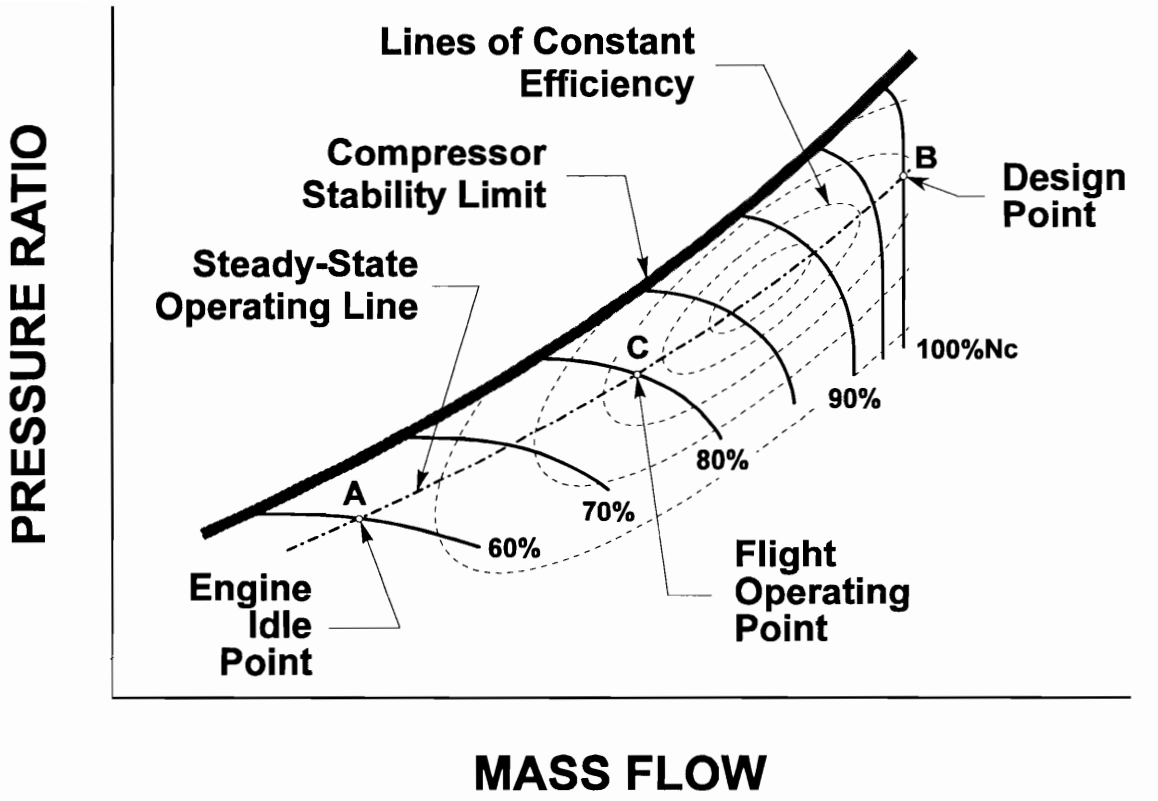

Figure 1. Typical transonic fan performance map

For each portion of the mission, it is clearly desirable to operate at the maximum possible efficiency condition. This desire to obtain high efficiency, however, must be moderated by the requirement to maintain adequate stall margin. Employing a compressor as an example, if the engine is operating at point *D* shown in Figure 2, and the pilot requests an increase in power, the engine control system will increase the fuel flow to the combustor. Initially, this increased fuel flow will be seen by the compressor as an increase in back pressure and the operating point will shift along a constant speedline up to point *E*. As the inertia of the engine is overcome by the increased power setting, the rotational speed of the engine will increase and the operating point will progress along the transient operating line to the desired operating point *F*.

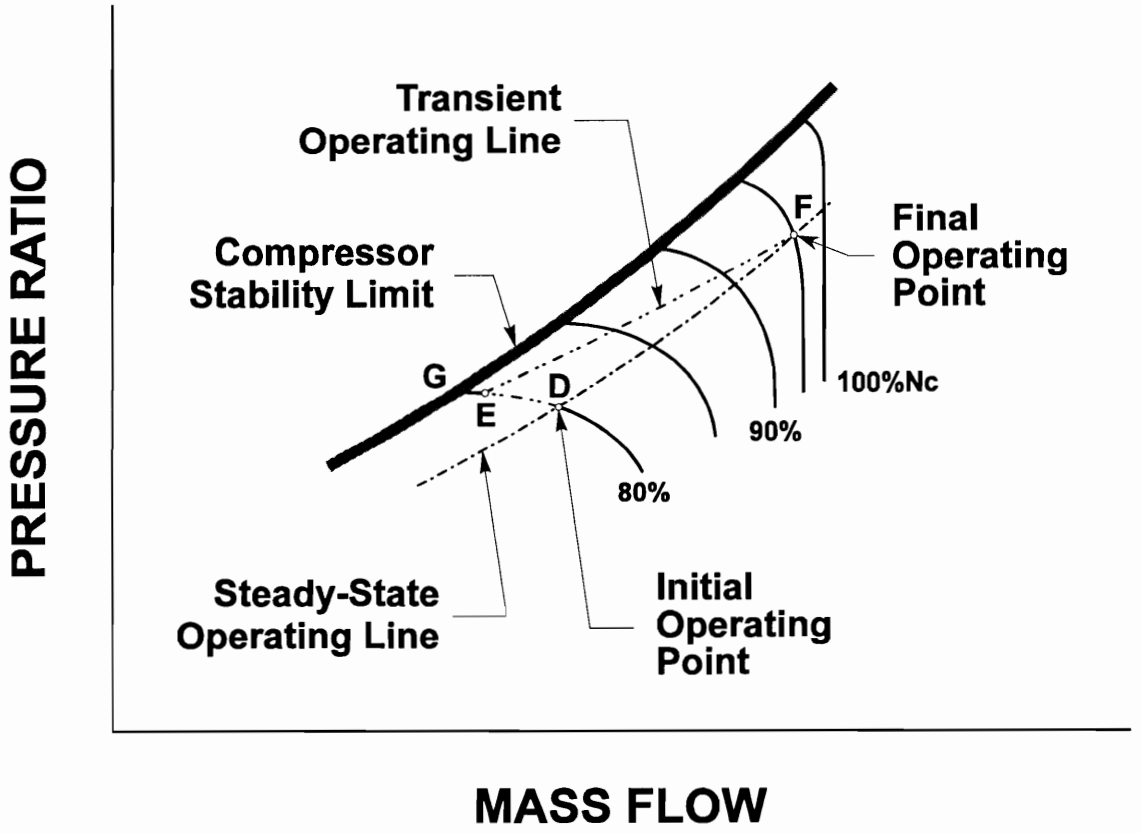

Figure 2. Engine response to a step increase in fuel flow

If the initial operating point *D* is too close to the stability limit, meaning the engine has insufficient stall margin, the increase in fuel flow will result in undesirable operation. As the mass flow decreases below the value at the stability limit point *G*, the compression system will either surge or stall and the blade stresses will increase dramatically. These increased stresses can induce rapid and catastrophic compression system failure, and these operating modes must be avoided.

To allow engineers to assess these and other performance tradeoffs, thermodynamic cycle and mission analyses such as those of Mayhew and Eisenhauer (1995) are conducted early in the design process. Global engine parameters such as mass

flow, bypass ratio, component pressure ratios, and component efficiencies are determined from these studies and it is then required of the component designers to perform successful detailed designs to meet these objectives.

Having thus established the basic size and speed parameters, the detailed aerodynamic compressor design process begins with the specification of a design-point flow field that the engineer thinks will meet the performance objectives. A streamline curvature method of solution of the equations of fluid motion is then used to determine the initial blading design. These methods assume the flow to be axisymmetric and inviscid, and the effects of entropy generation are included as total pressure losses determined from loss models (Lieblein, 1954; Novak, 1967; Law and Puterbaugh, 1982).

Because this technique is simple, inexpensive, and fast, it is currently used to make the fundamental engineering decisions such as the number of stages and blades, and to eliminate unacceptable options early in the design process. But the streamline curvature methods assume axisymmetric flow, and a blade shape generated in this manner must subsequently be analyzed with a CFD code to look for unfavorable 3-D and viscous flow effects. If improvements are required, both the streamline curvature and the Navier-Stokes analyses are repeated.

The use of streamline curvature methods to determine the blade shape required to generate a desired flow field is often referred to as "design mode." The use of this terminology is partly because this is the process in which the actual blade shape is specified, and partly because only the design-point operation is considered. Once blading which will produce suitable design-point behavior has been established, the off-design

operation of the compressor must be analyzed separately to ensure that sufficient stall margin will be available.

Streamline curvature methods can be used in what is often referred to as "analysis mode" to estimate the performance of a known blade shape. In this mode, each blade in the compressor is divided into a number of radial segments or stream tubes, and the performance of each of these segments in the relative frame is calculated as though it were an isolated, 2-D cascade section. The performance of each of these blade elements is then stacked in the radial direction to obtain the performance of the entire bladerow. CFD techniques are also used extensively to predict off-design performance. If unsuitable off-design performance is indicated for a candidate blade shape, the entire design cycle must be repeated.

This iterative process typically examines only the design-point and near-stall performance (Koch, 1994) for 2 main reasons. The most important reason from a business perspective is that there are typically contractual requirements for design-point performance and stall margin, with significant financial penalties for failure to meet the specifications. The second reason is that the streamline curvature methods are currently unable to predict off-design performance accurately, and the more expensive CFD techniques must be used.

It has been suggested that the use of streamline curvature methods should be abandoned in favor of Navier-Stokes codes (Denton, 1994), but this view is not universally shared. While a direct numerical solution of the Navier-Stokes equations can yield a very detailed qualitative description of the flow field for a known geometry, there

are still several limitations to the use of CFD in the design process. Navier-Stokes methods are quite expensive in terms of computer resources and time required for solution, and are currently unable to predict losses accurately. The inability to accurately quantify loss is a direct result of a poor fundamental understanding of turbulence and boundary layer transition, and this situation is not expected to improve in the near future (Casey, 1994b; Denton, 1993; Vuillez and Petot, 1994; Jennions, 1994). Also, such methods are not presently used in an inverse mode to provide the blade shape required to generate a desired flow field. In spite of these disadvantages, CFD is used extensively to obtain designs which operate closer to the physical separation and choking limits of the machine, and to reduce development time, expense, and risk. But, these are optimizations performed on a preliminary design which was obtained by streamline curvature methods.

It is generally accepted that streamline curvature methods will provide a satisfactory prediction of compressor performance as long as the losses and blockage are predicted accurately. As a result, it is expected that the use of these tools in the design process will continue for many years. Since these tools will continue to be used, the need for improvements in loss modeling to support them is widely agreed (Koch, 1995; Dunham, 1995; Casey, 1994a).

Historically, each major improvement in turbomachinery performance has been achieved by incorporating an improved predictive tool into the design process. The most successful of these have been mathematical models which express in quantitative terms an improved physical understanding of the fluid flow phenomena (Dunham, 1995).

Indeed, it is hard to imagine how an engineer will be able to improve a design without a firm grasp of the physical reasons underlying what the codes predict. The most prudent approach to improving turbomachinery performance begins with the development of a better physical understanding of the loss mechanisms. That understanding should then be expressed as mathematical models capable of quantifying the entropy generation of the fluid flow processes. Those models, once validated against experiments, can then be used to suggest improvements.

To obtain the desired level of performance, virtually all modern aircraft gas turbine engine fans employ transonic blading. For the first stage fan rotor, the axial component of the design-point inlet flow is in the high subsonic range, up to 0.9 for aggressive designs. The relative flow is supersonic at the blade tip, as high as 1.6 for aggressive designs, and is subsonic at the hub. The actual flow field inside this class of turbomachine is viscous, compressible, unsteady, 3-dimensional, and has both laminar and turbulent regions. Some simplifying assumptions clearly must be made to obtain an analytical solution of the Navier-Stokes equations, and the accuracy of that solution will depend on the validity of the assumptions made. Because few assumptions will hold for all well-designed machines, and the appropriate assumptions are not intuitively obvious, loss models use simplified theory and are highly empirical.

Typically, a given loss model will consider a single mechanism and neglect the effects of all others. The appropriate equations are then simplified based on either geometric considerations or the anticipated relative magnitudes of the terms, and correction factors are included to adjust the remaining terms. In transonic fans and

compressors, losses are produced by endwall and blade boundary layers, shocks, tip-leakage flows, secondary flows, and interactions among them, as shown in Figure 3. Although the models for these effects tend to be quite simplified, the design-point models include empirical data from corporate experience, and the design-point predictions tend to be accurate within 1 or 2 percent as long as the new design does not stray very far from the existing design base (Casey, 1994a).

The off-design flow field, however, is far less "well-behaved" than at the design point and the assumptions made in the design-point models no longer hold. Use of the

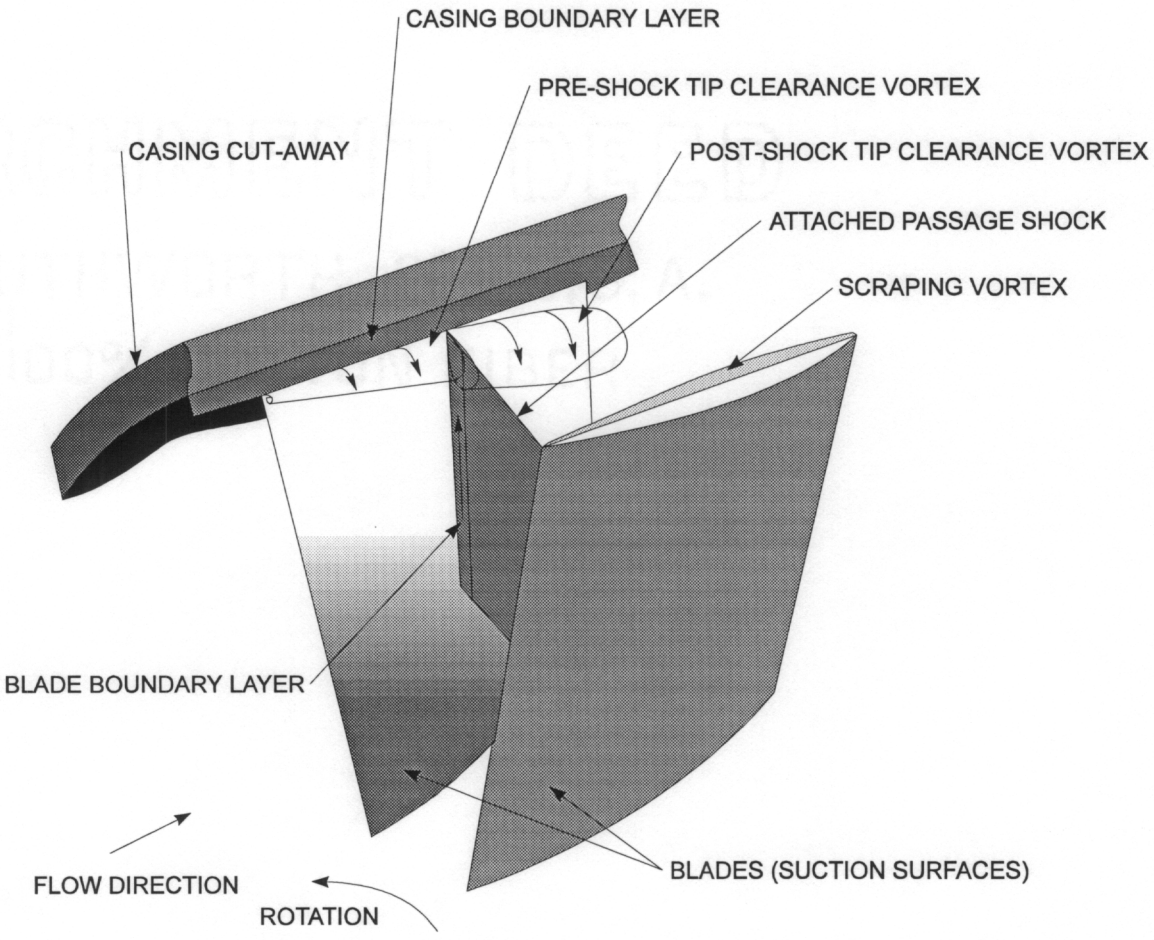

Figure 3. Loss sources in a transonic compressor (Puterbaugh, 1994)

design-point models to predict off-design performance would yield unreliable results. As a result, typical off-design models are simple correlations which mimic the anticipated trends, instead of fundamentally-based models which capture the actual flow physics. While application of these models can estimate low-speed operation with sufficient accuracy, as shown in Figure 4, performance is predicted poorly in the transonic regime.

To ensure meeting overall aircraft mission requirements, engine cycle analysis programs must be used to perform mission analyses, engine operability studies must be

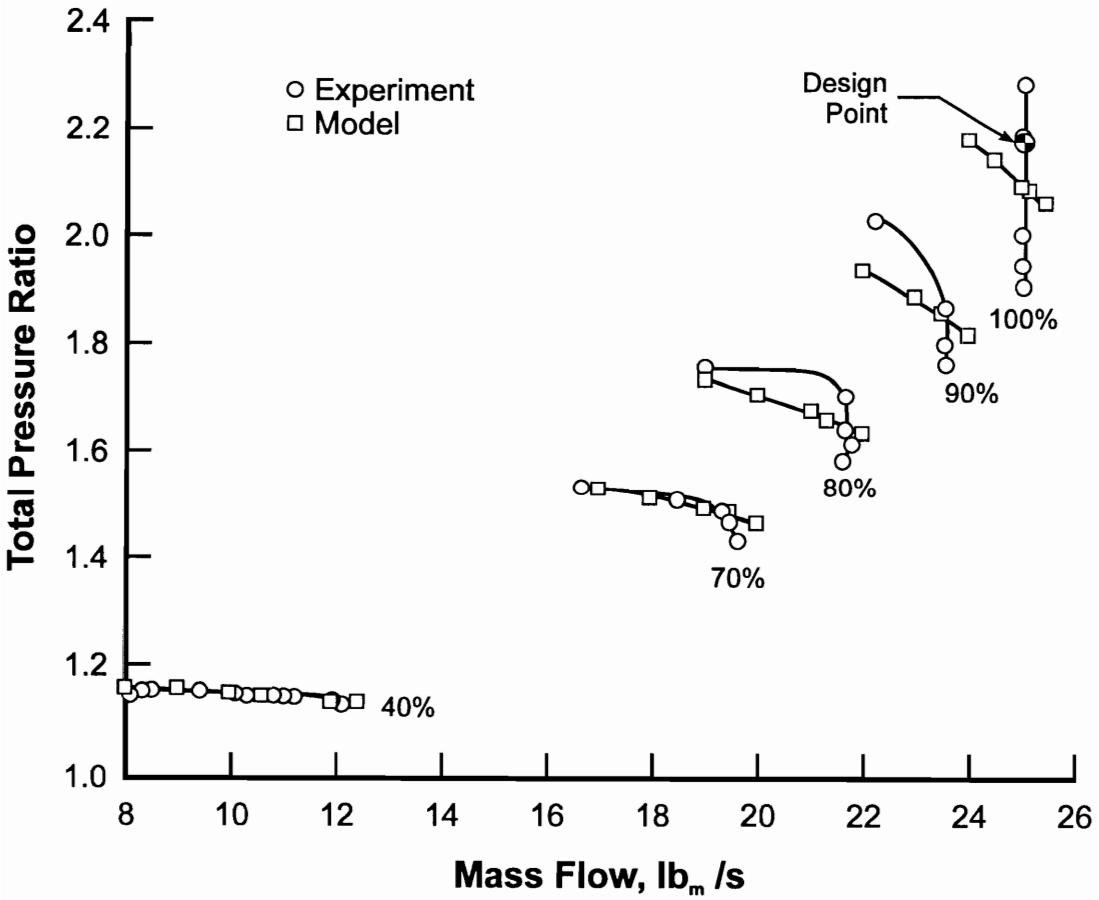

Figure 4. Measured performance for first stage of a 3-stage transonic compressor compared with predictions using Lieblein (1957) profile loss model and Miller, Lewis, and Hartmann (1961) shock loss model

performed, and engine control logic must be developed *before* the compression system hardware is tested. For each of these endeavors, the accuracy of the stage characteristics used as inputs to the prediction methods is critical if one is to obtain meaningful information about engine performance (Saravanamutto and Fawke, 1970; Boyer and O'Brien, 1989; Dowler, et al., 1989; Davis and O'Brien, 1991). Therefore, the ability to meet overall propulsion system goals hinges on the ability to generate accurate off-design compressor stage characteristics rapidly, reliably, and early in the design cycle.

Ultimately, it would be desirable to have the ability to generate the entire compressor map from first principles so that a design could be optimized for maximum part-speed efficiency. Since this is where most man-rated engines spend the majority of their operating lives, this is where the largest benefit to the customer will be obtained. To realize this objective, the compressor designer must have the capability to perform accurate part-speed performance calculations faster and cheaper than is currently possible with CFD codes. These part-speed performance calculations can be made with a streamline curvature method, but an improved understanding of the physical mechanisms will be required to improve the loss models to the point where reliable estimates are obtained.

The logical first step in the direction of improved off-design performance predictions is to develop a loss model which is applicable along the entire design speedline, from stall to choking. Because the existing low-speed loss models give satisfactory predictions, the scope of the current investigation will be restricted to the portion of the rotor flow field in which the relative flow is supersonic. Because the rotor

tip-region flow field was the subject of a separate research program (Puterbaugh, 1994), the scope of the current investigation will be further restricted to that portion of the flow field in which the influence of the tip-leakage flow is small. The region of applicability of the model to be developed in this dissertation, therefore, is outboard of the sonic line and inboard of the tip leakage flow. This is shown as the lightly shaded region in Figure 5, and is referred to as the "free-stream supersonic region." In the current context, this term is used to refer to the radial direction, not the blade-to-blade direction.

As mentioned previously, the flow field inside a transonic compressor is extremely complex, and there are multiple interactions among the various loss-producing mechanisms. It is generally recognized that these interactions are an inseparable part of

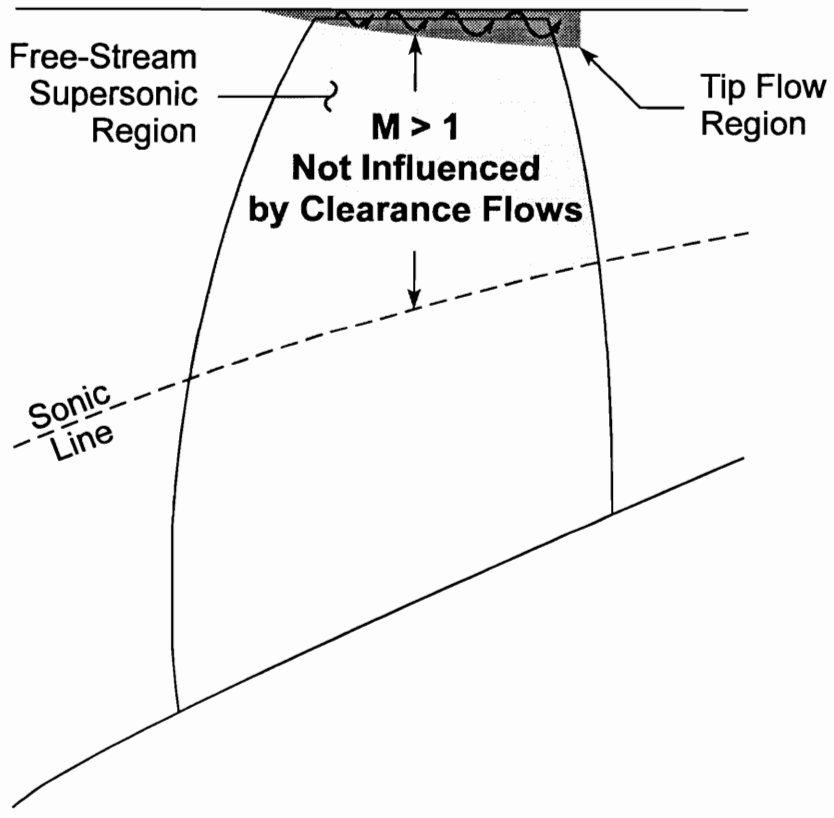

Figure 5. Region of applicability of current investigation

the actual flow structure and that the performance of the entire machine will not be obtained exactly by summing the performance of the isolated mechanisms. It is beyond the state of the art to quantify the effects of most of these interactions, however, and research efforts often focus on a single mechanism as though none of the other components were present. For this reason, much of the research in the turbomachinery field has been conducted on stationary, 2-D cascades to better isolate the particular mechanism or combination of mechanisms under consideration. Once the mechanism is understood in the cascade environment and a model has been developed and validated, that model can then be used in the design and analysis of actual fans and compressors.

This dissertation will improve the fundamental understanding of flow phenomena which exist in transonic compressors operating along the design speedline, although that understanding will be developed from an investigation of the flow in 2-D cascades. The physics of the situation will then be applied to suggest a fundamentally-based method for quantifying entropy production during peak-efficiency and off-design operation.

2. Literature Review

For the portion of the rotor flow field considered in the present investigation, it is widely accepted that both the passage shock and the blade boundary layers contribute significantly to the overall loss (Denton, 1993). Unfortunately, the author knows of no publication in the open literature in which the relative magnitudes of these contributions is demonstrated. Lacking any rational guidance to suggest otherwise, this leaves little choice but to review the literature for both mechanisms and attempt to discern afterwards which course to pursue.

During the course of this review, the major details of the analyses have been reproduced instead of just the summaries. While this may appear at first glance to be beyond what is necessary, it was done intentionally to demonstrate the restrictions on applicability of the various models. It is the author's opinion that the restrictions on the applicability of a model are equally as important as the model itself, and are quite often overlooked. Furthermore, inclusion of the limitations of the various approaches tends to give a certain level of insight into how much effort might be required to improve the models.

The detailed reviews are organized into a section on profile loss models and one on shock models. Each section begins with the publications which are generally regarded as the classical foundations in the field, and the later works are reviewed chronologically.

2.1 Profile Loss Models

The experimental foundation for the classical profile loss models was the low-speed cascade work of Herrig, et al. (1951). In these tests, NACA 65-A_{10} series profiles were tested with an air inlet velocity of approximately 29 m/s (95 ft/s) and a blade chord Reynolds number of approximately 245,000. Two-dimensional flow was achieved by controlling removal of boundary layer air through porous test section side walls so that the downstream static pressure equaled the ideal value corresponding to the turning angle, corrected for the blockage effect of the wake.

To facilitate use of the cascade data for compressor design, tests were made at various combinations of inlet air angle and solidity, β_1-σ. For these tests, the inlet angle was held fixed, and the angle of attack was varied in 2° or 3° increments by changing the stagger angle; hence the cascade geometry was altered. The data were not presented for constant cascade geometry over a range of incidence, so the test results were not directly applicable to off-design analysis.

The selection of the angle of attack designated as "design" for each combination of inlet angle, solidity, and camber was based on the premise that the blade section would be required to operate at Mach numbers near the critical value. By examining the trend of the pressure-distribution shape over the angle of attack range for each cascade combination, design angle of attack was determined to be the inlet air angle for which no peaks in the local velocity on either the suction or pressure surfaces occurred; this was determined to be the optimum for high-speed operation.

Inlet air angle was determined to be the major factor governing operating range; as β_1 increased, useful operating range decreased. Limiting blade loading criteria were not yet well enough understood to allow a single value of a single parameter to be specified for all conditions.

In an effort to establish a limiting blade loading criterion for compressor blades operating at design incidence, Lieblein, et al. (1953) applied the two-dimensional, incompressible boundary layer equation to the flow across a compressor cascade

$$\frac{d\theta}{dx} = \frac{\tau}{\rho V^2} - (H+2)\frac{\theta}{V}\frac{dV}{dx} \tag{1}$$

For incipient separation, the shear stress approaches zero and the form factor approaches a constant value of approximately 2.0 to 2.5. Under these conditions, the rapid growth of the boundary layer is associated predominantly with the velocity gradient, dV/dx, and Equation 1 becomes

$$\frac{d\theta}{dx} \cong \text{constant}\left(-\frac{\theta}{V}\frac{dV}{dx}\right) \tag{2}$$

Lieblein then defined the diffusion factor as a simplified separation criterion

$$D = -\frac{\theta}{V}\frac{dV}{dx} \tag{3}$$

The development up to this point was based on fundamental fluid mechanics, but calculation of the diffusion factor from Equation 3 is not possible without detailed boundary layer information. To allow calculation of this factor during the design phase, the velocity gradient was approximated as linear diffusion between the location of maximum suction surface velocity and the trailing edge. Referring to Figure 6,

$$-\frac{1}{V}\frac{dV}{dx} = -\frac{V_{\max} - V_2}{(1-a)cV_{avg}} \tag{4}$$

where V_{avg} is some average surface velocity between $V_{\max}$ and V_2. By assuming that the location of maximum velocity, a, and the ratio of momentum thickness to chord, θ/c, do

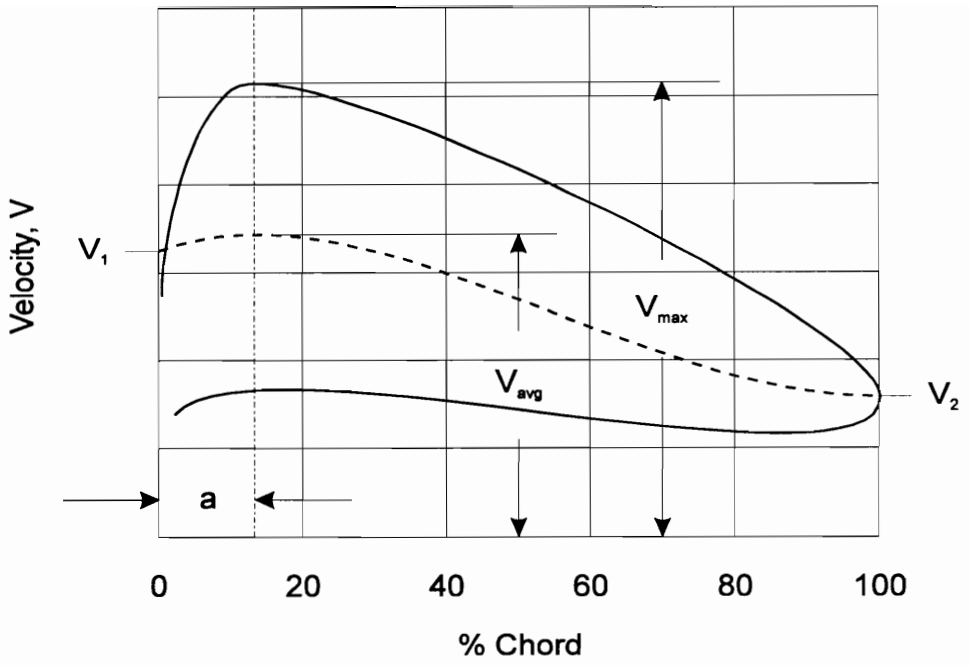

Figure 6. Typical velocity distribution for compressor cascade section near design incidence (Lieblein, 1953)

not change much for "conventional types of blading," meaning NACA 65-A_{10} series blade sections or close variants, then

$$\frac{\theta}{(1-a)c} \cong \text{constant} \tag{5}$$

By ignoring the constant in Equation 5 and approximating V_{avg} by V_1, the diffusion factor can be written as

$$D = \frac{V_{\max} - V_2}{V_1} \tag{6}$$

After examining the cascade pressure distributions of Herrig, et al. (1951), Lieblein, et al. (1953) established a functional relation between the maximum velocity ratio and a circulation parameter which is proportional to the lift coefficient in the form

$$\frac{V_{max}}{V_1} = 1 + b\frac{\Delta V_\theta}{\sigma V_1} + d \tag{7}$$

By selectively neglecting the constants b and d on the grounds that they would be approximately the same for "conventional types of blading," the diffusion factor was reduced to the form

$$D = \left(1 - \frac{V_2}{V_1}\right) + \frac{\Delta V_\theta}{2\sigma V_1} \tag{8}$$

For two-dimensional flow with equal axial velocity at inlet and exit, the diffusion factor becomes

$$D = \left(1 - \frac{\cos\beta_1}{\cos\beta_2}\right) + \frac{\cos\beta_1}{2\sigma}\left(\tan\beta_1 - \tan\beta_2\right) \tag{9}$$

The diffusion factor provided a satisfactory limiting-loading parameter that was clearly defined and was independent of solidity and air inlet angle for NACA 65-A_{10} series blade sections operating at low speeds and design incidence in two-dimensional cascade. The total-pressure loss coefficient increased slightly with diffusion factor, up to a diffusion factor value of approximately 0.6, after which a rapid rise in loss was observed.

The derived diffusion factor was also compared with experimental total-pressure loss coefficients obtained from single-stage axial-flow compressors operating at subcritical Mach numbers and minimum-loss incidence. The minimum loss coefficient

was essentially constant for values of diffusion factor less than 0.6, except at the rotor tip where three-dimensional and tip-clearance effects could not be separated. At the rotor tip, a practically linear variation of loss coefficient with diffusion factor was found to occur for values of diffusion factor greater than about 0.3.

While the development of the diffusion factor as a limiting-loading criterion was a major breakthrough, it was not generally applicable. As stated by the authors, several of the factors which may vary with blade shape, angle of incidence, and inlet Mach number were treated as constants and/or neglected. This treatment precludes application of the derived diffusion factor to off-design operation or to blade shapes that are significantly different from the two-dimensional NACA 65-A_{10} series profiles tested in cascade.

In an effort to extend the NACA diffusion factor to flows with a radial component, Smith (1954) started with Equation 8, but rewrote it in a form better suited to annular cascades. Smith felt that the term $\Delta V_\theta/\sigma V_1$ was more significantly written as Γ/cV_1; this reduces to the former for a two-dimensional cascade or for an annular cascade with a constant radius. For a stationary blade with changing radius

$$\Gamma = \frac{2\pi}{N}\Delta(rV_\theta) \tag{10}$$

By using the solidity at an arithmetic mean radius, Smith obtained (for stators)

$$D_S = \left(1 - \frac{V_2}{V_1}\right) + \frac{\Delta(rV_\theta)}{2\sigma_m r_m V_1} \tag{11}$$

For a rotating blade row, the relative vane circulation was used

$$\Gamma = -\oint \vec{V}\cdot d\vec{x} = -\oint (\vec{W}+\vec{U})\cdot d\vec{x} = \Gamma' - \oint \vec{U}\cdot d\vec{x} = \Gamma' + 2\omega A\sin\varphi \tag{12}$$

where A is the cross-sectional area of the blade. Smith neglected the area term because

the product ωA is much smaller than the other terms and obtained (for rotors)

$$D_R = \left(1 - \frac{W_2}{W_1}\right) + \frac{\Delta(rV_\theta)}{2\sigma_m r_m W_1} \tag{13}$$

Although this extension made the NACA diffusion factor better suited to analyzing the flow within an axial compressor stage, its application is still limited to design-point blade loading of NACA 65-A_{10} series profiles. This profile is a constant loading blade with the location of maximum thickness at approximately 40% chord. When these blades are used at higher Mach numbers, supersonic velocities can occur in the forward region, with resulting shock losses and possible boundary layer separation. The velocities in the forward section of the blade can be reduced by altering either the mean-line shape, the thickness distribution, or both.

Erwin, et al. (1953) conducted low-speed cascade tests on NACA 65-series blades with a systematic variation in mean-line loading. Three variations of the standard NACA 65-A_{10} series profiles were tested, two with the loading shifted toward the rear of the blade and one with the loading shifted even further forward. These tests were conducted to facilitate the selection of blade sections and angles to generate desired compressor design velocity diagrams for higher Mach number operation. It was determined that no "universal" blade profile existed for transonic use and that profile selection was dictated by the design inlet air angle, solidity, camber, and section thickness. As with the results of Herrig, et al. (1951), the data were not presented for constant cascade geometry over a range of incidence, so the test results were not directly applicable to off-design analysis.

In an attempt to gain a better fundamental understanding of the profile loss mechanisms, Stewart (1955) performed an analytical investigation of the compressible-flow loss characteristics of two-dimensional cascades. By assuming that the static

pressure is constant across the blade row exit plane, that the total temperature is constant across the boundary layer, and that the trailing edge velocity profile is given by

$$\frac{V}{V_{fs}} = \left(\frac{y}{\delta}\right)^n \tag{14}$$

Stewart derived equations for the compressible-flow boundary layer characteristics. These characteristics were then used to calculate the compressible-flow loss coefficients for both the blade trailing edge and for flow far downstream, where complete mixing has occurred.

The fully-mixed total-pressure loss coefficient was found to be significantly greater than that at the trailing edge, with the effect even more pronounced at high subsonic and supersonic velocity levels. Because mixing will always occur downstream of the blade row, this effect must be included when describing blade performance characteristics. Increasing the blade trailing-edge thickness was also found to increase the overall loss coefficient significantly, with an additional effect of compressibility existing only for exit flow angles close to axial.

Because the over-all loss coefficient depends directly on the momentum thickness at the blade trailing edge, an accurate evaluation of the trailing edge boundary layer must be obtained for compressible-flow conditions either by experiment or by theory. Because of the difficulty in accurately estimating the boundary layer, the practical application of these results has been limited.

Lieblein and Roudebush (1956a) developed an approach to profile loss modeling that pointed out the relative influence of the various geometric and aerodynamic factors on the resulting loss in total pressure across an incompressible, two-dimensional cascade. By changing the integration path for the boundary layer thickness parameters to be normal

to the cascade axial direction, instead of normal to the flow direction, and designating the parameters by the subscript y, the mass-averaged total pressure loss at an arbitrary exit plane, i, was determined to be (see Figure 7)

$$\Delta\overline{P}_i = \frac{1}{2}\rho V_1^2 \left(\frac{\cos\beta_1}{\cos\beta_i}\right)^2 \frac{\left(\frac{\theta_y}{s}\right)_i + \left(\frac{k_y}{s}\right)_i}{\left[1-\left(\frac{\delta^*_y}{s}\right)\right]^3} \tag{15}$$

where k is the pseudo-energy thickness, $k = \int_{-\delta}^{\delta}\left(1-\frac{V}{V_{fs}}\right)\left(\frac{V}{V_{fs}}\right)^2 dy$

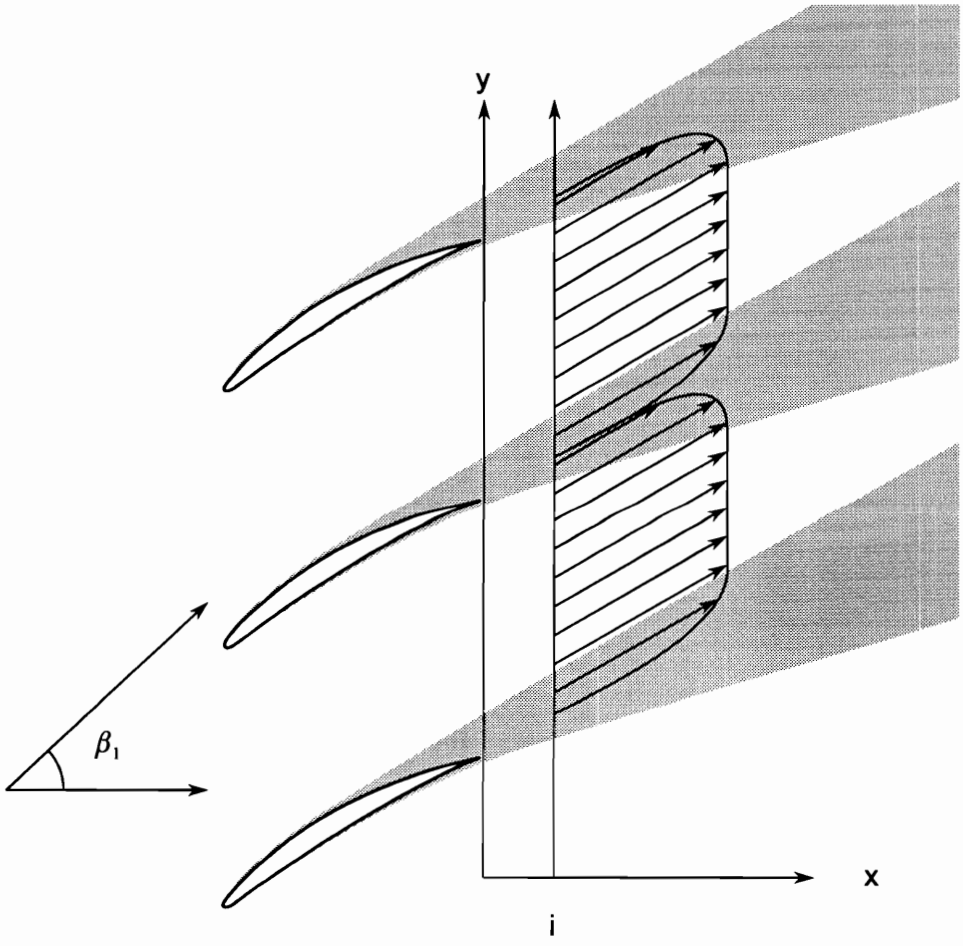

Figure 7. Velocity variation at an arbitrary plane in the wake of a compressor blade row

A convenient method of expressing the loss coefficient then becomes

$$\overline{\Omega}_i = \frac{\Delta \overline{P}_i}{\frac{1}{2}\rho V_1^2}\left(\frac{\cos\beta_i}{\cos\beta_1}\right)^2 = \frac{\left(\frac{\theta_y}{s}\right)_i + \left(\frac{k_y}{s}\right)_i}{\left[1-\left(\frac{\delta_y^*}{s}\right)\right]^3} \tag{16}$$

By further assuming that the axial gradients of flow in the wake are not large, the wake thicknesses in the plane normal to the flow can be related to the thicknesses in the plane normal to the cascade axial by the cosine of the flow angle, β (i.e. $\theta = \theta_y \cos\beta$, etc.), and Equation 16 becomes

$$\overline{\Omega}_i = \left(\frac{\theta}{c}\right)_i \frac{\sigma}{\cos\beta_i} \frac{1+K_i}{\left[1-\left(\frac{\theta}{c}\right)_i \frac{\sigma H_i}{\cos\beta_i}\right]^3} \tag{17}$$

Lieblein and Roudebush (1956a) then investigated the changes in K that would result from assuming different wake velocity profiles. For the 5 representative analytical velocity profiles considered, and for values of $H \leq 1.4$, a maximum difference of less than 1.5% was indicated for the quantity $(1+K)$ and, hence, for $\overline{\Omega}_i$. For simplicity, a power velocity profile of the form of Equation 14 was chosen as representative of the blade wake at a typical cascade measuring station. As a result, the *K-H* relation simplifies to

$$K = \frac{H+1}{3H-1} \tag{18}$$

and the loss coefficient simplifies to

$$\overline{\Omega}_i = 2\left(\frac{\theta}{c}\right)_i \frac{\sigma}{\cos\beta_i} \frac{\frac{2H_i}{3H_i-1}}{\left[1-\left(\frac{\theta}{c}\right)_i \frac{\sigma H_i}{\cos\beta_i}\right]^3} \tag{19}$$

In an effort to relate the loss in an arbitrary cascade measuring plane to the fully-mixed loss coefficient, Lieblein and Roudebush (1956b) studied cascade and isolated airfoil data obtained between the trailing edge and approximately 1 chord downstream to determine the decay of wake characteristics with downstream distance. The measured form factor was found to decrease rapidly with downstream distance and asymptotically approach a value of 1. For measuring planes greater than about ½ chord downstream, the value of the form factor was bounded by $H < 1.2$ for all cases, regardless of its value at the trailing edge. For cascade airfoils, the flow exit angle, β, and the momentum thickness, θ, both increase immediately downstream of the trailing edge, but both become essentially constant beyond about ¼ chord downstream of the trailing edge.

The results of mixing-loss ratio calculations for this range of form factor indicated a rapid increase in total-pressure loss immediately downstream of the trailing edge and that more than 95% of the mixing loss will have occurred within ½ chord of the trailing edge. Total-pressure loss coefficients computed by Equation 19 for cascade measuring planes more than 2% of axial chord downstream of the trailing edge agreed with those determined by direct integration within about $\pm 1\%$ for the available cascade data. From this, Lieblein and Roudebush (1956a) concluded that wake parameters measured at a typical cascade measuring station between ½ and 1 chord downstream of the trailing edge are sufficiently close to the fully-mixed condition to be used for design purposes. After making the appropriate substitutions, the conventional loss coefficient then becomes

$$\overline{\omega}_2 = 2\left(\frac{\theta}{c}\right)_2 \frac{\sigma}{\cos\beta_2}\left(\frac{\cos\beta_1}{\cos\beta_2}\right)^2 \left\{ \frac{\dfrac{2H_2}{3H_2 - 1}}{\left[1 - \left(\dfrac{\theta}{c}\right)_2 \dfrac{\sigma H_2}{\cos\beta_2}\right]^3} \right\} \tag{20}$$

As is clear from Equation 20, the total-pressure loss coefficient is a direct function of the wake momentum thickness ratio and cascade solidity, and a more modest function of the wake form factor and the inlet and outlet air angles. For practicality, Lieblein and Roudebush (1956b) suggested a constant value of $H = 1.08$ be used for calculations, with negligible error. Lieblein (1956) noted that, for this value of form factor, the collection of terms in braces in Equation 20 is essentially secondary, with a magnitude of nearly 1 for conventional unstalled configurations. This allows a simplification to the form

$$\overline{\omega}_2 \cong 2\left(\frac{\theta}{c}\right)_2 \frac{\sigma}{\cos\beta_2}\left(\frac{\cos\beta_1}{\cos\beta_2}\right)^2 \tag{21}$$

Lieblein (1956) concluded that the substitute loss coefficient, $\dfrac{\overline{\omega}_2 \cos^3\beta_2}{2\sigma\cos^2\beta_1}$, provided a more fundamental expression of the basic loss across a blade element than the loss coefficient alone. Examination of Erwin's (1953) data revealed that the above coefficient was well-correlated with the diffusion factor, as shown in Figure 8a. While this figure represents the NACA 65-A_{10} series profiles, similar curves for different blade shapes form the backbone of most compressor design systems currently in use (Hirsch and Denton, 1981; Law, 1994). A loss correlation was also obtained in terms of $\dfrac{\overline{\omega}_2 \cos\beta_2}{2\sigma_1}$, as shown in Figure 8b, but its effectiveness as an indicator of separation was not as good.

While Equation 20 provides great insight into the dominant factors in total-pressure loss generation, its application as a design tool was still hindered by difficulty in predicting the wake momentum thickness. To simplify the application of Equation 20, Lieblein (1957) developed an empirical correlation between the wake momentum thickness and the suction surface velocity diffusion. As was shown in Equation 1, the

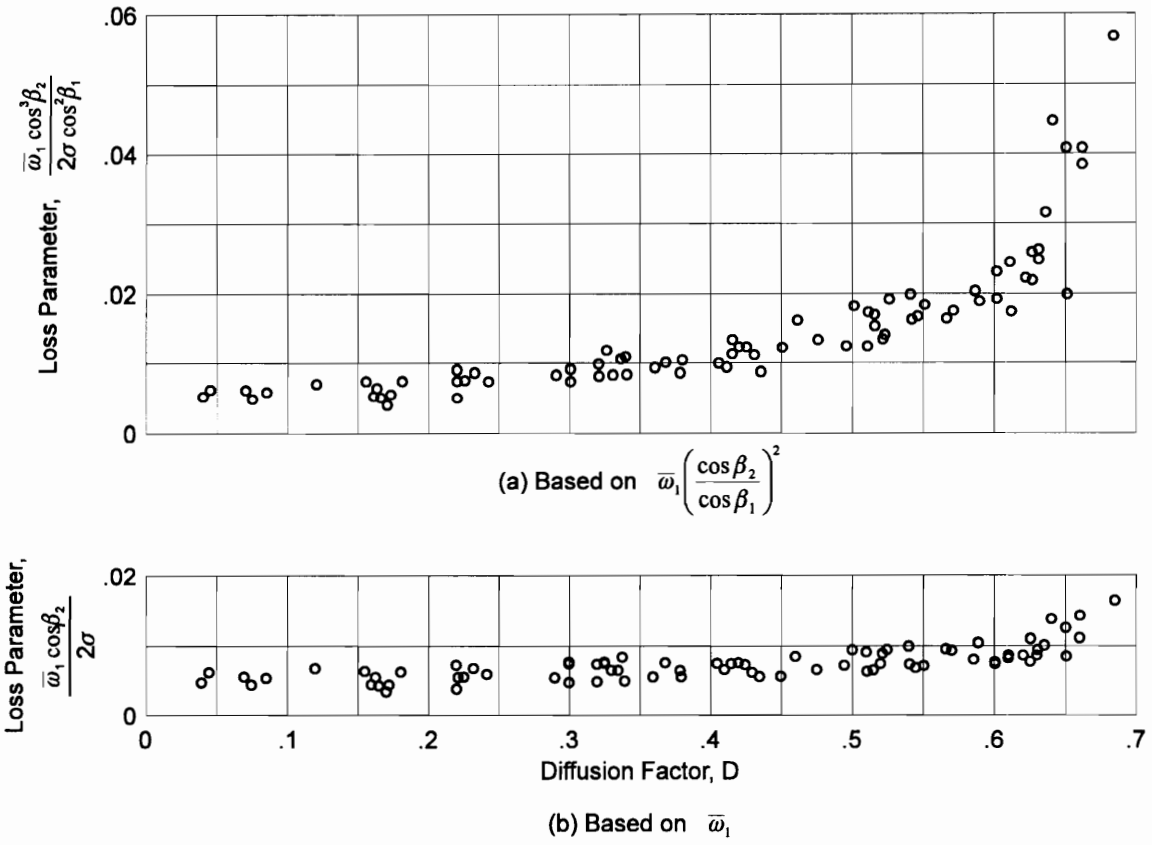

Figure 8. Variation of loss parameters with diffusion factor at minimum loss incidence (Lieblein, 1956)

growth of the boundary layer on a highly-loaded compressor blade is determined predominantly by the velocity gradient, dV/dx. Considering the flow between the location of maximum suction surface velocity and the trailing edge, neglecting the effects of the wakes, the continuity equation for incompressible flow reduces to

$$\frac{V_{\max}}{V_{fs,2}} = \frac{V_{\max}}{V_1}\frac{V_1}{V_{fs,2}} \approx \frac{V_{\max}}{V_1}\frac{\cos\beta_2}{\cos\beta_1} \tag{22}$$

The ratio V_{max}/V_1 was then correlated with a circulation parameter such that, for NACA 65-A_{10} and British C.4 circular arc blades

$$\frac{V_{max}}{V_1} = 1.12 + a\left(\alpha - \alpha^*\right)^{1.43} + 0.61\left(\frac{\cos^2\beta_1}{\sigma}\left(\tan\beta_1 - \tan\beta_2\right)\right) \tag{23}$$

where $a = 0.0117$ for NACA 65-series blades and $a = 0.007$ for C.4 circular arc profiles.

Lieblein (1957) then defined the equivalent diffusion ratio as

$$D_{eq} \equiv \frac{V_{max}}{V_1}\frac{\cos\beta_2}{\cos\beta_1} \approx \frac{V_{max}}{V_{fs,2}} \tag{24}$$

By making the appropriate substitutions, the equivalent diffusion ratio becomes

$$D_{eq} = \frac{\cos\beta_2}{\cos\beta_1}\left[1.12 + a\left(\alpha - \alpha^*\right)^{1.43} + 0.61\frac{\cos^2\beta_1}{\sigma}\left(\tan\beta_1 - \tan\beta_2\right)\right] \tag{25}$$

The data of Herrig, et al. (1951) and of Erwin, et al. (1953) was then examined to determine a correlation between equivalent diffusion ratio and wake momentum thickness. In many cases, the original data showed erratic variations of loss parameter with angle of attack, as shown in Figure 9; these variations were identified as the product of laminar separation. For these cases, Lieblein (1957) estimated the probable variation in loss parameter that would have existed in the absence of the laminar separation and used these faired curves for the comparison.

As can be seen from Figure 10, excellent correlation between the equivalent diffusion ratio and wake momentum thickness was obtained for values of D_{eq} less than 2. Although Figure 10 only includes data for the NACA 65-A_{10} and C.4 profiles, essentially all of the data for the NACA 65-AI series profiles calculated from Equation 25 fell within the band of data shown. Lieblein (1957) concluded that the equivalent diffusion ratio was

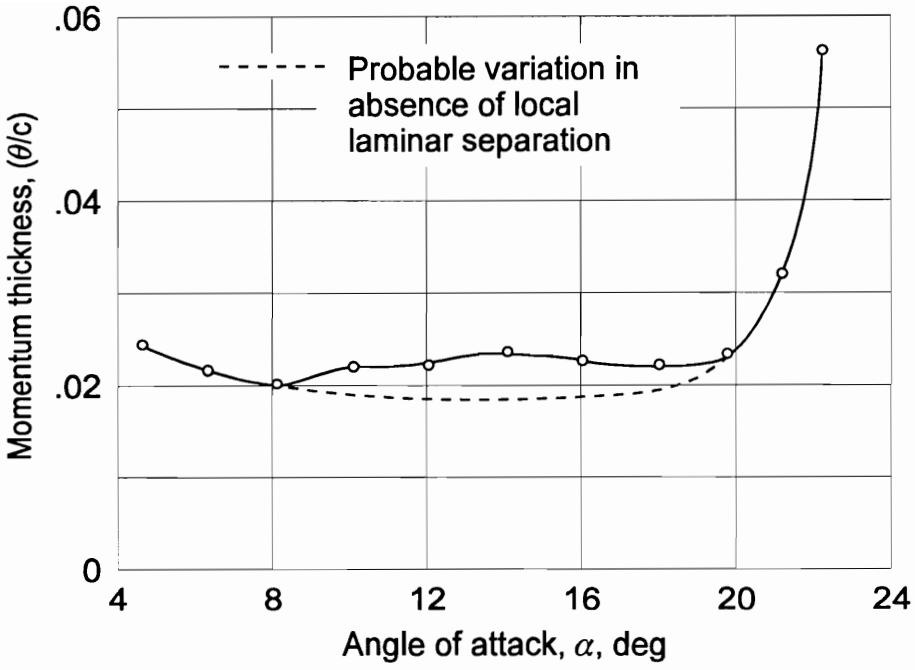

Figure 9. Illustrative variation of momentum thickness in presence of laminar separation

a universal indicator of positive-incidence blade stall for low-speed operation, with a value of D_{eq} greater than 2 indicating stalled flow.

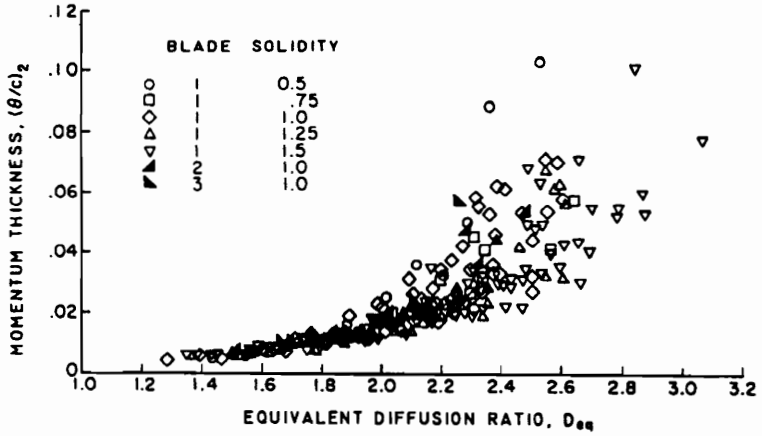

Figure 10. Correlation of wake momentum thickness with equivalent diffusion ratio at angles of attack greater than minimum loss (Lieblein, 1957)

To determine the unstalled operating range of a cascade, Lieblein (1957) assumed that the design incidence was known from the reported cascade data. By iteratively solving Equation 25 until a value of 2 was obtained; the positive-stalling incidence would be obtained. A stalling criterion for negative α stall could not be identified from the published data because pressure surface peak velocities were not considerably greater than suction surface velocities. Lieblein referred to the difference between the design and positive-stall incidence angles as the half-range of the cascade and assumed that the same amount of unstalled range existed on the negative-incidence side of minimum loss, as well.

In an effort to make the equivalent diffusion ratio more directly applicable to compressors, as opposed to cascades, Klapproth (Lieblein, 1959) rewrote the circulation parameter from Equation 23 to include the effects of changing radius and axial velocity

$$\frac{\cos^2\beta_1}{\sigma}\left(\tan\beta_1-\tan\beta_2\right)\equiv\frac{\cos^2\beta_1}{\sigma}\left[\tan\beta_1-\frac{r_2V_{x2}}{r_1V_{x1}}\tan\beta_2-\frac{\omega r_1}{V_{x1}}\left(1-\frac{r_2^2}{r_1^2}\right)\right] \tag{26}$$

Klapproth noted that the change in radius and axial velocity across the blade row would result in a change in the total circulation around the airfoil. By assuming that the resulting velocity distribution is similar to that for an airfoil with an increased camber to produce the same absolute circulation, the equivalent diffusion ratio becomes

$$D_{eq}=\frac{\cos\beta_2}{\cos\beta_1}\frac{V_{x1}}{V_{x2}}\left[\begin{array}{l}1.12+a\left(\alpha-\alpha^*\right)^{1.43}+\\0.61\dfrac{\cos^2\beta_1}{\sigma}\left\{\tan\beta_1-\dfrac{r_2V_{x2}}{r_1V_{x1}}\tan\beta_2-\dfrac{\omega r_1}{V_{x1}}\left(1-\dfrac{r_2^2}{r_1^2}\right)\right\}\end{array}\right] \tag{27}$$

A widely applicable correlation was thus developed to relate the total pressure loss across a compressor blade element to the velocity triangles and cascade geometry. The relation between total pressure loss and wake momentum thickness and form factor,

Equation 20, is an analytical relation based on first principles for two-dimensional, incompressible flow. The relationship between velocity triangles, cascade geometry, and wake momentum thickness, as epitomized in Figure 10, is semiempirical, with low-speed cascade data used to develop the correlations.

It was known (Lieblein, 1956) that the total-pressure loss across a cascade was weakly influenced by inlet Mach number as long as the Mach number was kept below some critical value. If the Mach number was increased further, there was a considerable increase in loss, as shown in Figure 11. The flow physics which caused this rapid increase in loss was poorly understood, but it was generally believed to be the result of supersonic flow in the blade passage being terminated by shocks, with possible boundary layer separation. The increased losses were avoided by restricting the inlet relative Mach number to $M \leq 0.8$, but this limited the stage pressure ratio to approximately 1.2:1.

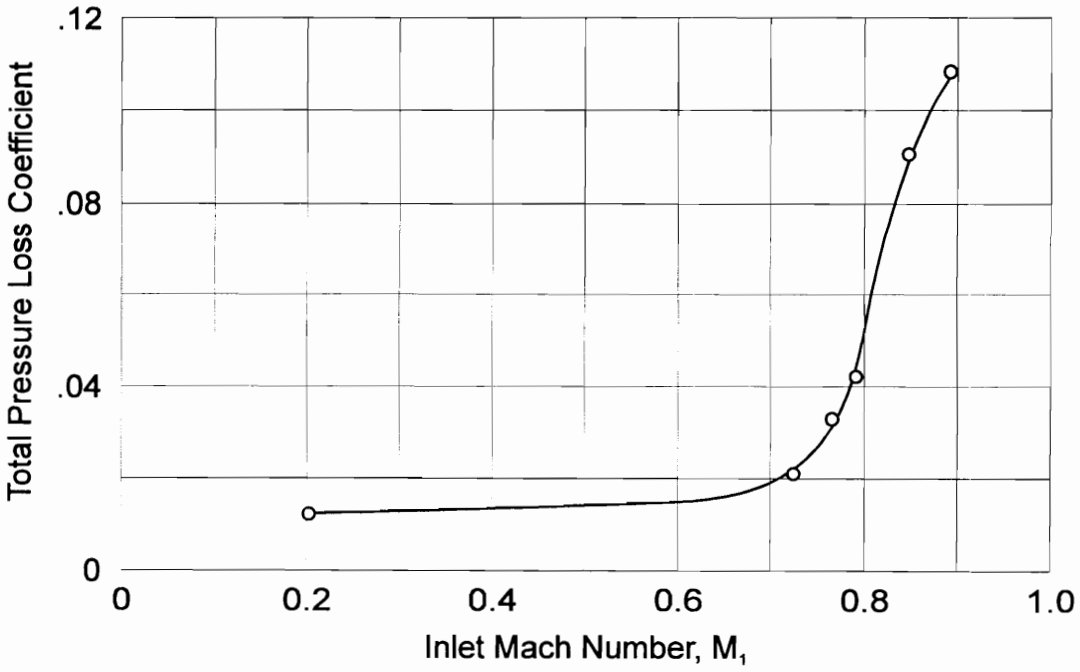

Figure 11. Variation of cascade loss with inlet mach number for NACA 65-($12a_{10}$)10 blade in region of minimum loss (Lieblein, 1956)

It was also recognized (Klapproth, 1954) that by eliminating IGVs and using transonic relative Mach numbers, it was possible to input significantly more work at the rotor tip than if IGVs were used (for the same limiting value of diffusion). If the losses could be controlled such that the work input increased in proportion to the increased blade losses, higher rotor pressure ratios could be obtained without loss of efficiency. The performance requirements of aircraft turbine engines has motivated the use of higher relative Mach numbers to achieve this goal.

While the combination of Equations 27 and 20, along with the data correlation of Figure 10, provided a simple means to predict the performance of a low-speed cascade, the effects of compressibility were ignored. In spite of this, the Lieblein loss models have been used to design compressors which operate in the transonic and supersonic regimes.

Swan (1961) started with Equation 27 to calculate the equivalent diffusion ratio, D_{eq}, and used curve fits to evaluate the wake momentum thickness ratio, θ/c, as a function of D_{eq}. For operation at minimum-loss incidence, a family of curves was used to correct θ/c for radial position along rotors only. For off-design operation, momentum thickness was corrected for rotor inlet Mach number, but not spanwise location. The simplified form of the loss relation, Equation 21, was used to calculated the rotor profile loss. It is unclear how the stator losses were determined.

Noting that Lieblein (1957, 1959) had taken the approach of looking at on-design flow separately from off-design, Swan corrected θ vs. D^*_{eq} for spanwise position along the rotor in a manner similar to a trend Lieblein supposedly observed in $\overline{\omega}$ vs. D. Because Lieblein's diffusion factor was developed for design-point operation, Swan did not make a similar off-design correction. These comments suggest that Swan made a common mistake of assuming that Lieblein's diffusion factor (also called the D-factor), D, and his equivalent diffusion ratio, D^*_{eq}, are interchangeable. While both D and D^*_{eq} were attempts

to correlate profile loss and maximum allowable blade loading at minimum-loss incidence with cascade diffusion, the definitions show them to be fundamentally different (see Equations 6 and 24, pages 16 and 26, respectively).

The diffusion factor, D, was derived from first principles by assuming that the ratio of momentum thickness to chord does not vary much for "conventional types of blading," e.g. NACA 65-A_{10} profiles, and ignoring certain constants accordingly. This method is applicable to design-point operation only. The equivalent diffusion ratio, D_{eq}, on the other hand, was empirically correlated (not derived from first principles) and is applicable for both design-point and off-design operation. The limiting value of diffusion factor, beyond which losses increase dramatically, is $D \leq 0.6$ while the limiting value of equivalent diffusion ratio is $D_{eq}^{*} \leq 2.0$.

While Swan reported that the design-point momentum thickness correction was similar to that reported by Lieblein (1956), Lieblein did not suggest a correction for either $\overline{\omega}$ vs. D or θ vs. D_{eq}^{*} as a function of spanwise location. Lieblein simply noted that in the tip region of rotors, where the tip-clearance and endwall effects could not be separated, the total pressure loss coefficient increased almost linearly with D. Because this increase was not present at mean radius, and no data were available between mean- and tip-radius for comparison, Lieblein suggested a correction ***only*** for the 90% span location of rotors.

Swan asserted that spanwise location of the element had little effect on off-design momentum thickness, and corrected for relative Mach number instead. It is conceivable that the design-point momentum thickness correction for spanwise location should have been attributed to relative Mach number, but no data comparisons were offered to support either correction (only the curves used were included). Because the data comparisons in this paper were so sparse, it is difficult to assess the general validity of the model.

Jansen and Moffatt (1967) used Equation 6 to calculate the design diffusion ratio and used a curve supposedly fitted to the loss relation of Figure 8b to calculate $\overline{\omega}^*$. If the design-point relative Mach number was greater than 0.7, the design-point loss coefficient and inlet air angle were corrected according to the relations

$$\overline{\omega}^{*''} = \overline{\omega}^*\left[2\left(M_1 - M_{1cr}\right)+1\right] \tag{28}$$

$$\beta_1^{*''} = \beta_1^* + 10M_1 - 7 \tag{29}$$

For off-design operation with $M_1 > 0.7$, a correction was made to the choking inlet air angle in the form

$$\beta_{1ch}'' = \beta_{1ch} + 1.5\left(10M_1 - 7\right) \tag{30}$$

The stalling inlet air angle was not corrected for Mach number. The off-design loss coefficient was calculated as a polynomial such that the loss at stall or choke is twice the minimum loss value according to the relation

$$\overline{\omega} = \overline{\omega}^{*''}\left[0.8333\left(\frac{\beta_1 - \beta_1^*}{\beta_{1,xx} - \beta_1^*}\right)^2 + 0.1667\left(\frac{\beta_1 - \beta_1^*}{\beta_{1,xx} - \beta_1^*}\right)+1.0\right] \tag{31}$$

where *xx* represents either the stalling or choking value.

While Jansen and Moffatt (1967) stated that a curve fit was used to calculate $\overline{\omega}^*$ according to the relation in Figure 8b, a plot of the equation stated in the paper matches the data of Figure 8a instead. The difference in magnitude between these two loss relations is evident from the figure. For this reason, it is uncertain whether a consistent relation between the fitted curve and the design-point loss coefficient was used or whether a significant error was made. Because the off-design loss relation is also based

on the suspicious design-point loss coefficient, the usefulness of this model is questionable.

It was recognized that the loss models of Swan (1961) and of Jansen and Moffatt (1967) were attempts to apply the fundamentally sound low-speed loss models of Lieblein (1953, 1957) far outside of the bounds of the original data sets. These low-speed models were applied to high-speed flows simply because a more fundamentally-based model did not exist, and the results obtained were as accurate as was possible at the time. By adding many years of proprietary corporate experience to the loss relation typified in Figure 8, engine manufacturers have been able to accurately predict the design-point performance of machines which do not stray very far from their respective knowledge base. Extrapolation from an existing database to a radical new design, however, has not typically provided a satisfactory prediction.

In an effort to extend the reasonable range of profile loss model applicability to the transonic regime, Koch and Smith (1976) rewrote Lieblein's equivalent diffusion ratio as the product of 3 other velocity ratios

$$D^*_{eq} = \frac{V_{\max}}{V_{fs,2}} = \frac{V_{\max}}{V_{th}} \times \frac{V_{th}}{V_1} \times \frac{V_1}{V_{fs,2}} \tag{32}$$

where V_{th} is the velocity in the cascade passage throat, which was assumed to occur at one-third of the axial length of the cascade.

By considering only well-designed blade shapes operating at minimum-loss incidence, Koch and Smith developed a semiempirical correlation for D_{eq}^{*} which accounts for blade thickness, with approximate corrections for compressibility and streamtube contraction

$$D_{eq}^{*}=\frac{V_1}{V_2}\sqrt{\left(\sin\beta_1-K_1\sigma\Gamma^{*}\right)^2+\left(\frac{\cos\beta_1}{A_{th}^{*}\left(\rho_{th}/\rho_1\right)}\right)^2}\left(1+K_3\frac{t_{\max}}{c}+K_4\Gamma^{*}\right) \tag{33}$$

where

$$\Gamma^{*}=\frac{\Gamma}{cV_1}=\frac{\Delta\left(rV_\theta\right)}{2\sigma_m r_m V_1}$$

$$A_{th}^{*}=\left[1-\frac{K_2\sigma\frac{t_{\max}}{c}}{\cos\overline{\beta}}\right]\left(1-\frac{A_{a1}-A_{a2}}{3A_{a1}}\right)$$

$$\overline{\beta}=\left(\frac{\beta_1+\beta_2}{2}\right)$$

$$\frac{\rho_{th}}{\rho_1}=1-\frac{M_x^2}{1-M_x^2}\left(1-A_{th}^{*}-K_1\frac{\tan\beta_1}{\cos\beta_1}\sigma\Gamma^{*}\right)$$

The constants K_1 through K_4 are contained in the first two velocity ratios in Equation 32 and were calibrated to reduce the deviation between the predicted values of $V_{\max}$ and the values predicted by a potential flow analysis of 34 cascades covering a wide range of solidity, camber, and stagger.

A blade-to-blade boundary layer code was then used to correlate the trailing edge boundary layer momentum thickness and form factor with equivalent diffusion ratio. By using the trailing edge values, as opposed to wake values, the effects of finite trailing edge thickness and wake mixing were avoided. The computer program calculated the compressible boundary layer over both surfaces of an imaginary blade, and the boundary layer was assumed turbulent everywhere. The inviscid velocity field was specified as a

linear velocity gradient from 1/3 chord to the trailing edge, and the ratio $V_{max}/V_{fs,2}$ was varied from 1.3 up to the value that produced separation. A subtle, but important, point in this paper is that the boundary layer program was used only to develop the correlations, not in the application of the model after the initial correlations were made.

The correlations determined from the boundary layer code were presented in two categories. First, the trailing edge momentum thickness and form factor were correlated with equivalent diffusion ratio for incompressible, constant streamtube height flow with a Reynolds number of 10^6. This momentum thickness correlation was similar to that of Lieblein (1957), with the differences attributed to the fact that Lieblein's cascade data were at a different Reynolds number and that Lieblein's momentum thickness was measured in the wake instead of at the trailing edge. Second, additional curves were used to correct the momentum thickness for Mach number, streamtube height ratio, Reynolds number, and surface roughness, and to correct the form factor for Mach number and streamtube height ratio.

Data comparison indicated that an addition of 0.0025 to the low-speed momentum thickness correlation was needed. The reasons for this addition were not understood at the time of the paper, but it was necessary to match the data. A compressible-flow mixing calculation similar to that of Stewart (1955) was then used to calculate the fully-mixed loss coefficient. The model of Koch and Smith (1976) is generally accepted as the most fundamentally-based profile loss model in the open literature, as it accounts for many of the real-fluid phenomena which exist in a transonic compressor in a rational manner (Hirsch and Denton, 1981; Çetin, et al. 1987), but application of the model is restricted to minimum-loss operation of well-designed airfoils.

In an attempt to improve the range of applicability of loss correlations used in compressor throughflow calculations, Çetin, et al. (1987) reviewed 8 transonic compres-

sor tests and proposed a new off-design total loss correlation. All of the machines reviewed had either Double-Circular-Arc (DCA) or Multiple-Circular-Arc (MCA) blading, and all of the rotors had part-span dampers. Losses were considered as a whole and were expressed by a total-pressure loss coefficient which accounted for all types of losses except for the blockage effects of the end-wall boundary layer and tip-clearance effects. Shock losses and part-span damper losses were apparently included in this overall loss coefficient.

Inlet Mach number and type of blading (DCA vs. MCA) were concluded to be the 2 strongest governing factors in determining off-design loss at transonic speeds, but Mach number and 3-D effects could not be separated in this analysis. A parabola was used to correlate off-design losses according to

$$\overline{\omega} = \overline{\omega}^* + c_m \left(i - i^*\right)^2 \tag{34}$$

where c_m is a function of inlet relative Mach number, blade profile shape, and whether the blade is operating at greater or less than design incidence. The steeper slope on the choking side of the loss bucket generated by this correlation is apparent in Figure 12, and this was felt to be a better representation of the data than a symmetric parabola.

The design-point loss coefficient in Equation 34, $\overline{\omega}^*$, was supposedly determined using the loss model of Koch and Smith (1976), but significant errors appear to have been made in its application. The subroutine used by Çetin, et al. (1987) to evaluate the new loss and deviation correlations was included in an Appendix, and that source code has been independently scrutinized by the present author and by Hale (1996). These reviews revealed that, once the trailing edge momentum thickness and form factor had been estimated, the loss coefficient was calculated from Equation 20 instead of with a compressible mixing calculation. Neglecting the mixing loss can result in an error of the

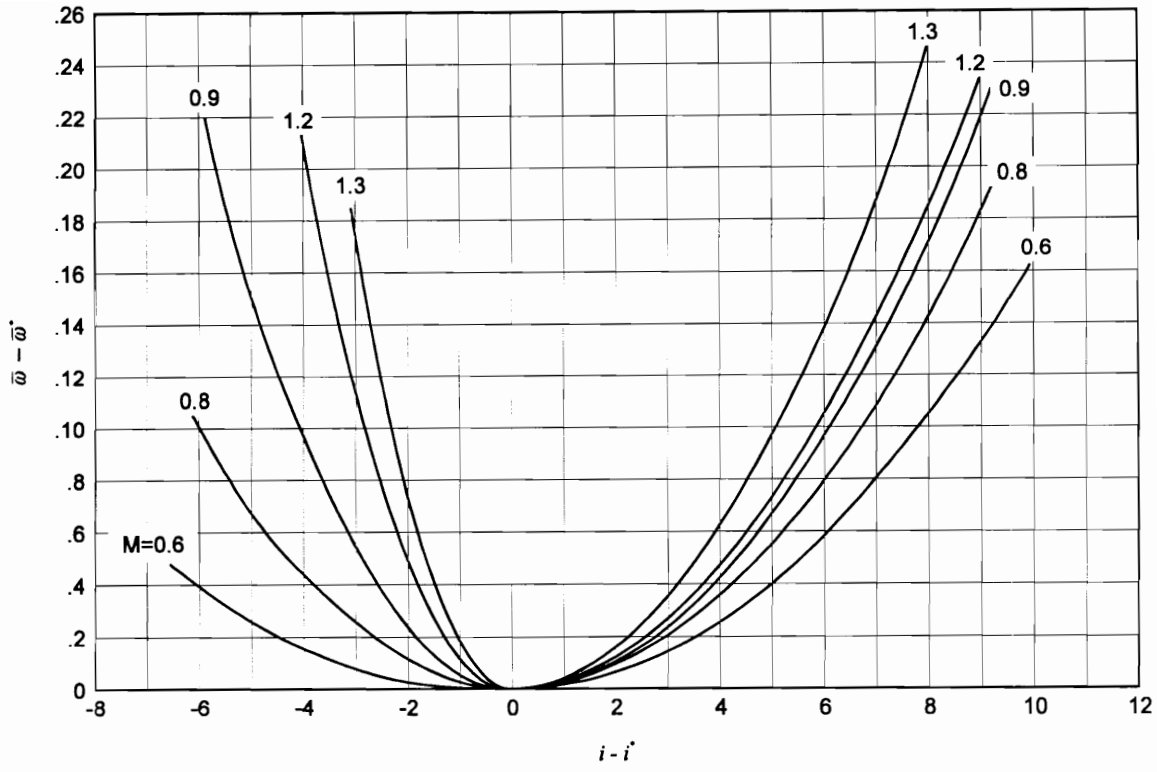

Figure 12. Typical off-design transonic loss buckets for DCA blades (Çetin, et al., 1987)

order of 30% for the fully-mixed loss coefficient (Lieblein, 1956b). In addition, the shock loss attributed to leading edge bluntness was included, but the passage shock loss model used by Koch and Smith (1976) was omitted.

Because the equations governing entropy generation are highly nonlinear, Çetin, et al. (1987) asserted that predicting the total loss from superposition of the losses due to shocks, profile boundary layers, tip-clearance, etc. was "not likely to be realistic." But the loss generated by a part-span damper is likely to be concentrated near the damper itself, and the loss generated by a shock is limited to the regions of supersonic flow. Instead of attempting to model the physics of any of the loss processes or interactions, least-squares curve fits were used to correlate the data with inlet Mach number and incidence angle.

While this approach may have merit for identifying some global trends, it obscures the nature of the specific mechanisms and their interactions, and it smears their effects evenly from hub to tip. Application of these correlations outside of the original data set should be discouraged, as no fundamental basis suggests they would be applicable. In fact, data comparison in the report showed the new correlations to be accurate within $\pm 30\%$ of the total loss for only about 60% of the data that was not used to develop the correlations. Because the correlations are not generally applicable and offer no suggestions for further research, they have somewhat limited value.

2.2 Summary of Profile Loss Models

There are 2 well-known design-point profile loss models, and 2 types of off-design models in the open literature. The most commonly used design-point model is Lieblein's (1956) loss as a function of diffusion factor, D, as shown in Figure 8a. For low-speed, two-dimensional cascades, the ordinate in Figure 8a is approximately equal to the wake momentum thickness, but this simplification cannot be made for compressible flow. In either case, the correlation implied by this figure is strictly empirical, with no closed-form analytical relation to predict it. The diffusion factor can be calculated from either Equation 6 or 8, and the loss coefficient can be easily measured. The ease of updating the empirical database typified by Figure 8a makes this method favored by engine companies because they have an ever-expanding collection of test data.

The other common type of design-point loss model uses empirical correlations of momentum thickness and form factor with equivalent diffusion ratio, Equation 24, and an analytical relation between momentum thickness and loss coefficient. If the trailing edge boundary layer thicknesses are correlated, a mixing calculation similar to that of Stewart (1955) is used; if the wake thicknesses are correlated, the loss is calculated from

Equation 20. Because the profile boundary layer thicknesses are not easily measured on an actual compressor blade, it is more difficult to update the empirical databases required by this model. If one does not have access to a large number of test results from modern blade shapes, however, use of the correlations of Koch and Smith (1976) will likely predict the design-point loss more accurately than use of the diffusion factor (Çetin, et al., 1987).

The method described in the previous paragraph can also be used to predict off-design profile losses if suitable off-design boundary layer correlations are known. While this method is the most fundamentally sound off-design profile loss model in the open literature, it is not commonly used. Instead, the off-design loss bucket is typically assumed to be a parabola of the form

$$\overline{\omega} = a\left(i - i^*\right)^2 + b\left(i - i^*\right) + c \tag{35}$$

where a, b, and c are constants. This type of loss bucket is typically specified such that the stalling and choking losses are twice the minimum loss value. Since an infinite number of parabolas can be drawn through any 2 points, these loss buckets can best be described as arbitrary.

It is apparent from the above discussion that critical portions of the current state-of-the-art profile loss models are grounded in empiricism, instead of theory. A significant contribution would be made by determining an analytical relation between some diffusion parameter (D, D_{eq}, or a newly defined parameter) and the trailing edge momentum thickness for compressible flow. By combining this new relation with an analytical relation between momentum thickness and total pressure loss coefficient, a fundamentally based profile loss model could be developed. This model would be valid for both design-point and off-design flow, as long as significant separation is avoided.

2.3 Shock Loss Models

The foundation of the modern shock loss models is that of Miller, et al. (1961). This method assumed that a normal shock extended from the blade leading edge to the suction surface, normal to the mean passage camber line, as shown in Figure 13. Although casing measurements had indicated that the passage shock was somewhat curved and stood slightly ahead of the blade at the design point, the effects of the detachment distance and curvature were determined to be small. A Prandtl-Meyer expansion was calculated from the upstream condition to determine the Mach number at the suction surface shock impingement point. The arithmetic average of this Mach number and the Mach number existing at the upstream condition was then used in the shock calculation.

Because the shock geometry was not known to vary with throttle setting, the only inclusion of off-design effects was the change in upstream incidence angle. As the incidence angle increases, a larger Prandtl-Meyer expansion occurs and the Mach number

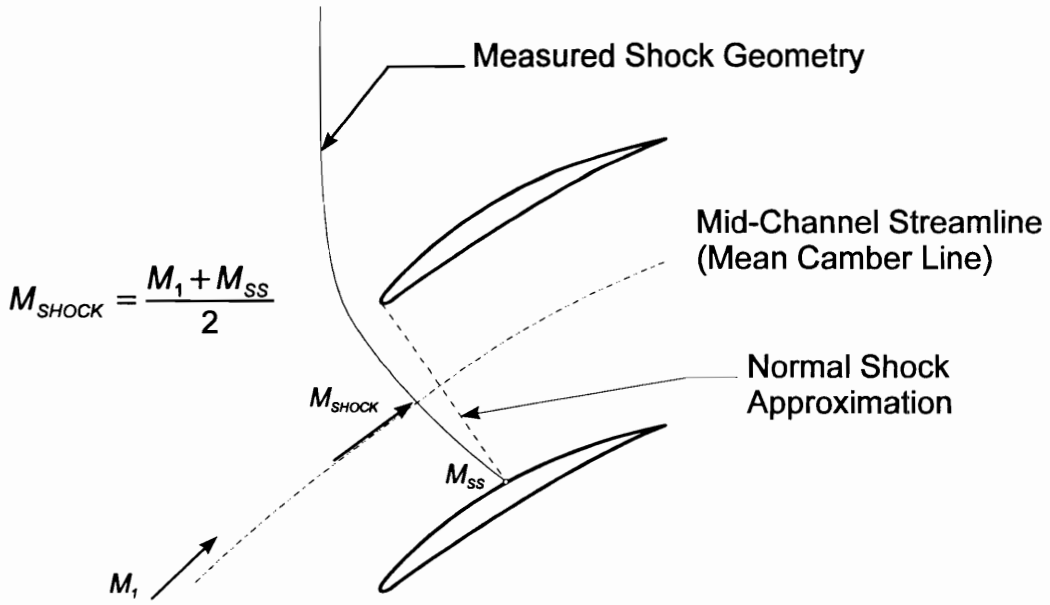

Figure 13. Shock geometry used for Miller, Lewis, and Hartmann (1961) shock loss model

ahead of the shock increases. Because the incidence variation between peak efficiency and stall was not large, only small changes in shock strength were predicted. The authors concluded that this model should be restricted to design-point calculations, as it seriously underestimated the increase in shock loss as incidence is increased above the design-point value.

Boxer (1969) developed a shock model to be applied to high-reaction supersonic blade sections with sharp leading edges, straight entrance regions, and large camber values (12° to 56°) concentrated near the trailing edge of the blade. A normal shock was assumed to extend across the passage as close to the leading edge as stability would allow. For Mach numbers greater than 1.3, the suction surface boundary layer was assumed to separate and not reattach. A dump diffusion process was assumed to occur slightly downstream of the trailing edge where the separated boundary layer mixed with the free-stream flow.

This model is only applicable at the maximum pressure ratio, maximum efficiency operating point and requires an *a priori* knowledge of the sidewall separation effects on the exit flow. While this model might be a reasonable approximation for the operation of the highly-cambered supersonic blade sections considered, machines designed based on this philosophy performed poorly (Wennerstrom and Stavros, 1966; Carman, et al., 1968) and this approach to compressor design was abandoned. This model is clearly not applicable to what are known today as well-designed transonic airfoils.

Balzer (1970) asserted that, although there may be more than 1 shock within a cascade passage, the loss associated with a single normal shock is representative of the loss in the actual shock system even for off-design operation. Since the fluid properties along the mean flow path are some average of the properties normal to the path, it was suggested that the "average" properties are encountering a normal shock. By using

experimentally determined flow angles along the mean flow path, the method of Miller, et al. was applied to an off-design analysis with favorable results. This approach suggested that even a crude model can predict shock losses quite accurately over a wide range of operation if the representative conditions upstream of the shock are known. Unfortunately, the method did not address how to obtain the "representative" conditions upstream of the shock without measuring them.

Koch and Smith (1976) reported that the shock loss for "well-designed" transonic airfoils operating at minimum-loss incidence is determined by the diffusion which occurs across the passage shock and by the blade leading edge bluntness. The passage shock model was assumed to generate the entropy rise across 1 oblique shock that reduces a "representative" passage inlet Mach number to unity. If the blade exit Mach number is supersonic, the oblique shock reduces the "representative" passage inlet Mach number to the exit Mach number. The "representative" passage inlet Mach number was presented as a weighted average of the suction surface Mach number and the upstream Mach number. The loss associated with leading edge bluntness was added in the form

$$\frac{\Delta s}{R} = -\ln\left\{1 - \frac{t_{LE}}{s\cos\beta_1}\left[1.28\left(M_1 - 1\right) + 0.96\left(M_1 - 1\right)^2\right]\right\} \tag{36}$$

which gives

$$\overline{\omega}_{shock} = \frac{\frac{t_{LE}}{s\cos\beta_1}\left[1.28\left(M_1 - 1\right) + 0.96\left(M_1 - 1\right)^2\right]}{1 - \frac{P_1}{P_{01}}} \tag{37}$$

Although the above approach did not address shock geometry directly, it did include an attempt to address the effect of leading edge thickness on shock loss. No

bluntness data were presented to support this correlation, however, so assessment of its accuracy is not possible.

Prince (1980) reviewed a large number of supersonic cascade and rotor tests in an attempt to understand the differences between the anticipated and measured shock structures. The measured shock discontinuities were substantially below expectations because the shock was significantly more oblique than expected, and it was determined that the blade leading edge makes an oblique angle with all stream surfaces. This is shown in Figure 14 for the case of a passage shock which is normal to the suction surface of a transonic rotor. Because stagger angle increases with increasing radius, a normal shock in the passage will intersect the suction surface farther downstream at the tip than at mid-span. This results in a spanwise sweep of the shock as it intersects the suction surface.

Wennerstrom and Puterbaugh (1984) extended the method of Miller, et al. (1961) to reflect the above-mentioned three-dimensional shock geometry. First, the locus of points where the shock impinges on the suction surface is calculated for all streamlines. This line is typically swept back relative to the flow as one proceeds from hub to tip, and the suction surface obliqueness angle is determined from the slope of this line. Then the Mach number on the suction surface is calculated as a Prandtl-Meyer expansion from the upstream conditions to the suction surface blade angle. On the pressure surface, the shock is assumed to be attached to the leading edge of the blade and the spanwise sweep angle here is assumed to be the leading edge sweep angle; the Mach number is assumed to be the upstream Mach number. The Mach number and sweep angle are assumed to vary linearly from pressure to suction surface and a 3-point integration of shock loss is performed across the passage. As with the model of Miller, et al., application of this model is limited to design-point operation.

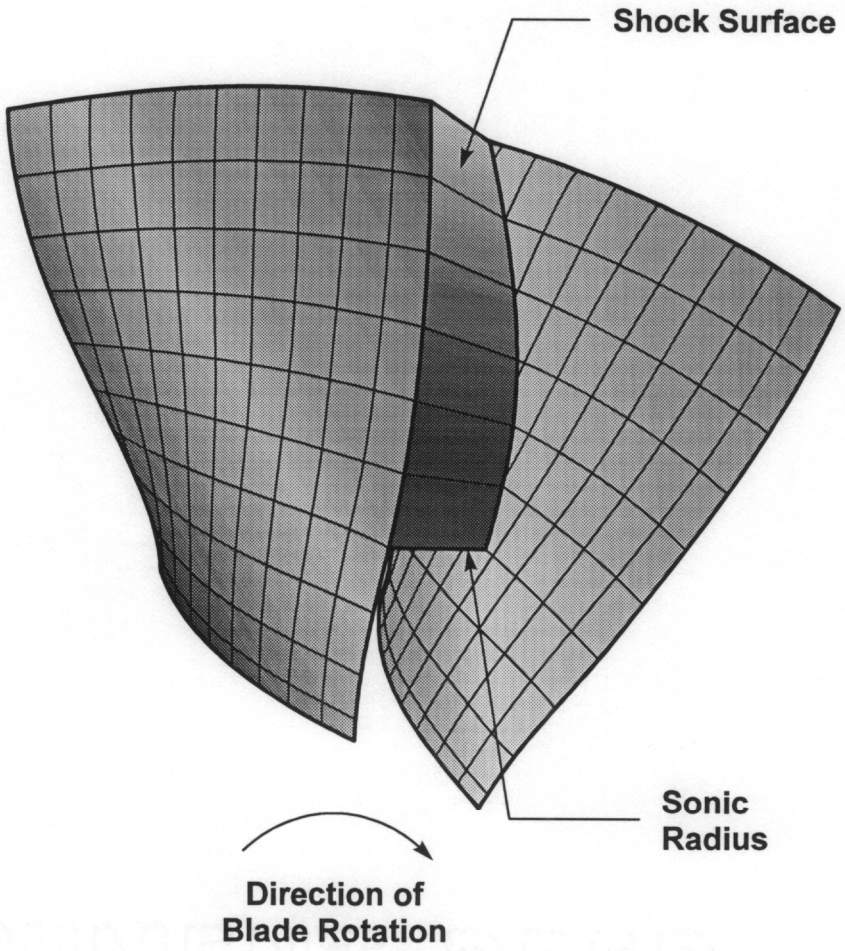

Figure 14. Transonic rotor passage showing spanwise sweep of passage normal shock

This three-dimensional model predicts a lower shock loss than the model of Miller, et al., and the corresponding higher pressure ratio and higher efficiency predictions matched the presented transonic rotor data more closely than the older method. It was also concluded that spanwise blade sweep could be used as a compressor design variable to either maintain efficiency at higher tip speeds or increase efficiency at conventional tip speeds.

Broichhausen and Gallus (1982, 1987) studied an extremely low aspect ratio (near 0.31) supersonic compressor which was tested both in a rotor-only configuration and with

a tandem stator downstream. The shock loss was calculated as being comprised of a detached bow shock and a normal passage shock, although the contribution from the bow shock for a rotor with a straight entrance region was determined to be negligible in comparison with the magnitudes of the other loss sources. The bow shock was approximated as a hyperbola which is normal to the free stream at the foremost point and asymptotically approaches the free stream Mach lines, after Moeckel (1949). The Mach number upstream of the passage shock was assumed to be the arithmetic mean of the upstream Mach number and the Mach number obtained from a Prandtl-Meyer expansion to the suction surface shock impingement point, after Miller, et al. (1961) and as shown in Figure 13.

Broichhausen and Gallus (1987) made comparisons between measurements and predictions, but the predicted losses were presented as the summation of profile, bow shock, passage shock, and shock-induced separation losses. Separate, not-validated loss models were presented for each mechanism. Only 11 data points, obtained from 2 different rotors, were presented for comparison and no thorough parametric investigation was conducted. Given the uncertainty associated with each of these predictions, it is quite conceivable that low estimates obtained from one model may have been canceled by high estimates from another, and the overall agreement may have been fortuitous. In the present author's opinion, insufficient data were presented to evaluate the 4 models used in the performance predictions.

Schreiber (1987) analyzed the wake measurements of 3 transonic and supersonic cascades in which the inlet Mach number was varied from supercritical subsonic up to the "unique incidence" condition to determine the relative contributions of viscous and shock losses on cascade performance. For a supersonic cascade, the flow through the entire passage experiences a passage shock of some sort which generates a total pressure loss.

In addition, the flow near the blade experiences an additional viscous loss from the blade profile boundary layer, as shown qualitatively in Figure 15. The pitchwise traverse measurements were used to determine the edges of the wake, and the losses were separated by assuming a linear variation of shock loss within the wake region. It was determined that the viscous loss was only slightly influenced by Mach number and that the increase in overall loss with increasing Mach number is predominantly caused by the increased shock losses.

Dunker (1987) published an attempt to model the shock loss which will exist when a cascade is operated at supercritical subsonic Mach numbers. The approach used measured shock geometry from a single experiment to correlate the location of the terminating shock, which was assumed to be perpendicular to the suction surface. A simple wave model was used to calculate the subsonic flow upstream of the shock, while a Prandtl-Meyer expansion was used to calculate the supersonic region. An arithmetic

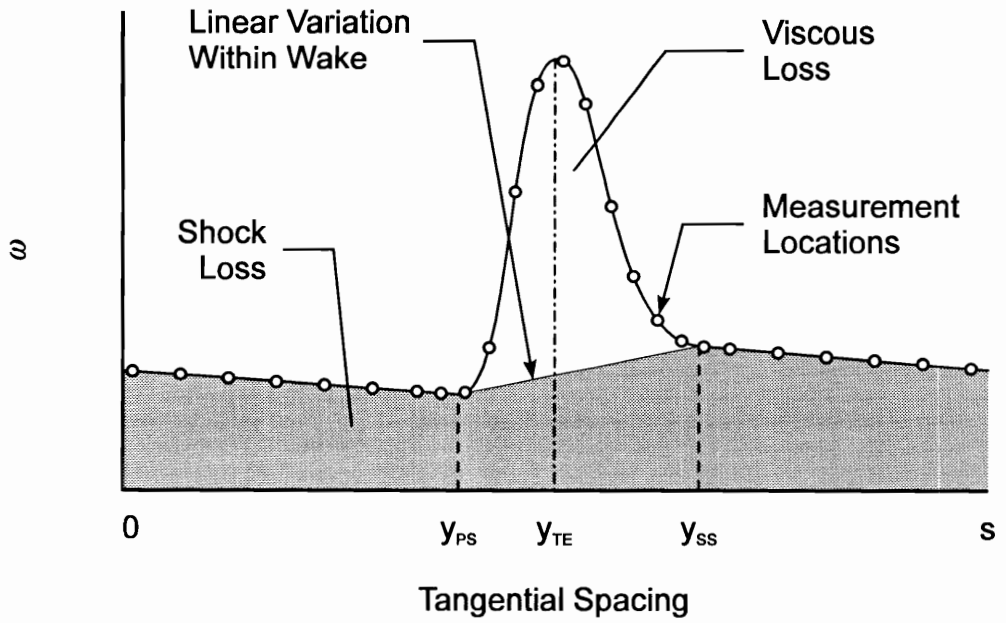

Figure 15. Shock and viscous losses in the measuring plane downstream of supersonic cascade

average of the Mach number at the free-stream edge of the shock and the Mach number where the shock intersects the suction surface were used to calculate the shock loss. Application of this model predicted loss coefficients which were less than half of the measured loss, and no explanation was given for the disparity.

Freeman and Cumpsty (1992) developed a simplified model for the process which occurs when a shock stands ahead of the blade leading edge. This is essentially a duct flow calculation in which mass, momentum, and energy are conserved. The blade entrance region is assumed to be both thin and straight, so that a single angle is used to describe the blade and flow directions. This renders the model incapable of addressing cascades with inverse camber to decelerate the flow ahead of the passage shock. The blade exit relative flow angle is considered an input to the model, so the method has limited value as a predictive tool.

Having identified the major limitations of this model, it should be noted that it does reproduce many of the qualitative trends observed in transonic compressors. These trends include increased loss with increased incidence or increased wheel speed, and the narrowing of the useful operating range between choke and surge as wheel speed is increased. Comparisons made with this model tend to support the view that many trends are determined by overall conservation in the blade-to-blade direction rather than by details of the geometry or 3-D flows, and that even crude models which conserve the basic quantities can provide reasonably accurate predictions (Denton, 1993). In addition, it was asserted that for $U/\sqrt{c_p T_{01}} \geq 0.75$, the loss due to the shock system dominates the losses from other sources.

2.4 Summary of Shock Loss Models

To summarize, the most sophisticated shock loss model in the open literature assumes that the passage shock structure in a transonic rotor operating at peak efficiency is a single normal shock in the cascade plane. This model is incapable of predicting off-design performance. The off-design shock loss models require *a priori* knowledge of flow angle and Mach number significantly downstream of the shock, which limits their usefulness as design tools, and they are limited to the operating region between peak efficiency and surge. None of these models are capable of predicting the performance of multiple passage shocks which will exist during choked operation and, hence, none are applicable in the "unique incidence," or choked region of operation.

2.5 Identification of Potential Loss Model Improvements

The existing subsonic profile loss models provide reasonable predictions for both design-point and off-design operation (Lieblein, et al., 1953; Lieblein, 1957), and the design-point profile loss of transonic blades can be estimated accurately with the model of Koch and Smith (1976). While a fundamentally-based off-design profile loss model for transonic compressors would be a clear and valuable contribution, there are significant technical challenges which must be addressed before this can be accomplished. The profile loss model estimates the entropy production in the blade boundary layer, and this clearly depends on whether the boundary layer is laminar, turbulent, or transitions within the blade passage. Because of the poor fundamental understanding of turbulence and boundary layer transition which exists today (Casey, 1994b; Denton, 1993; Vuillez and Petot, 1994; Jennions, 1994), the next significant improvement in profile loss modeling is not likely within the next several years.

Although an improved profile loss model is not a tractable dissertation topic, it is still possible to make an improvement in transonic loss modeling. Because it is not possible to operate a cascade section at supersonic relative velocities without the existence of passage shocks, an off-design profile loss model will still require a complimentary off-design shock loss model to estimate the overall loss of the blade row. This dissertation will develop an improved understanding of the changes in shock geometry which occur with design-speed operating point. That understanding will then be used to propose a fundamentally-based off-design shock loss model that is applicable over the entire useful supersonic operating range of the cascade.

3. Supersonic Flow in 2-D Compressor Cascades

The goal of this chapter is to provide a review of the physical mechanisms which affect the flow in supersonic compressor cascades. The discussion is intentionally kept as qualitative as possible to identify the general trends and to avoid unnecessarily excessive detail. For the most part, detailed mathematical models for the various mechanisms are deferred until a later chapter.

This discussion begins with the flow conditions leading into a supersonic compressor cascade and the classical assumptions used in its analysis. This will be followed by an explanation of the changes in shock structure which will occur over the complete operating range of the cascade. Much of the supersonic cascade literature (Kantrowitz, 1950; Levine, 1956; Starken, 1971) has focused on the minimum-incidence operating condition, and an excellent treatise on the subject is given by Lichtfuß and Starken (1974). Although this condition is only a portion of the operating range, this is a useful place to begin the current discussion.

3.1 Started Cascade Operation

Consider a cascade section operating with an inlet flow that is supersonic relative to the blade but has an axial component that is subsonic, as shown in Figure 16. There will obviously be a viscous boundary layer near the blade surface, but it is known to be thin upstream of the passage shock. Shock structures are known to be unsteady, but the length scale of the shock motion is small compared to the blade chord. The flow upstream of the passage shock is therefore assumed to be steady and inviscid.

The blade leading edge is assumed to be sufficiently sharp as to allow the shock to be attached. The actual bow waves will be curved and very slightly detached, but this effect can safely be neglected for the present analysis. The bow shock is sufficiently

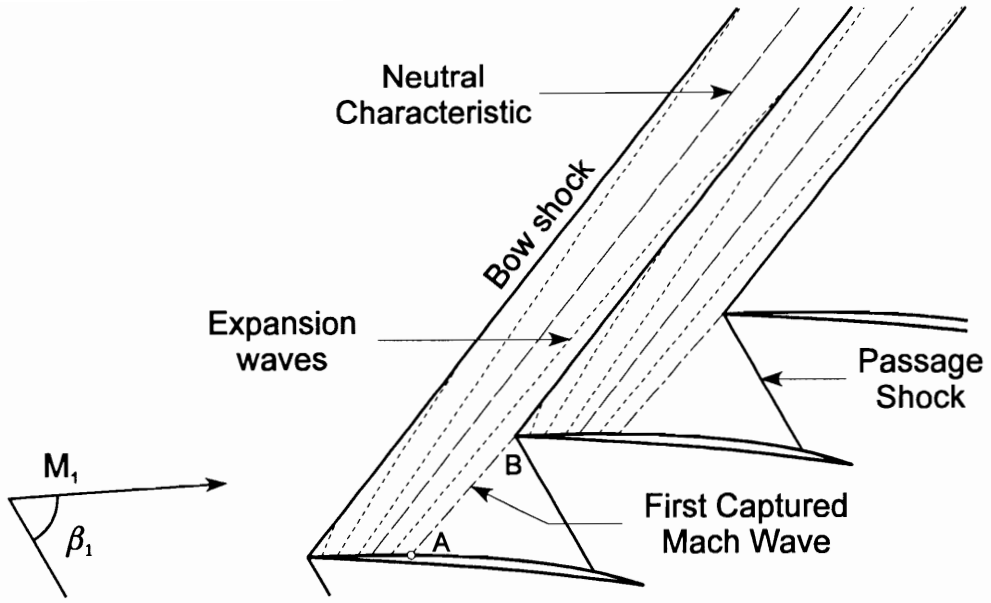

Figure 16. Idealized wave structure in the entrance region of a supersonic compressor cascade

weak everywhere except directly ahead of the leading edge, where it locally becomes a normal shock, that the flow can reasonably be assumed isentropic between the upstream condition and the passage shock. This allows the bow shock to be treated as equivalent to an expansion wave, but of opposite sign.

As the flow passes around the leading edge, it will undergo a Prandtl-Meyer expansion from the upstream flow angle to be aligned with the suction surface blade angle. Since the characteristic lines upstream of the passage shock run only to the left and the flow is assumed isentropic, the flow direction and Mach number are constant along each characteristic. Because the axial component of the flow is subsonic, the Mach waves emanating from the suction surface move upstream of the blade, allowing the cascade to influence the upstream flow.

Near the leading edge, these characteristics intersect the bow shock attached to the leading edge of that blade. There is a particular wave, however, which extends to infinity without intersecting the bow shock attached to the leading edge or the bow shock from

the adjacent blade. This is called the "neutral characteristic," and it is drawn with long dashes in Figure 16. Mach lines downstream of the neutral characteristic will intersect either the bow shock or passage shock emanating from the leading edge of the adjacent blade.

When the flow reaches point *A*, the Mach wave which extends from the suction surface exactly intersects the leading edge of the adjacent blade at point *B*. This is the first captured Mach wave, and it determines the maximum mass flow which can pass through the cascade. The flow region extending upstream from the first captured Mach wave is generally referred to as the "inlet region" or the "entrance region" of the cascade. The location of point *A* depends on suction surface curvature and upstream Mach number, and must be determined by iteratively solving the Prandtl-Meyer and continuity relations. The Prandtl-Meyer relation is given by

$$\beta_1 + \nu(M_1) = \beta_A + \nu(M_A) \tag{38}$$

where ν is the well-known Prandtl-Meyer function.

$$\nu(M) = \sqrt{\left(\frac{\gamma+1}{\gamma-1}\right)}\tan^{-1}\sqrt{\left(\frac{\gamma-1}{\gamma+1}\right)\left(M^2-1\right)} - \tan^{-1}\sqrt{M^2-1} \tag{39}$$

The continuity relation is given by

$$\dot{m} = \frac{F(M_1)P_{01}s\cos\beta_1}{\sqrt{c_pT_{01}}} = \frac{F(M_A)P_{0A}\left|\overline{AB}\right|\sin\mu_A}{\sqrt{c_pT_{0A}}} \tag{40}$$

where F is the following compressible mass flow function.

$$F(M) = \frac{\dot{m}\sqrt{c_pT_0}}{P_0A} = \frac{\gamma}{\sqrt{\gamma-1}}M\left\{1+\frac{\gamma-1}{2}M^2\right\}^{-\frac{\gamma+1}{2(\gamma-1)}} \tag{41}$$

Because we are considering a stationary cascade, the total temperature will be constant between the upstream condition and the first captured Mach wave. The total pressure will also be constant between these locations because the entropy rise across the bow shock has been neglected.

For a given blade shape, β_A and $\left|\overline{AB}\right|$ may be regarded as supplied parameters and the variable M_A must then satisfy both Equations 38 and 40. Clearly, the 2 independent equations for M_A can only be satisfied for particular combinations of β_1 and M_1. For a given value of M_1, a unique value of β_1 can satisfy the equations. Since the upstream flow angle is fixed, so is the mass flow, and the flow is choked. The literature typically refers to this as the "unique incidence" condition, but this term is really a misnomer. This is not the ***only*** incidence at which this cascade can operate for the upstream Mach number, rather it is the ***minimum*** incidence. Operation at higher incidence will be discussed later in this chapter.

The above analysis assumed that the blade leading edge was "sharp," but actual fan and compressor blades have some finite leading edge radius for damage tolerance. The leading edge bluntness causes the bow shock to be slightly detached from the blade, as shown in Figure 17. In the immediate vicinity of point B, where the stagnation streamline intersects the bow shock, the bow shock will be nearly normal to the flow and there will be a small subsonic region behind the shock. The flow quickly expands to supersonic conditions as it proceeds around the leading edge radius, but there will be a small loss in total pressure from the subsonic region. Models for the inclusion of these effects into Equation 40 will be presented in a later chapter.

It is also possible for a cascade to be choked at a throat downstream of the first captured Mach wave at a location where the Mach number is unity, as shown in Figure 18. In this case, the blade is said to have insufficient throat margin and is

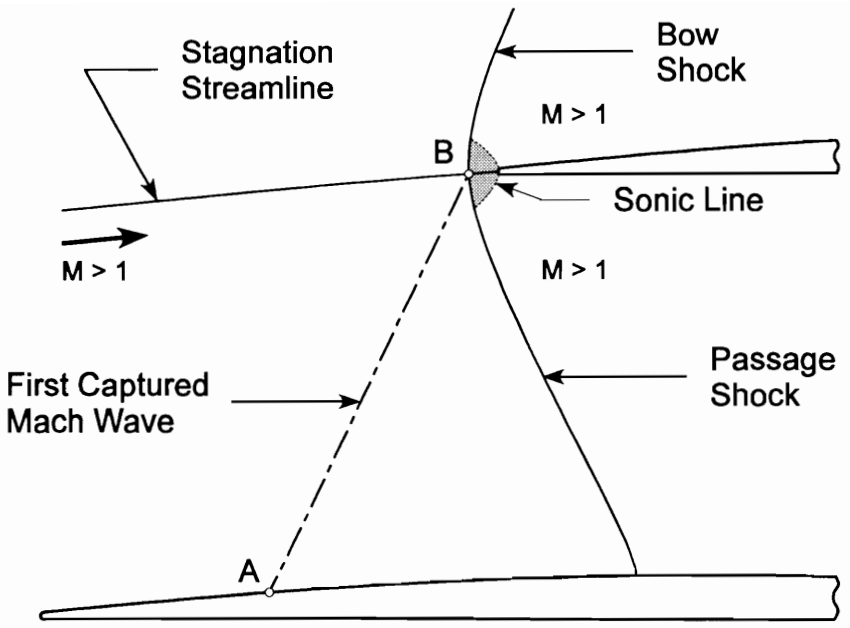

Figure 17. Bow shock detachment upstream of a blade with a blunt leading edge

considered to be poorly designed. Because such blades have little value to the turbine engine community, this mode of operation is not considered in the present analysis.

For low back pressure conditions, the passage shock which begins at the blade leading edge will be a weak shock and the flow downstream of this shock will be supersonic. The amount that the bow shock and passage shock will be swept relative to

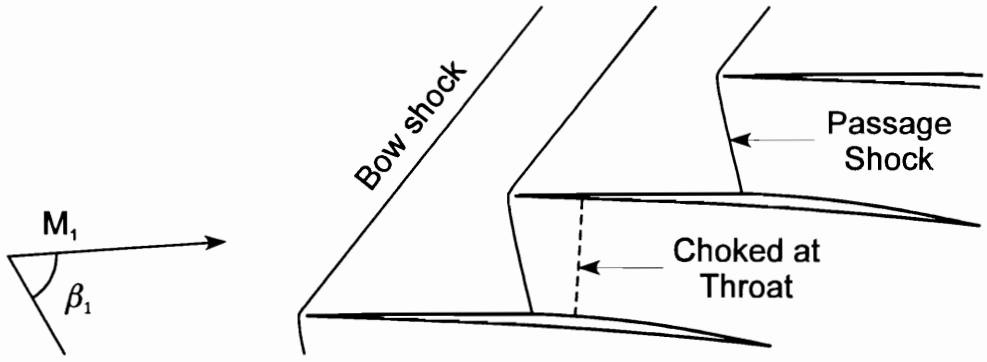

Figure 18. Cascade section choked downstream of the first captured mach wave

the incoming flow will increase with upstream Mach number, as shown in Figure 19. (The black circles in this figure are the mounting pins used to secure the blades to the cascade sidewalls.) The blades shown in this figure are commonly referred to as "precompression blades" because they have negative or inverse camber in the entrance region. Unlike the situation shown in Figure 16, a precompression blade ***increases*** the relative flow angle in the inlet region, decelerating the flow and causing the Mach waves to converge. As long as the blade curvature is modest and gradual, this results in a nearly isentropic deceleration of the flow upstream of the first captured Mach wave.

At the point where the passage shock impinges on the suction surface, continuity requires that the flow be aligned with the blade surface. If the Mach number downstream of the oblique shock is high enough, a reflected shock will exist at an angle such that the flow downstream of the second shock is aligned with the blade surface. A reflected shock is barely visible in the lower part of Figure 19. For the Mach numbers typical of transonic fans, however, the angle required by the second shock is often larger than the maximum deflection possible for the Mach number that exists downstream of the first shock. In this case, the passage shock will become an approximately normal shock very near the suction surface and the flow downstream will be both subsonic and aligned with the blade surface. This situation is called a Mach reflection and is shown in the upper part of Figure 19.

The changes in shock structure which will occur with back pressure can be considered by drawing an analogy between the diverging passage of a compressor cascade and the diverging portion of a Laval nozzle. For the low back pressure conditions shown in Figure 19, supersonic flow will exist downstream of the weak passage shock. (For the case of a Mach reflection, the suction surface boundary layer thickens as a result of the normal shock and this provides the area contraction necessary

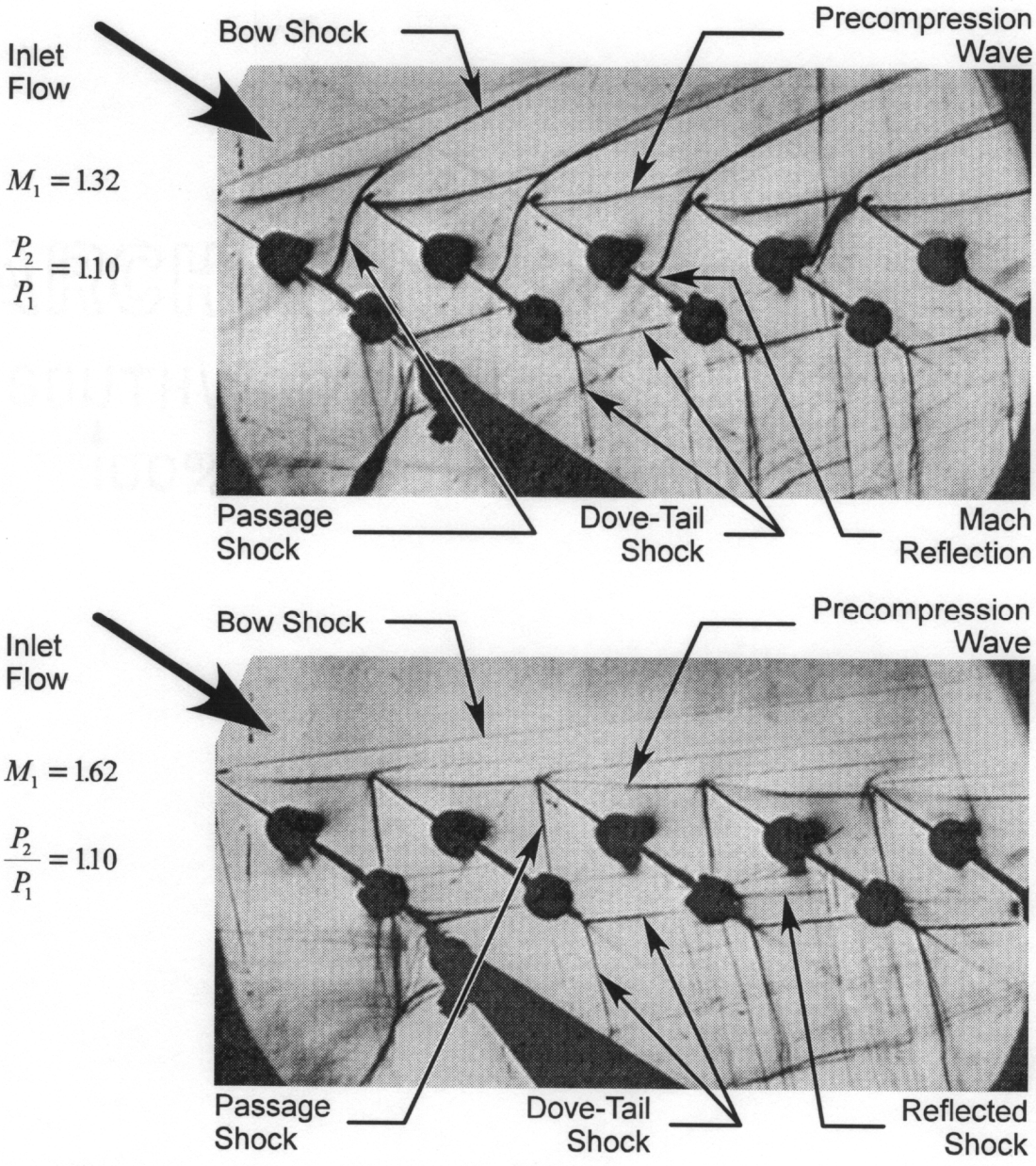

Figure 19. Passage shock structures for low back pressure operation at 2 upstream mach numbers (Tweedt, et al., 1988)

to reaccelerate the flow to supersonic.) An oblique "dove-tail" shock is formed when the supersonic flow reaches the blunt trailing edge. The left-running branch of this shock extends across the entire passage and impinges on the pressure surface of the adjacent blade, while the right-running branch extends indefinitely downstream of the cascade. The cascade exit flow is supersonic for this operating condition.

As the back pressure is increased above some "low" value, the influence of the downstream static pressure begins to move upstream as shown in the upper part of Figure 20. The left-running branch of the "dove-tail" shock still stands at the blade trailing edge, but it merges with a normal shock before reaching the pressure surface of the adjacent blade. This normal shock extends across the entire passage and merges with the right-running branch of the trailing edge "dove-tail" shock. Just as in a Laval nozzle, this normal shock moves upstream with increasing back pressure.

Eventually, however, the back pressure is increased to a point where the normal shock extends across the entire blade passage, as shown in the lower part of Figure 20. This shock is actually very slightly curved so that it is approximately normal to the flow across the entire passage, but this curvature is small and is neglected in the present discussion. The passage shock which originates at the blade leading edge will subsequently be referred to as the "first passage shock" or the "weak passage shock." The normal shock which terminates the region of supersonic flow within the blade passage will be referred to as the "second passage shock." As the back pressure is increased further, the second passage shock continues to move upstream and eventually coalesces with the first passage shock. The range of back pressures for which 2 distinct passage shocks exist will be referred to in this dissertation as the "low back pressure" regime, although there is no standard usage of this term in the literature.

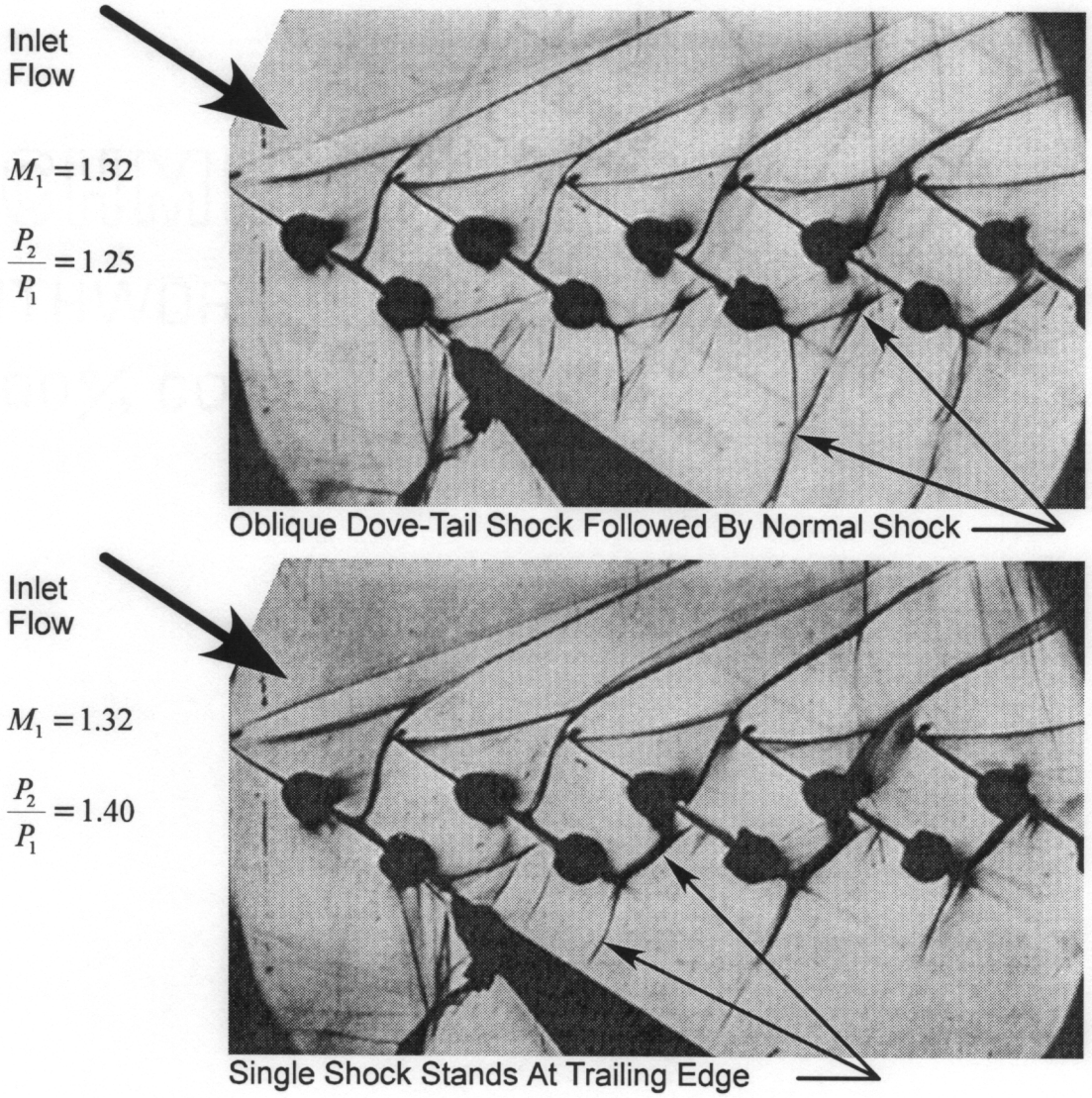

Figure 20. Variation of second passage shock with back pressure in the "low back pressure" Regime

Before continuing this discussion of shock structure variation, a brief digression must be made into one of the difficulties associated with supersonic cascade testing. The sidewall boundary layers thicken as the static pressure ratio of the cascade is increased, allowing the downstream pressure information to move upstream. Because the pressure information moves upstream in the streamwise direction, the rear-most blade passages are affected first. Above a certain back pressure, however, the blade-passage and entrance-

region flow are also affected and it becomes impossible to maintain acceptable flow periodicity without the use of some type of suction device to control the sidewall boundary layers.

While the use of sidewall suction allows a cascade to be operated at higher static pressure ratios while maintaining acceptable flow quality, it makes it much more difficult to obtain high-quality photographs of the shock structure. To be of the greatest value, the holes or slots through which the sidewall boundary layers are removed must be located in the blade passage, thus obscuring the view of the shock system. In addition, the light used to generate the Schlieren images must pass through 4 plexiglass windows, instead of 2. Because each of these panes is of the order of 25mm (1in) thick (Schreiber and Tweedt, 1987), even the first copy of these photographs is not suitable for publication. For this reason, the shock structures shown for the remainder of this chapter are simple sketches which capture the qualitative nature of the flow.

Returning to the discussion of shock structure variation with back pressure, we will now consider the flow regime referred to in this dissertation as the "medium back pressure" regime. As before, this term is presented to help organize the material and there is no standard usage of this term in the literature. This flow regime begins when the second passage shock shown in the bottom part of Figure 20 has moved upstream far enough to just coalesce with the first passage shock. As the back pressure is increased further, the normal shock continues to move upstream. The passage shock structure then becomes a combination of a weak shock that originates at the blade leading edge and a full-passage normal shock, as shown in Figure 21. Because there is supersonic flow downstream of the weak passage shock, there is no change in the flow upstream of the normal shock until the normal shock reaches the blade leading edge.

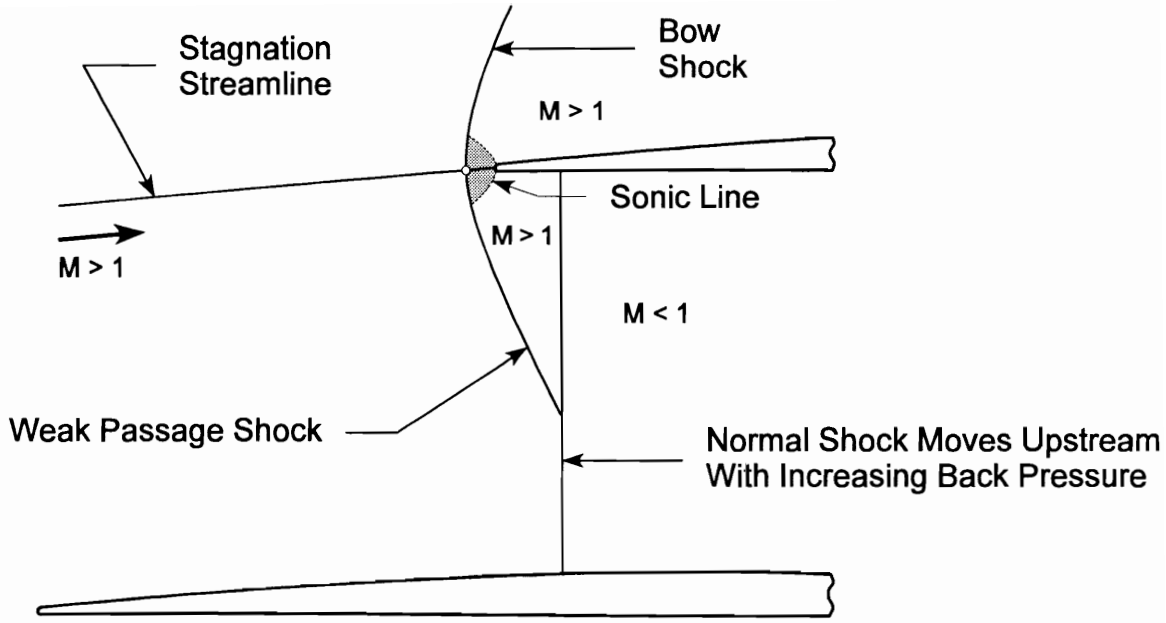

Figure 21. Bifurcated shock structure which exists in the "medium back pressure" regime

For all of the shock structures shown in Figures 19 through 21, the cascade operates at the minimum incidence condition and this is commonly referred to in the literature as a "started" cascade. There is, of course, a maximum back pressure for which a cascade will remain started and this represents the high-pressure end of the "medium back pressure" regime. This limiting pressure is sometimes referred to as P_{2opt} (Starken, 1971; Dunker, 1987) because the minimum ***overall*** loss for the cascade occurs at or very slightly above this value. For this operating point, the passage shock is a single, very slightly curved strong shock which can be closely approximated as a normal shock. This shock, along with the stagnation streamline and first captured Mach wave for started operation, are shown as dashed lines Figure 22.

3.2 Unstarted Cascade Operation

If the back pressure is increased above the value P_{2opt}, the normal passage shock will detach and move upstream of the blade leading edge by an amount Δx. As the

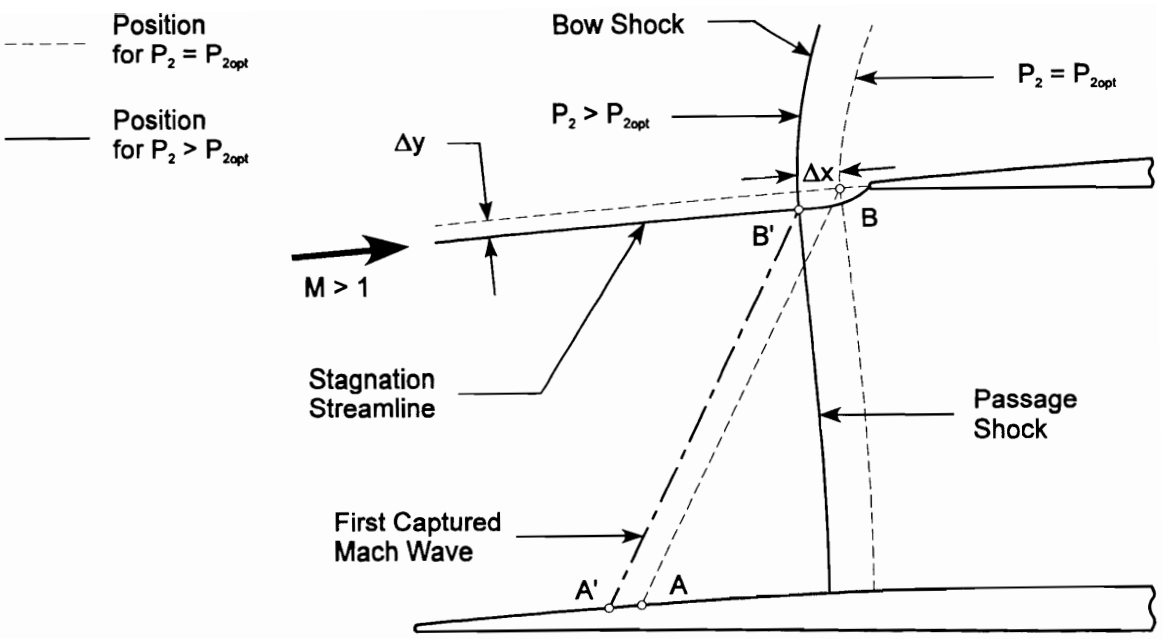

Figure 22. Shock detachment and stagnation streamline shift for an unstarted cascade

passage shock moves upstream, the stagnation streamline will shift toward the suction surface by an amount Δy to provide the typical path for subsonic flow approaching an airfoil. These 2 effects cause the first captured Mach wave to move upstream and to become shorter, as shown by the dark solid lines in Figure 22. Because Equations 38 and 40 must always be satisfied, Δx and Δy are the primary mechanisms which allow the upstream flow angle to increase above the minimum value. Operation with a detached passage shock is commonly referred to as an "unstarted" cascade and will also be referred to in this dissertation as the "high back pressure" regime.

The relationship between the shock detachment distance, Δx, and the stagnation streamline shift, Δy, is currently unknown, but it is possible to calculate the upstream flow angle that would result from assumed values of these parameters. The stagnation streamline shift turns out to be the dominant physical mechanism that increases the upstream incidence angle above the minimum value. Although the present discussion

concerns unstarted performance, this effect can be understood by considering the minimum (started) inlet flow angle for a given Mach number. If the blade thickness is increased, the line segment $\overline{AB}$ in Equation 40 becomes shorter, and this produces the well-known trend of minimum inlet flow angle increasing with blade thickness. Returning now to the unstarted case, an increase in Δy causes a decrease in $|\overline{AB}|$ and an increase in the calculated upstream flow angle.

The shock detachment distance alone, Δx, does not change $|\overline{AB}|$ significantly because the started stagnation streamline immediately upstream of point *B* follows the contour of the blade suction surface immediately upstream of point *A*. By shifting the first captured Mach wave upstream, however, there will be a minor difference between the relative flow angle (and Mach number) at point *A'* and at point *A*. Because there is modest curvature in the entrance region of well-designed transonic compressor blades, however, this has only a second-order effect on the upstream flow angle.

3.3 Summary

To help put the foregoing discussion of shock structure variation in perspective, an overall loss curve for the entire operating range of a typical supersonic compressor cascade is shown in Figure 23. The ability to accurately predict the minimum inlet flow angle, $\beta_{1\min}$, is critical since this has a first-order affect on the choke-limited mass flow estimate for the cascade. The mass flow, in turn, has a first-order effect on the engine thrust calculation.

While it is clearly desirable to operate at the minimum-loss condition, the need to maintain some choke margin for overspeed operation generally requires that the upstream flow angle be greater than $\beta_{1\min}$. Furthermore, all of the unchoked flow conditions which comprise the most useful operating range of a rotor are unstarted conditions. This

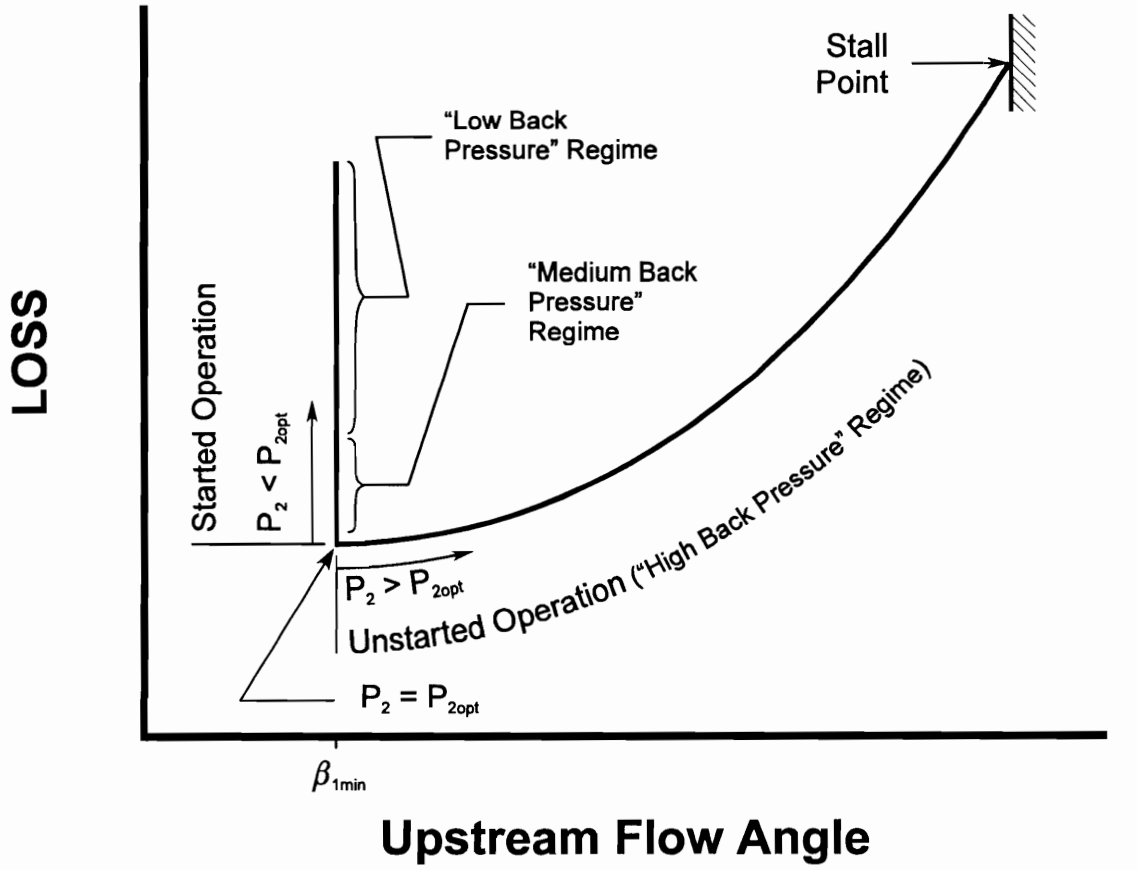

Figure 23. Typical supersonic compressor cascade overall loss curve

suggests that unstarted cascade performance is of the greatest practical importance to a compressor designer.

Engine operation in the "medium" back pressure regime is not uncommon, however. This could occur in a transient mode, as the result of an engine deceleration from an unstarted condition, or the steady-state operating point could be placed here to provide additional stall margin. Steady-state engine operation in the "low" back pressure regime is typically undesirable because the efficiency is poor there.

4. A Cascade Experiment

It is imperative that some means be available to assess the accuracy of any new mathematical model before it is employed in the design of new hardware, and it is clearly desirable to use actual measurements in this validation process. It is also possible to augment the available measurements with Navier-Stokes analyses to obtain information which was not measured in the original experiment. Both of these methods have been employed in the present research, and will be discussed in this chapter and the next.

The blade sections that are considered in the present investigation are the L030-4 and L030-6 profiles which were tested at the DFVLR (now DLR) in Germany. These are the 45% span and 68% span of the L030 transonic research compressor rotor reported by Dunker, et al. (1978) and Dunker and Hungenberg (1980). The major blade geometric parameters and design-point aerodynamic parameters are listed in Table 1.

Details of the experimental facility are given by Schreiber (1980, 1981) and a brief English-language description is given by Schreiber and Starken (1981). This is a continuously-running facility with a flat lower nozzle wall and an adjustable upper nozzle

Table 1. Geometric and design-point aerodynamic parameters for L030 rotor and cascades

	L030-4 45% span	**L030-6 68% span**
γ	48.51°	55.71°
s/c	0.621	0.678
t/c	0.05	0.04
LER/s	0.004035	0.003168
M_1	1.0913	1.2237
M_2	0.7167	0.8110
β_{1m}	58.66°	61.95°
β_{2m}	46.17°	54.03°
P_2/P_1	1.464	1.517

wall. This configuration allows the Mach number to be varied during test operation up to a value of 1.4. The test section consists of 6 blades with 90mm (3.54in) chord length and 167mm (6.57in) span, as shown in Figure 24. The sidewall boundary layer is removed upstream of the test section by applying suction to a single slit. The upper wall of the test section is slotted and has suction applied to prevent wave reflections from destroying the inlet flow uniformity. The lower tailboard is slotted to prevent wave reflections from destroying the exit flow periodicity.

The sidewall suction system used to maintain flow quality was qualitatively similar for both cascades, although minor differences were required to accommodate the blade profile differences. A series of parallel slots was machined through the inner cascade sidewall, as shown in Figure 25 for the L030-6 cascade. Suction was applied to the gap between the slotted inner wall and the solid outer wall to control the sidewall boundary layers. The slots were staggered at approximately the arithmetic average of the

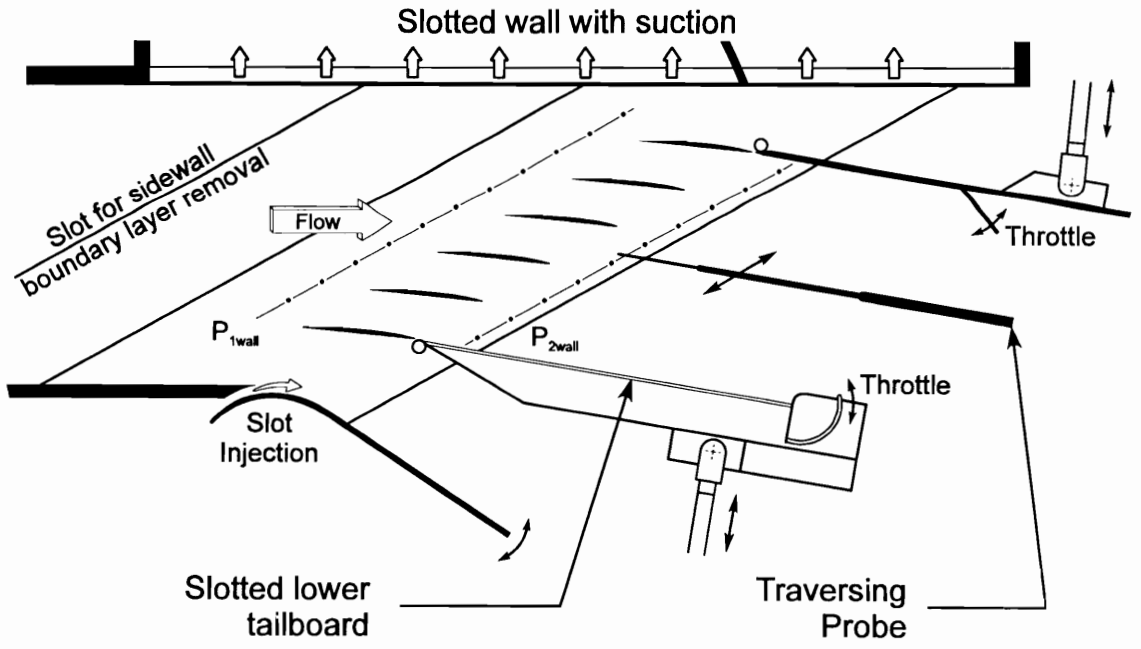

Figure 24. Wind tunnel test section for L030-4 and L030-6 cascades (Schreiber, 1980)

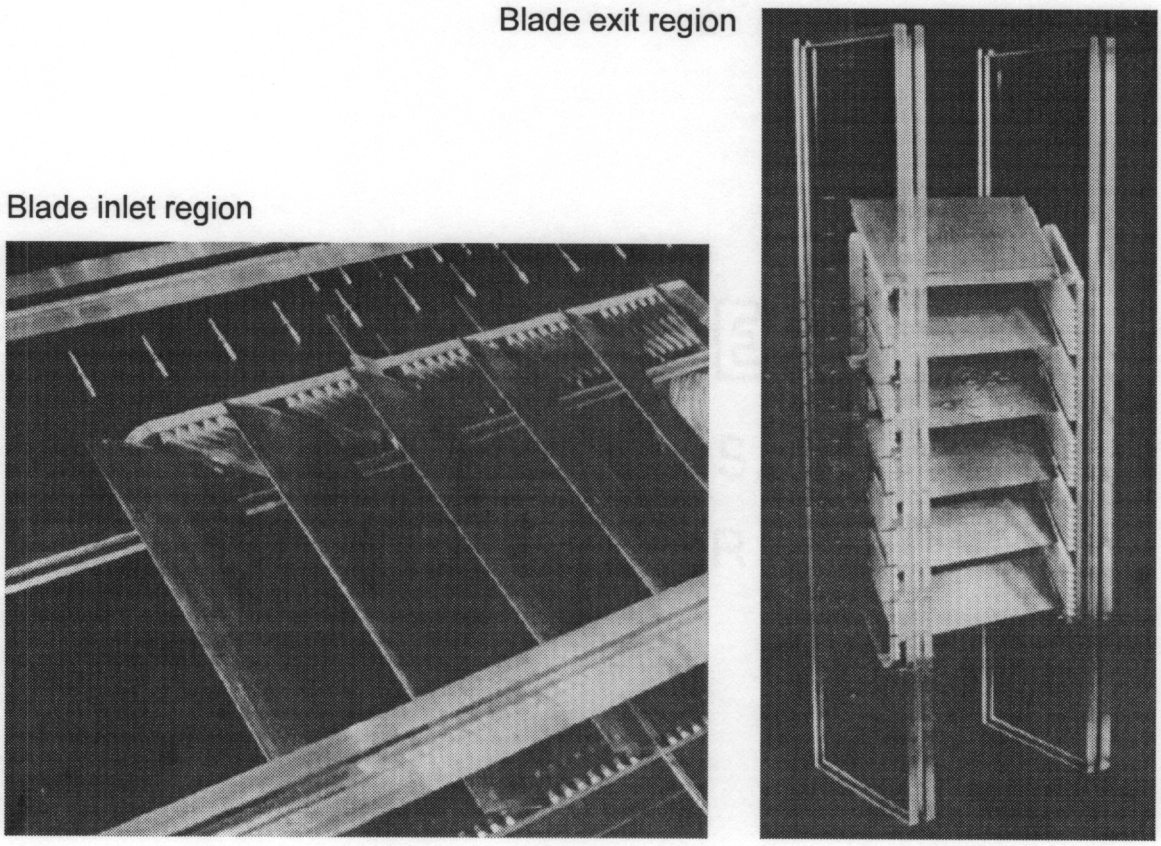

Figure 25. L030-6 Blades installed in cascade sidewalls (Schreiber, 1980)

trailing-edge suction-surface and pressure-surface blade angles. Seven slots were used for the L030-6 cascade and 6 for the L030-4.

It is customary for cascade measurements to be presented as the "mixed-out" values which would exist if a constant-area mixing process were to occur between the measurement plane and a hypothetical plane downstream where the flow field is uniform. For a stationary cascade, the energy equation reduces to

$$T_{01} \equiv T_{02} \tag{42}$$

The continuity, axial momentum, and tangential momentum equations

$$\dot{m} = \int_{y_0}^{y_0+s} \rho_2 W_2 \cos\beta_2 dy = \overline{\rho}_2 \overline{W}_2 s \cos\overline{\beta}_2 \tag{43}$$

$$I_x = \int_{y_0}^{y_0+s} \left(\rho_2 W_2^2 \cos^2\beta_2 + P_2\right) dy = \left(\overline{\rho}_2 \overline{W}_2^2 \cos^2\overline{\beta}_2 + \overline{P}_2\right) s \tag{44}$$

$$I_\theta = \int_{y_0}^{y_0+s} \left(\rho_2 W_2^2 \cos\beta_2 \sin\beta_2\right) dy = \overline{\rho}_2 \overline{W}_2^2 s \cos\overline{\beta}_2 \sin\overline{\beta}_2 \tag{45}$$

are then combined to obtain a quadratic equation which is solved for W_2 (Schreiber, 1980; Schreiber, 1981; Schreiber and Tweedt, 1987)

$$\overline{W}_2 = \sqrt{\frac{2\gamma}{\gamma+1}\left[\left(\frac{I_\theta}{\dot{m}}\right)^2 + \frac{\gamma}{\gamma+1}\left(\frac{I_x}{\dot{m}}\right)^2 - RT_{01} \pm \sqrt{\frac{1}{\gamma+1}\left(\frac{I_x}{\dot{m}}\right)^2\left[(\gamma-1)\left(\frac{I_\theta}{\dot{m}}\right)^2 + \frac{\gamma^2}{\gamma+1}\left(\frac{I_x}{\dot{m}}\right)^2 - 2\gamma RT_{01}\right]}\right]} \tag{46}$$

The negative sign in front of the radical is used for subsonic exit flow. This "mixed-out" velocity is then used to calculate the "mixed-out" flow angle, density, static pressure, total pressure and total pressure loss coefficient as follows.

$$\overline{\beta}_2 = \cos^{-1}\left(\frac{I_\theta}{I_x \overline{W}_2}\right) \tag{47}$$

$$\overline{\rho}_2 = \frac{\dot{m}}{\overline{W}_2 s \cos\overline{\beta}_2} \tag{48}$$

$$\overline{P}_2 = \frac{I_x}{s} - \overline{\rho}_2 \overline{W}_2^2 \cos^2\overline{\beta}_2 \tag{49}$$

$$\overline{P}_{02} = \left(\frac{\overline{\rho}_2 R T_{01}}{\overline{P}_2} \right)^{\frac{\gamma}{\gamma-1}} \tag{50}$$

$$\overline{\omega} = \frac{P_{01} - \overline{P}_{02}}{P_{01} - P_1} \tag{51}$$

An approximate method of quantifying the fractions of the overall loss that is the result of the viscous blade boundary layer and the passage shock system has been presented by Schreiber (1987). The edges of the viscous wake region are determined from the traverse measurements, as shown in Figure 15 (page 46), and the profile loss is calculated by area-averaging the local total pressure loss coefficient (Schreiber and Tweedt, 1987).

$$\omega_{profile} = \int_{y_{ps}}^{y_{ss}} \omega dy - \frac{1}{s} \left(\frac{\omega_{y_{ps}} + \omega_{y_{ss}}}{2} \right) \left(y_{ss} - y_{ps} \right) \tag{52}$$

ref_page_eq_profile_loss_coefficient)An implicit assumption in the use of this method is that area-averaging the local total pressure loss coefficient yields approximately the same value as the "mixed-out" loss coefficient. The present author integrated the measured wakes from 19 of the operating points reported by Schreiber and Tweedt (1987) and noted a maximum difference of 0.0025 between results of the 2 methods. This suggests that area-averaging the local loss coefficient is a reasonable approximation within the present context. The shock loss is then calculated as the difference between the "mixed-out" overall loss and the approximated value of profile loss.

$$\omega_{shock} = \overline{\omega} - \omega_{profile} \tag{53}$$

Schreiber (1987) used this method to determine the shock loss and profile loss portions of the overall loss for the L030-4 and L030-6 cascades over a range of operating conditions, as shown in Figure 26. This clearly forms an excellent basis for validating a shock loss model, since these are actual measurements of the phenomenon of interest. The trend of increasing shock loss with increasing Mach number (at constant inlet flow angle) is clear. The variation of shock loss with inlet flow angle (at constant Mach number) is not clear, however, because measurements were presented for only 2 or 3 flow angles for each Mach number. Navier-Stokes analysis tools can be of some help in determining this variation, and this will be the subject of the next chapter.

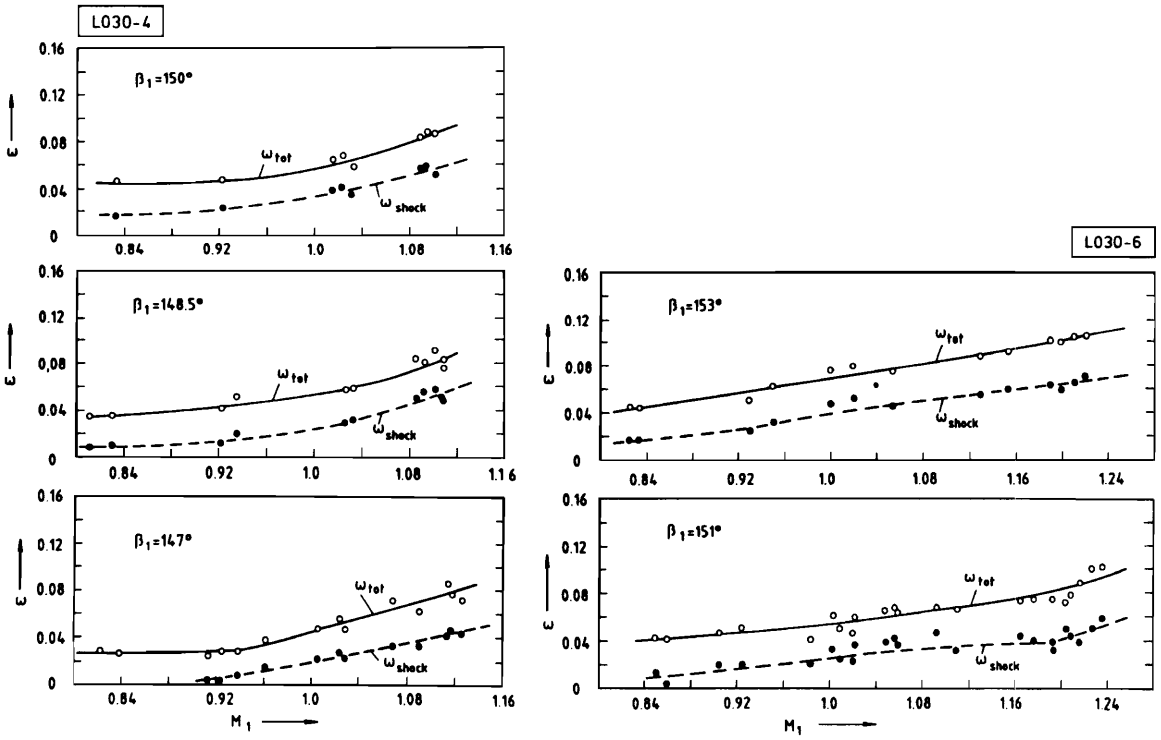

Figure 26. Influence of inlet Mach number and inlet flow angle on measured total pressure losses and corresponding shock losses for the L030-4 and L030-6 cascades (Schreiber, 1987)

5. A Navier-Stokes Analysis

In an effort to improve the understanding of the qualitative variation of shock loss between the known measurements, a Navier-Stokes flow analysis of the L030-4 and L030-6 cascades has been conducted. This analysis used the RVCQ3D (**R**otor **V**iscous **C**ode **Q**uasi-**3**-**D**) solver developed for the analysis of blade-to-blade flows in turbomachinery (Chima, 1987; Chima, et al., 1987). Because viscous grids are typically much finer normal to the blade than in the streamwise direction, all viscous derivatives in the streamwise direction are dropped for lack of resolution. This is commonly referred to as the "thin shear layer" approximation.

For the current investigation, an explicit 4-stage Runge-Kutta integration scheme was used to march forward in time from an initial guess to a steady-state solution (the number of integration stages is user-specified). A spatially-varying time step and implicit residual smoothing were used to accelerate convergence, and the Baldwin-Lomax turbulence model was used. Because the blade-chord Reynolds numbers in the cascade experiment were in the range of $1.5-2.0\times10^6$, the flow was assumed to be turbulent everywhere. The code uses a fourth difference artificial dissipation term to prevent odd-even decoupling and a second difference artificial dissipation term for shock capturing. The method is generally second order accurate, although it reduces to first order near shocks.

5.1 Grid Generation

Grid generation was not the focus of the current research, so this section is not intended to be a tutorial or detailed review on the subject. A somewhat nonstandard approach was taken to obtain the grids used in this investigation, however, and it is

appropriate to outline that approach. It is hoped that this material is presented in a way that does not require advanced understanding of grid generation techniques.

The RVCQ3D code uses a body-fitted (ξ, η) C-type grid which is typically generated using a version of the GRAPE code developed by Sorenson (1981). The ξ index is in the streamwise direction and the η index is in the normal-to-blade direction, as shown in Figure 27. The $\eta = 0$ line starts at point *a* for $\xi = 0$ and moves upstream with increasing ξ. The blade trailing edge is located at point *b*, and the blade surface points are ordered clockwise around the blade from this point. The inlet boundary extends from point *e* to point *f*, and the exit boundary extends from *d* to *g*. For turbomachinery flows, which are periodic in the y-direction, the periodic boundaries are *de* and *fg*.

C-type grids are quite well suited to the study of isolated airfoils, but highly-staggered transonic compressor cascades present additional challenges. Because the axial component of the inlet flow is subsonic, the bow waves travel upstream of the blade and the inlet boundary must be far enough upstream to capture them. The additional

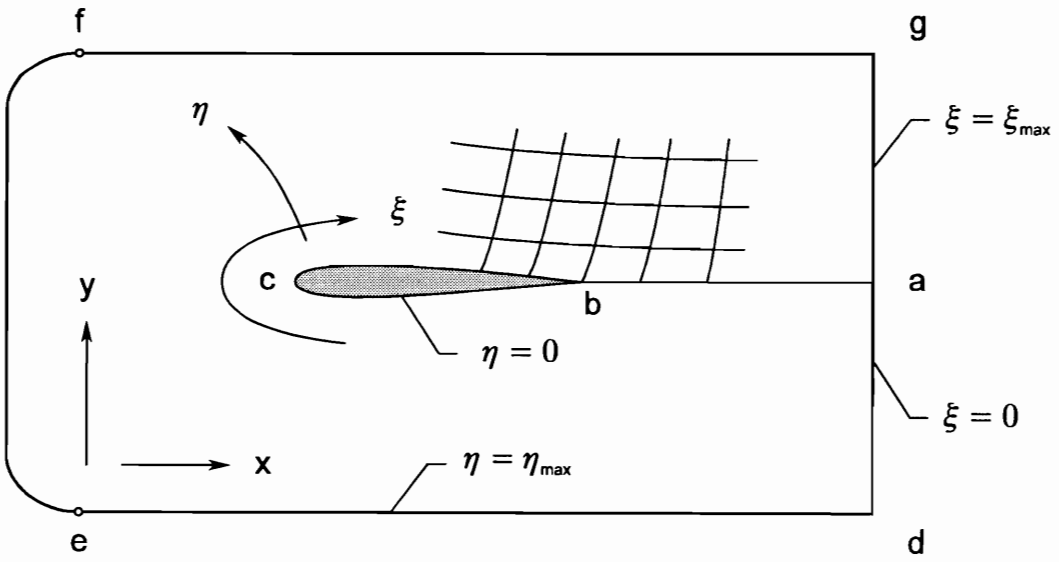

Figure 27. General physical-space topology for C-type grids

requirement to maintain a periodic boundary forces the computational domain to be curved such that the inlet boundary is normal to the axial direction, as shown in Figure 28. Because transonic compressor cascades are highly staggered, this causes the grid to be badly skewed in the inlet region.

Because the GRAPE code was developed for the study of isolated airfoils, the $\eta = \eta_{max}$ boundary is typically generated by evenly spacing the points around the perimeter and forcing the ξ = constant lines to be normal to the boundary. This poses no significant problems for external aerodynamics because the grid outer boundary can be arbitrarily large. But the clustering of grid points at the leading and trailing edges, combined with the proximity of the grid outer boundary for turbomachinery applications,

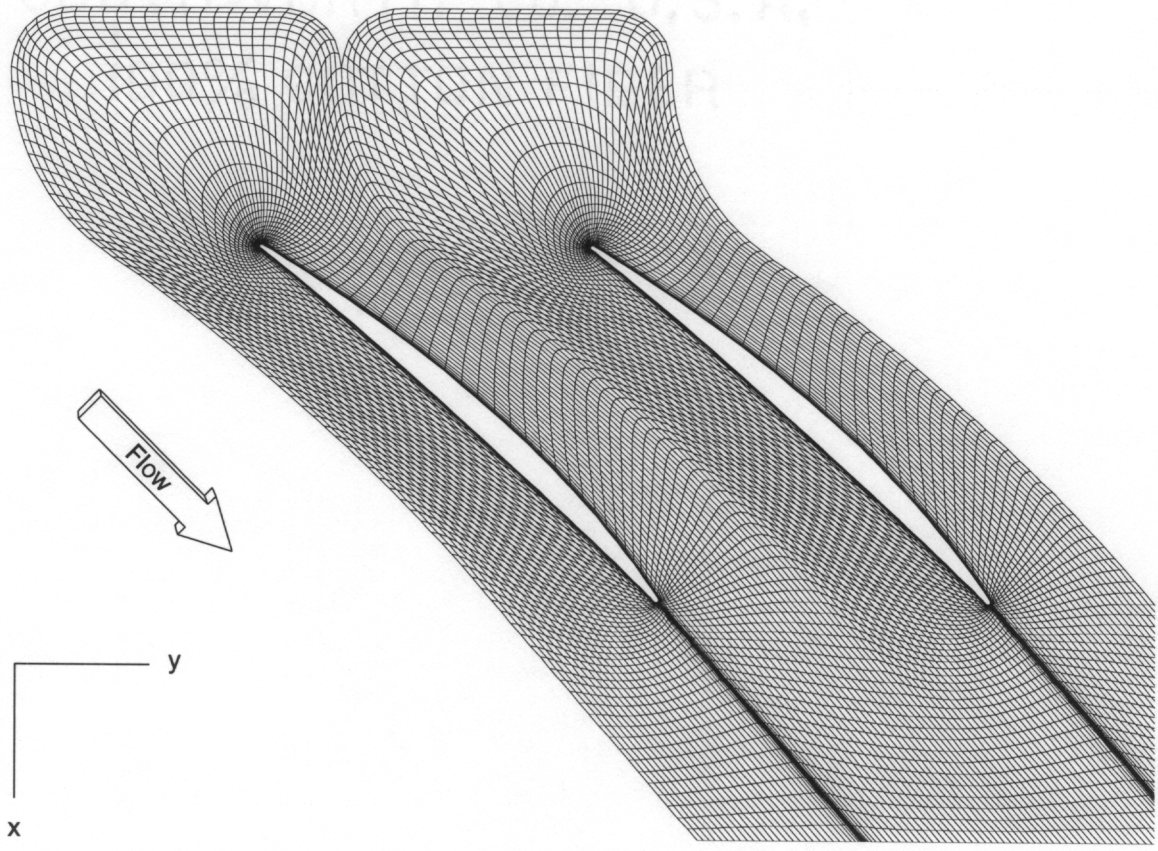

Figure 28. Coarse grid (169x34) for L030-4 cascade using evenly-spaced outer boundary points

produces highly nonuniform cell skewness. Near the leading edge of the blade suction surface, the grid is nearly orthogonal to the streamwise direction, although the cell skewness increases toward the rear of the blade. The grid cells are visibly skewed on the pressure side of the blade, however, more so near the periodic boundary than near the blade surface. This dramatic change in cell skewness at the periodic boundary produces a significant "wiggle" in the passage shock that is not representative of the flow physics, even when the grid density is increased to 449x148.

Because the goal of this Navier-Stokes analysis was to determine shock performance, an attempt has been made to generate grids well suited to shock capturing. While simply increasing the number of grid points can improve the accuracy of a solution, this is an inefficient use of computational resources and does not always have the desired effect. The "art" of grid generation is to cluster the grid points in regions with large flow gradients and allow coarse grid spacing elsewhere. While it is also desirable to have the grid faces be nearly orthogonal to the streamwise direction, this is not always practical or even possible. When the grid cells must be skewed relative to the flow, it is important to minimize the variations in skewness between neighboring cells.

Referring to Figure 28, the current effort increased the number of points on the periodic boundary in the inlet region by reducing the number of points on the inlet boundary. Flow variations are typically expected to be small on the inlet boundary and this was not expected to reduce the overall accuracy of the solution. The spacing of the grid points along the periodic boundary was adjusted to correspond more closely with the blade-surface grid points, thereby generating ξ = constant lines which are more nearly parallel to the y-axis.

To implement these improvements, a computer program was developed to manually specify the x- and y-coordinates and the angle between the ξ = constant lines

and the $\eta = \eta_{max}$ line for every point on the outer boundary. The first step in this process is to run GRAPE to generate a grid with zero-radius corners at the intersection of the inlet and periodic boundaries (points *e* and *f* in Figure 27). A separate program then reads the GRAPE-generated inner boundary (blade coordinates and line *ab* in Figure 27) and outer boundary coordinates and fits a spline to the latter. This spline is then used to determine the y-coordinates at the outer boundary as a function of the desired x-coordinates. The methods used to determine those desired x-coordinates will be discussed next.

Downstream of the blade, the x-coordinates along the periodic boundary are taken from the GRAPE-generated coordinates along line *ab*, resulting in nearly vertical ξ = constant lines. For the points on the blade surface, the $\xi = i$ point on the pressure side of the blade will be connected to the $\xi = \xi_{max} - i + 1$ point on the suction surface of the lower blade. For the points downstream of the leading-edge grid clustering and upstream of the trailing-edge clustering, the x-coordinate along the periodic boundary is simply the arithmetic average of the 2 blade surface coordinates.

It is common to cluster the blade coordinates near the leading and trailing edges to resolve the flow details in these areas. If the "arithmetic average" method discussed above were used near the leading and trailing edges, there would be a dramatic change in the grid spacing at the periodic boundary immediately upstream and immediately downstream of the blade. To avoid this problem at the rear of the blade, uniform grid spacing was used from 8 grid points upstream of the trailing edge to 30 points downstream of the trailing edge. In the inlet region, the following exponential stretching was used on the forward-most 31 points on the periodic boundary

$$x_k = x_{20} - (x_{20} - x_{inlet})\left(\frac{k}{32}\right)^{1.5} \tag{54}$$

where x_{20} is the x-coordinate of the 20th point on the periodic boundary downstream of

the blade leading edge; x_{inlet} is the x-coordinate of the points farthest upstream in the computational domain; and k is an index which is 0 at $x = x_{20}$ and 31 at the intersection between the inlet and periodic boundaries (points e and f in Figure 27). The constants used in this stretching function were determined by visually inspecting the grids generated with different values.

The y-coordinates of the upstream-most points (the inlet boundary) are uniformly spaced. The ξ = constant lines are specified to be vertical at every point on the periodic boundaries and horizontal at every point on the inlet boundary.

The outer boundary specification obtained in this manner is then used as input to the GRAPE code to obtain a grid that is better suited to resolving the passage shock. The

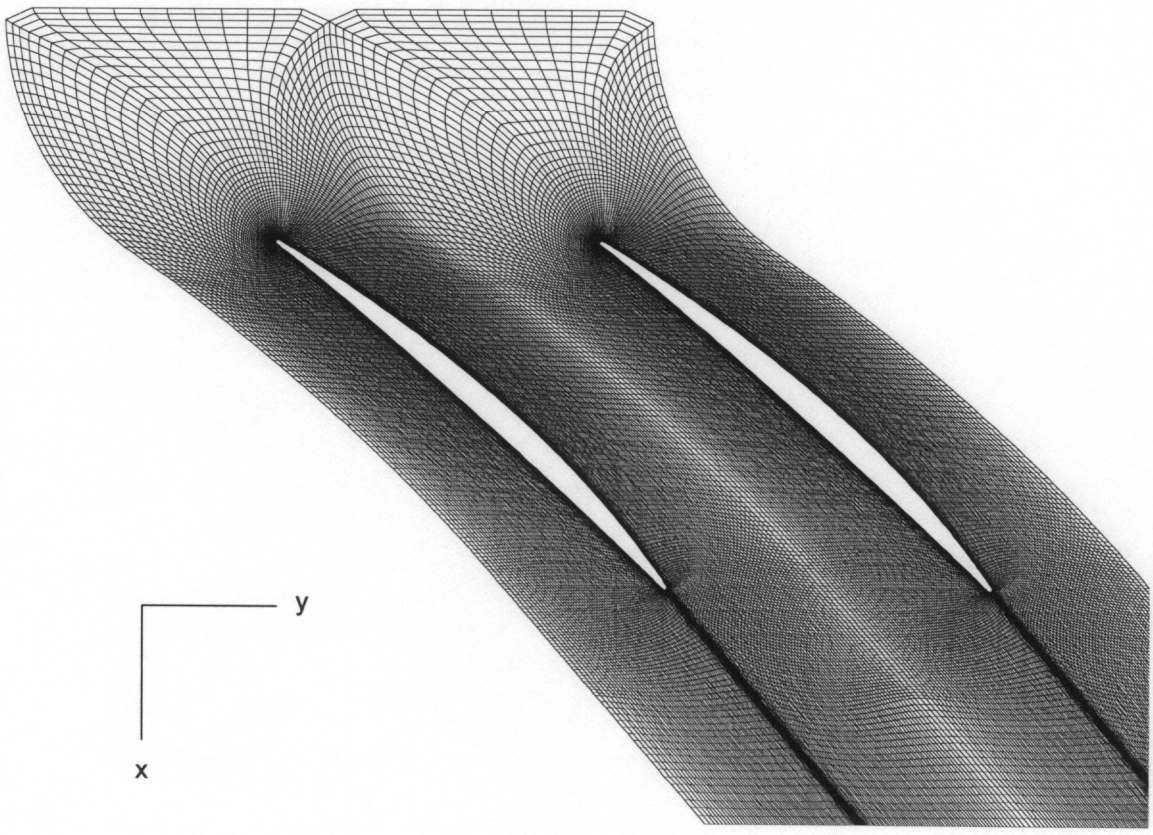

Figure 29. Fine grid (321x70) used in the current investigation for the L030-4 cascade

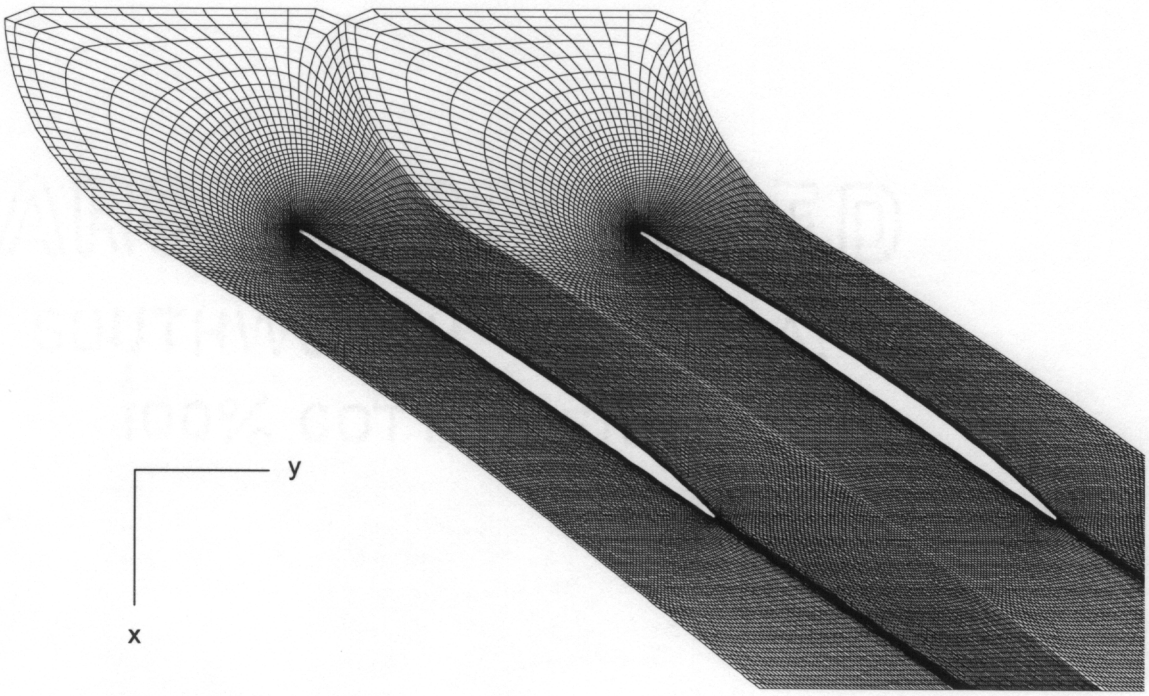

Figure 30. Fine grid (321x70) used in the current investigation for the L030-6 cascade

grids used in the current investigation were generated in this manner and are shown in Figures 29 and 30. It is clear from these figures that the inlet-region grid clustering of the L030-4 grid is more nearly uniform than in the L030-6 grid, and this was intentional.

The number of points in the inlet region is determined by the value of η_{max} and these points can either be clustered near the leading edge or distributed more evenly across the inlet region. A sharper resolution of the passage shock can be obtained by clustering the points near the leading edge, but the strong portion of the bow wave cannot be resolved if it extends across the periodic boundary. Somewhat better resolution of the strong bow wave crossing the periodic boundary can be obtained if the grid points are more uniformly spaced, but this comes at the expense of passage shock resolution.

For the operating points considered during the L030-6 grid refinement studies, the bow shock did not cross the periodic boundary. The grid points were therefore clustered

near the leading edge to sharpen the resolution of the passage shock. The bow shock did cross the periodic boundary for the L030-4 cascade, however, because it had a larger leading edge radius and was operated at lower Mach numbers. Although the inlet-region grid spacing was more nearly uniform for the L030-4 grid, only marginal resolution could be obtained after the bow wave crossed the periodic boundary. This is because the cells on the suction side of the inlet region for a C-type grid are highly skewed relative to the incoming flow. Much finer grid density is required to resolve a shock when the grid is skewed, and sufficient resolution cannot be obtained in the inlet region of a C-type grid without roughly quadrupling the overall number of points.

The improvement in shock resolution obtained through use of the grid refinements discussed above are shown in Figure 31 for the L030-6 cascade with inlet Mach number of 1.20 and static pressure ratio of 1.57. For the solution shown on the left side of this figure, obtained with the "standard" GRAPE grid clustering, the weak passage shock exhibits a change in curvature at the periodic boundary that is not representative of the known flow physics. Furthermore, the second passage shock is not as sharply resolved on the pressure side of the passage as on the suction side, and has a slight "wiggle" at the periodic boundary. These are both results of the badly skewed grid cells on the pressure side of the passage, as identified in Figure 28 (page 72). These shock structure anomalies have been almost completely eliminated through the use of the present grid refinements, as shown in Figure 31b.

5.2 Streamtube Contraction

The RVCQ3D code is quasi-3-dimensional in that it allows the user to specify a variation of streamtube height as a function of axial position, as shown in Figure 32 (page 79). This variation, specified as a series of (x, h) pairs, might typically be obtained

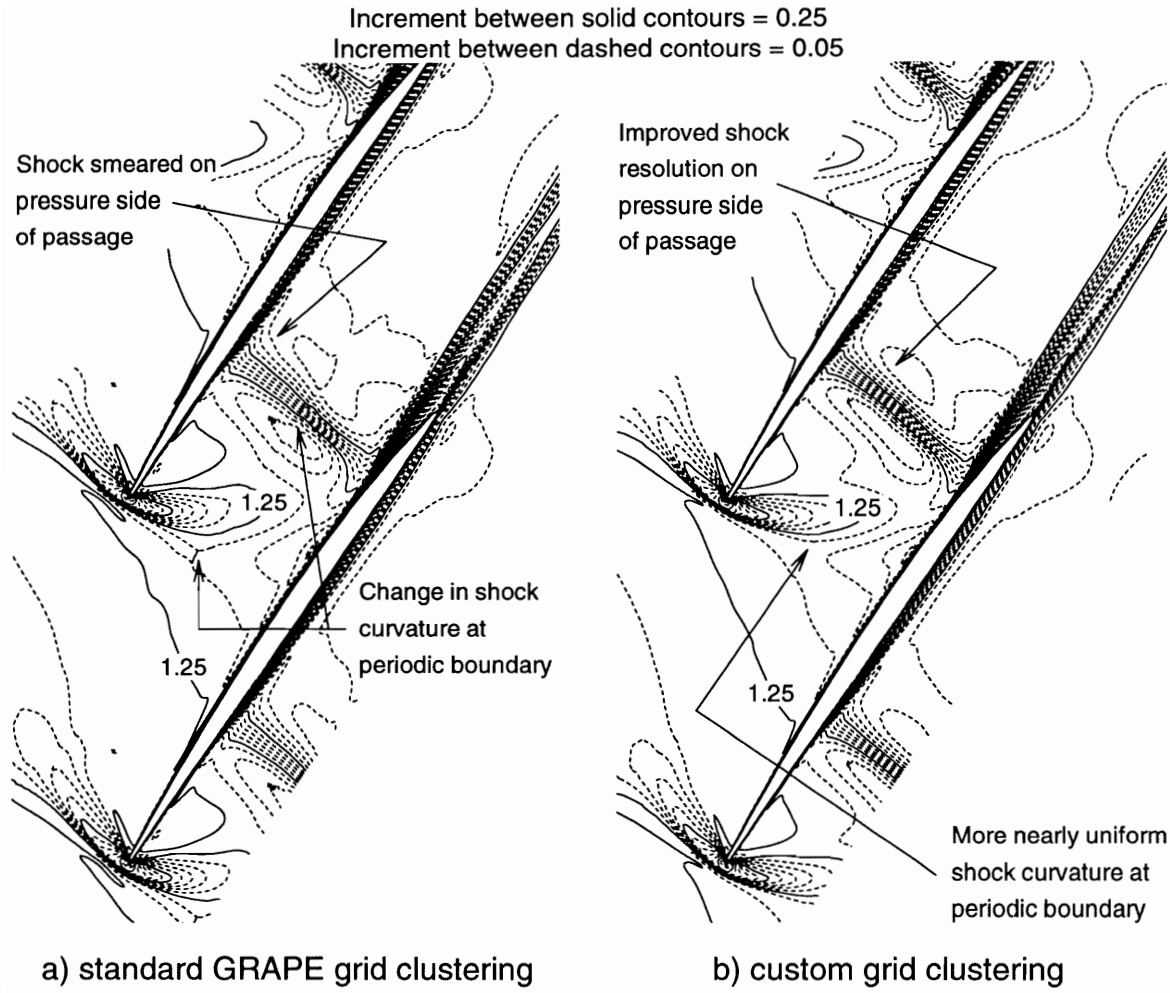

Figure 31. Improvement in passage shock resolution obtained from custom grid specification for L030-6 cascade with M_1 = 1.20 (both grids were 321x70)

from an axisymmetric throughflow calculation. Because streamtube convergence has a first-order effect on the measured flow properties and on the CFD solutions, an attempt was made to include this effect in the present Navier-Stokes analysis. It will be shown in a later section, however, that this attempt was not entirely successful.

There is some ambiguity in the modeling of streamtube contraction for 2-dimensional cascades with AVDR variation. The cascade sidewalls are parallel and essentially solid, and the AVDR variation is generally the result of sidewall boundary

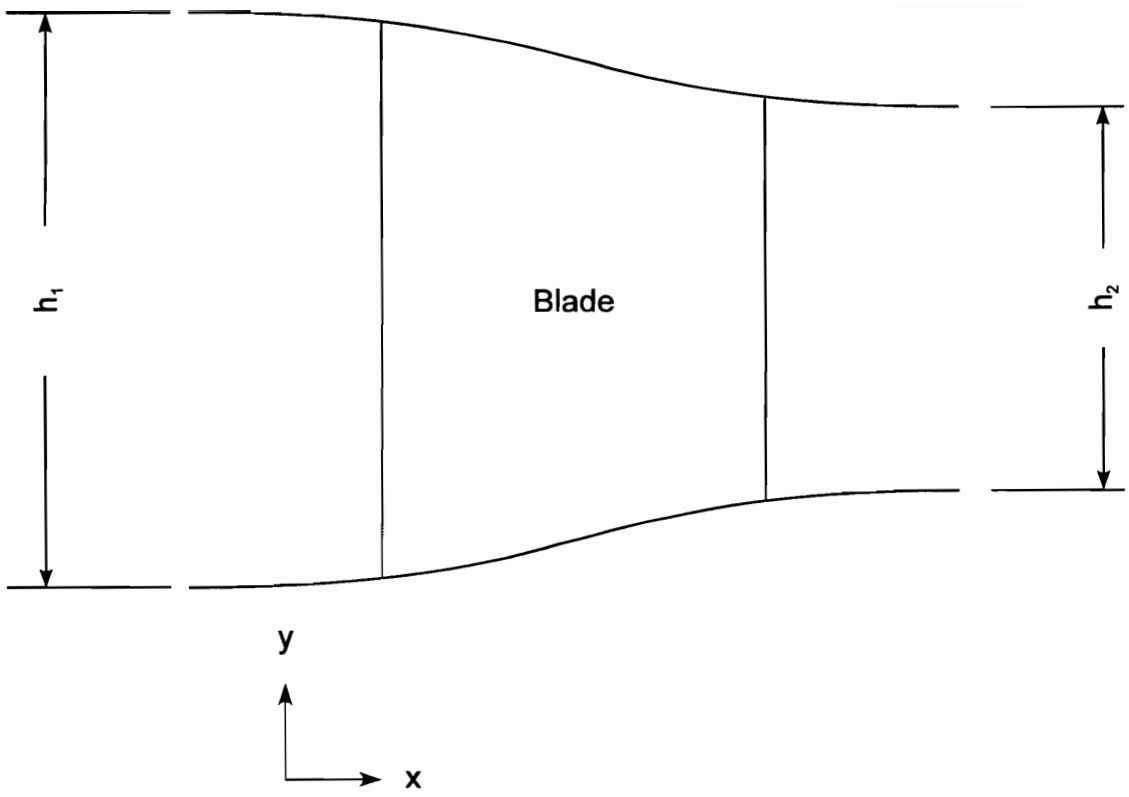

Figure 32. Variation of streamtube height as RVCQ3D input

layer growth. In the absence of sidewall suction, the passage shock would likely produce a nearly discontinuous change in the sidewall boundary layer. Because the RVCQ3D code fits a spline to the user-input endwall variation, however, a step-change in streamtube height would cause wild variations in endwall slope near the discontinuity. (The magnitude of the streamtube height is unimportant, only its x-derivative affects the solution).

An effective suction system will help stabilize the sidewall boundary layer, but the extent of this stabilization is not known because the boundary layer growth is typically not measured inside the blade passage. Because the passage shock spans some range of axial coordinate, however, it is reasonable to suggest that the effective passage height variation is actually 3-dimensional in spite of the solid cascade sidewalls. The passage

shock position is also known to be a function of Mach number, incidence, and back pressure, and this suggests that the actual variation of effective streamtube height inside the blade passage is likely to be operating-point dependent. Because the RVCQ3D code requires a unique x-h relation, it would be difficult to model this variation even if it were known exactly.

Some judgment clearly must be applied when specifying the effective passage height variation for 2-dimensional cascades. The sidewall boundary layer growth upstream of the passage shock is likely to be small compared to the growth which occurs downstream. The *differences* in the entrance-region sidewall boundary layers caused by changes in AVDR will likely be very small and are neglected in the current investigation. Because the passage shock begins slightly upstream of the blade leading edge and spans a range of axial coordinate, the streamtube contraction was assumed to begin at the leading edge. To obtain a smooth variation, the effective streamtube height was modeled as a cubic polynomial with a value of 1 at the blade leading edge and $1/AVDR$ at the exit boundary. An inflection point was specified near the blade trailing edge with a slope of -10, and this produced the effective sidewall variation shown in Figure 33 for the L030-6 cascade with $AVDR = 1.20$. The only justification for the location and slope of the inflection point is that it produced a variation that "appears" smooth and reasonable, although it is difficult to assess the validity of this specification with any degree of certainty.

5.3 Specification of Solver Boundary Conditions

For axially subsonic inlet conditions, the user specifies the total pressure, total temperature, Mach number, and relative flow angle at the inlet boundary. The latter 3 quantities are used to calculate the inlet circumferential velocity, V_θ, and the solver

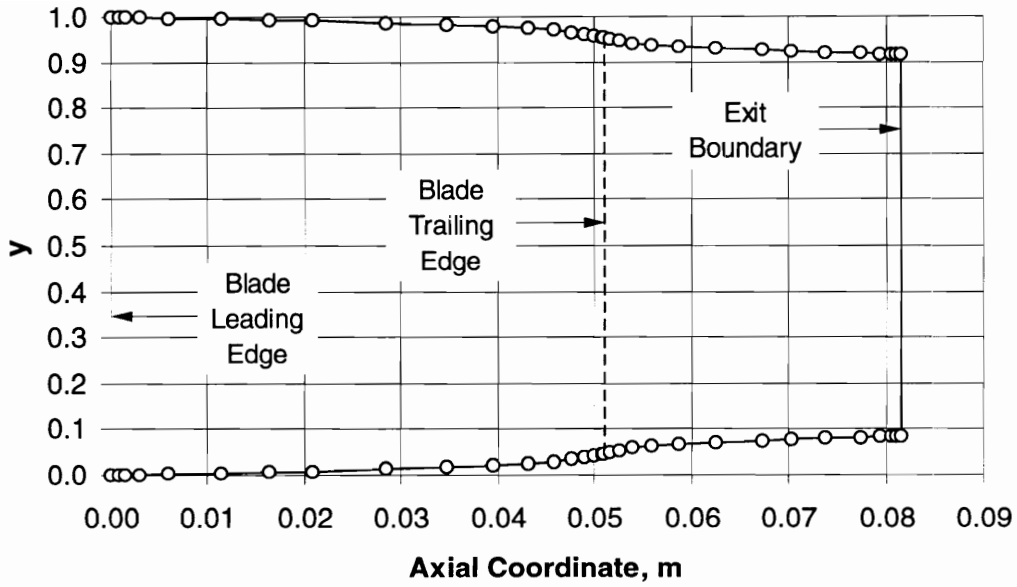

Figure 33. Effective sidewall variation used as input to CFD for L030-6 cascade with *AVDR* = 1.20

conserves that V_θ value at the inlet boundary. For axially subsonic exit conditions, the user specifies the exit plane area-averaged static pressure.

If the specified exit pressure is low enough for the cascade to be started, the solver automatically calculates the started inlet conditions for the specified V_θ. Because the exact minimum-incidence angle is not known *a priori*, this typically requires some iteration to obtain the correct inlet boundary conditions. Suppose, for example, that the user wants to obtain started operating points for an inlet Mach number of 1.200 and that the started inlet flow angle for this cascade and Mach number is 61.013° ($V_{\theta 1} = 321$ m/s for $T_{01} = 300$ K). If a first guess for the inlet flow angle is 62°, this yields $V_{\theta 1} = 324$ m/s and the solver will return a higher-than-desired upstream Mach number, perhaps $M_1 = 1.214$. If the inlet flow angle is guessed to be 60° ($V_{\theta 1} = 318$ m/s), the solver will return a lower-than-desired value, perhaps $M_1 = 1.186$. Once the correct inlet boundary

conditions are obtained, typically within 4 or 5 iterations, they are held fixed while the back pressure is varied to obtain the started portion of the characteristic.

If the specified back pressure is high enough, the solver will calculate an unstarted solution. In this case, the desired inlet Mach number and flow angle are held fixed while the back pressure is varied to obtain the desired operating point. If the user specifies a back pressure that is too low, the solver calculates a higher-than-desired Mach number and a lower-than-desired inlet flow angle. If the exit pressure is guessed too high, the solver calculates a lower Mach number and higher flow angle. If the desired operating point is near stall, the solver may not converge if the back pressure is specified too high.

5.4 Convergence Criteria

The solution convergence histories were generally well-behaved, although they varied dramatically with operating condition. Solutions for started operating points generally approached convergence much more quickly than for unstarted operation unless the started condition contained a shock-induced boundary layer separation. The convergence history for a typical started operating point of the L030-6 cascade is shown in Figure 34. The reduction in density residuals, shown in the upper part of this figure, is about 3 orders of magnitude. While this is only a "fair" reduction, it is fairly typical of viscous solutions. It is believed that local unsteadiness effects in the viscous region cause the associated local residuals to remain fairly large (Chima, 1996), but the overall quality of the solution is still believed to be good because both mass and energy are conserved. It is shown in the middle part of this figure that the error in these conservation quantities is less than 0.1% after about 1400 iterations. Chima (1996) has suggested that 0.1% error for these conservation quantities is a fairly strict convergence criteria and indicates that the solution is most likely correct. The total pressure loss coefficient, shown in the

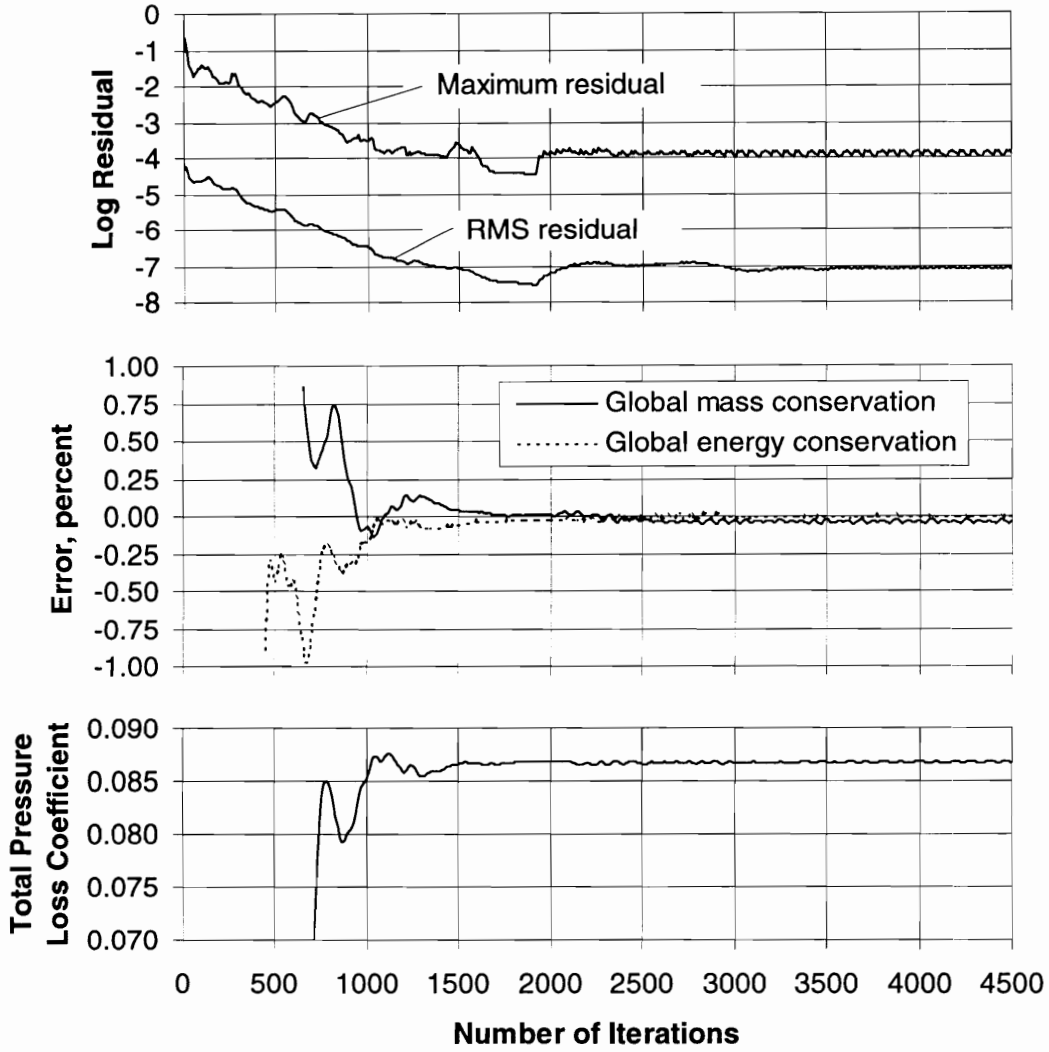

Figure 34. Convergence history of an RVCQ3D computation for started operation of the L030-6 cascade

bottom part of this figure, also reaches an essentially constant value after about 1500 iterations; although not shown, the predicted exit flow angle and exit Mach number are similarly well-behaved.

The approach to assessing convergence for unstarted operation is somewhat different than for started conditions. As mentioned earlier in this chapter, the RVCQ3D code integrates in time from an initial guess to a steady-state solution. As the solution

marches forward in time, the inlet Mach number decreases and the inlet flow angle increases until the steady-state conditions are reached. Unlike started operation, however, up to 15,000 iterations may be required to reach the unstarted steady state.

It is possible to accelerate the process of obtaining a "converged" unstarted solution by relaxing the definition of "steady-state." If an exit pressure higher than the steady-state (15,000 iterations) value is specified, the time integration of the solution will pass through the desired operating condition after fewer iterations. The number of iterations required to obtain the desired operating condition is shown as a function of back pressure in Figure 35, as are the other major exit flow parameters for each solution. It should be noted that these solutions for 2500 and fewer iterations failed the criteria of 0.1% errors in mass and energy conservation, and should be considered unreliable. The solutions for 3000 and more iterations, however, met this criteria and are more likely to be correct. Comparison of the variation in the exit flow parameters for these solutions with the wind tunnel facility uncertainties, presented in Table 2, shows that the flow parameter variations are smaller than the measurement uncertainties. This suggests that any solution run for a sufficient number of iterations to reduce the mass and energy conservation errors below 0.1% will be correct within the engineering accuracy of the method.

Table 2. Calculated uncertainties (95% confidence) for static pressure ratios of about 2.0 and the indicated inlet Mach numbers for the DLR supersonic cascade wind tunnel (Schreiber and Tweedt, 1987)

	Parameter			
Inlet Mach number	P_2/P_1	$\overline{\omega}$	β_2	M_2
1.4	0.168	0.0046	1.5°	0.012
1.6	0.142	0.0046	1.5°	0.012
1.7	0.133	0.0041	1.5°	0.010

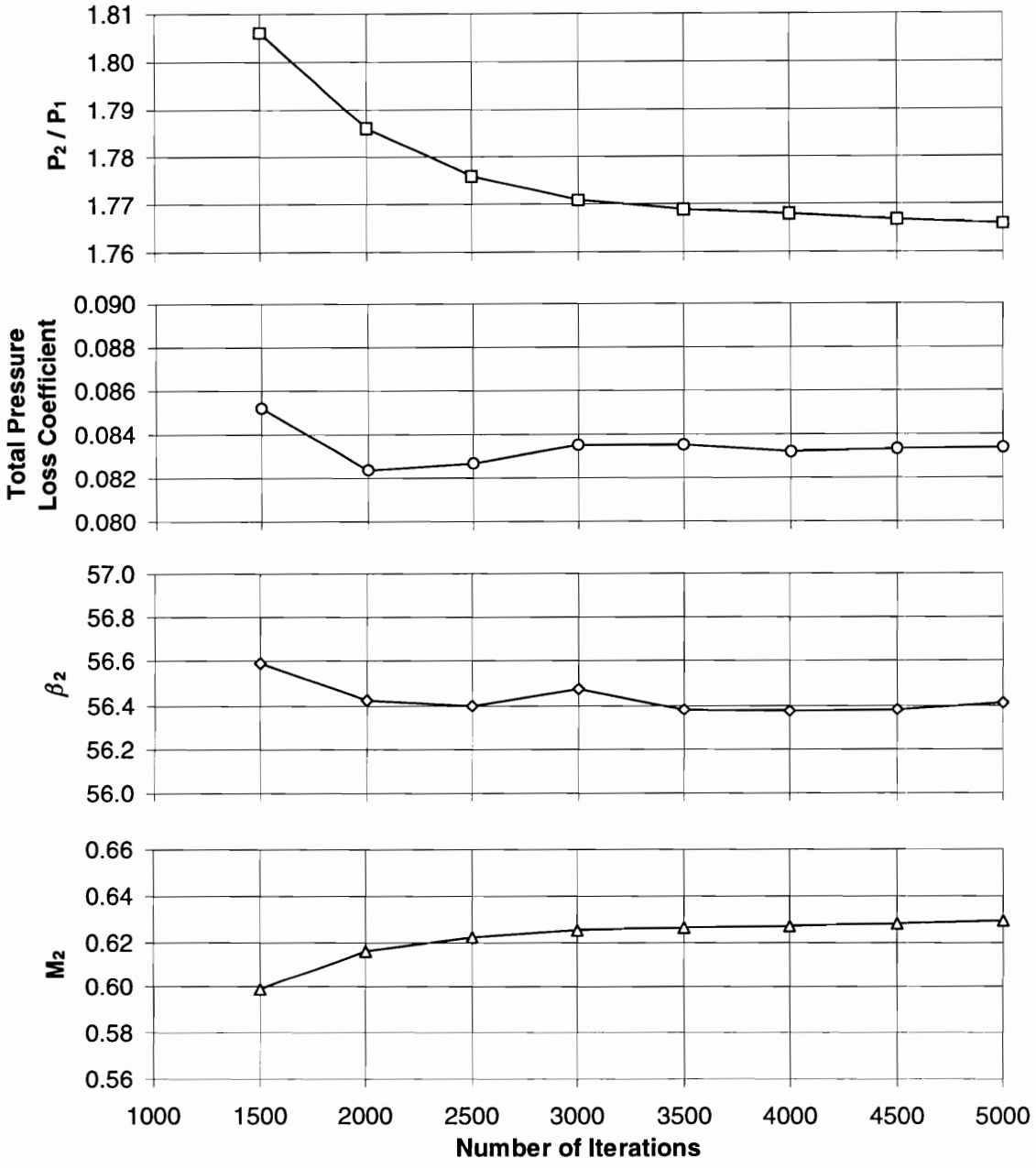

Figure 35. Effect of number of iterations on exit flow parameters for unstarted operation of the L030-6 cascade

For this reason, it was desired to impose 2 criteria to establish the convergence of a solution. The first criteria, that the magnitude of the energy conservation error be less than 0.1% was satisfied for all solutions presented. Although it was desired to establish

the same magnitude criterion for the mass conservation errors, operating conditions which exhibited a shock-induced boundary layer separation were not always this well-behaved. The mass conservation error was less than 0.2% for all solutions presented. Started solutions typically required between 2000 and 3000 iterations to meet these criteria while unstarted conditions typically required 3000 to 3500 iterations. Execution of 3500 iterations of the RVCQ3D code on a Silicon Graphics Power Indigo with a single 75MHz R8000 processor required 17 minutes of CPU-time for the 321x70 grids used.

5.5 Post-Processing to Calculate Losses

The "mixed-out" losses were calculated from the CFD solutions in a manner similar to that presented in the previous chapter, although some of the details were handled differently. As shown in Figures 28 through 30, the exit-plane grid spacing is much finer near $\eta = 0$ (point *a* in Figure 27) than near $\eta = \eta_{max}$ (periodic boundary). In general, the viscous blade wake region does not follow the dense grid spacing downstream of the blade. This results in fine grid spacing in the region of small flow gradients and vice versa. In an attempt to increase the number of integration points located within the wake, splines were fit to the flow variables at the grid exit plane. These splines were then evaluated at evenly-spaced increments across the blade passage to perform the integration. While this did increase the number of integration steps within the wake region, the 321x70 grid resolution was fine enough that this step had a negligible effect on the integrated values.

The "mixed-out" exit velocity was calculated by combining the mass, momentum, and energy equations to obtain a quadratic in $\overline{W}_2 \cos\overline{\beta}_2$, after Pianko and Wazelt (1983).

$$\overline{W}_2^2 \cos^2\overline{\beta}_2 - \frac{2\gamma}{\gamma+1}\left(\frac{I_x}{\dot{m}}\right)\overline{W}_2 \cos\overline{\beta}_2 + 2\left(\frac{\gamma-1}{\gamma+1}\right)\left\{c_p T_{01} - \frac{1}{2}\left(\frac{I_\theta}{\dot{m}}\right)^2\right\} = 0 \qquad (55)$$

The above quadratic has the following solution.

$$\overline{W}_2 \cos\overline{\beta}_2 = \frac{\gamma}{\gamma+1}\left(\frac{I_x}{\dot{m}}\right) \pm \sqrt{\left[\frac{\gamma}{\gamma+1}\left(\frac{I_x}{\dot{m}}\right)\right]^2 - 2\left(\frac{\gamma-1}{\gamma+1}\right)\left\{c_p T_{01} - \frac{1}{2}\left(\frac{I_\theta}{\dot{m}}\right)^2\right\}} \tag{56}$$

The negative sign in front of the radical is used for subsonic exit flow. The "mixed-out" velocity and flow angle were then calculated as

$$\overline{W}_2 \sin\overline{\beta}_2 = \frac{I_\theta}{\dot{m}} \tag{57}$$

$$\overline{\beta}_2 = \tan^{-1}\left(\frac{\overline{W}_2 \sin\overline{\beta}_2}{\overline{W}_2 \cos\overline{\beta}_2}\right) \tag{58}$$

$$\overline{W}_2 = \frac{\overline{W}_2 \cos\overline{\beta}_2}{\cos\overline{\beta}_2} \tag{59}$$

Equations 48 through 51 (pages 67 and 68) were then used to calculate the remainder of the "mixed-out" flow properties, and the profile loss and shock loss components were calculated from Equations 52 and 53 (page 68).

One of the current limitations of Navier-Stokes codes is a generally poor ability to predict wake mixing, with the predicted wakes almost always "deeper" than the measured wakes (Strazisar, 1995). Consequently, the mixing and loss which follow a boundary layer separation are not accurately predicted. While better prediction of wake mixing is obviously desirable, the narrow wakes predicted by the CFD typically have a local minimum on each side of the wake which can be used to determine the wake edges, as shown in Figure 36. These local minima were used as the bounds of integration for the profile loss calculation.

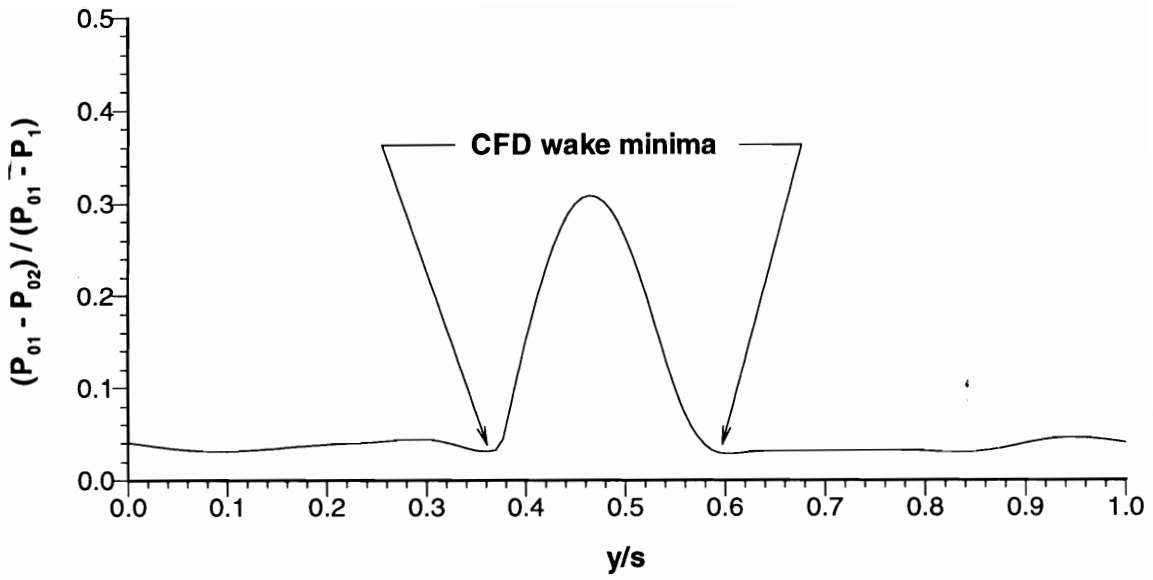

Figure 36. Typical CFD exit-plane wake profile showing local minima used to define edges of wake for viscous profile loss estimation

5.6 Comparison with Measured Data

Although the RVCQ3D code has been widely used in both industrial and research environments for several years, it is appropriate to establish the level of agreement obtained for the current investigation. Ideally, this would be done by comparing a loss bucket generated for a single upstream Mach number and a fixed AVDR. In practice, however, the exit static pressure and the AVDR are strongly coupled and only limited independent variations are possible in the cascade tests. The typical experimental procedure is to set the inlet Mach number and exit static pressure as close as possible to the desired values, and then measure the AVDR obtained from these settings (Schreiber and Tweedt, 1987).

A measured loss bucket generated in this manner for the L030-6 cascade is shown in Figure 37, as are the loss values obtained from the RVCQ3D code. The inlet Mach number for these points ranged from 1.18 to 1.21 and the AVDR varied from 1.03 to

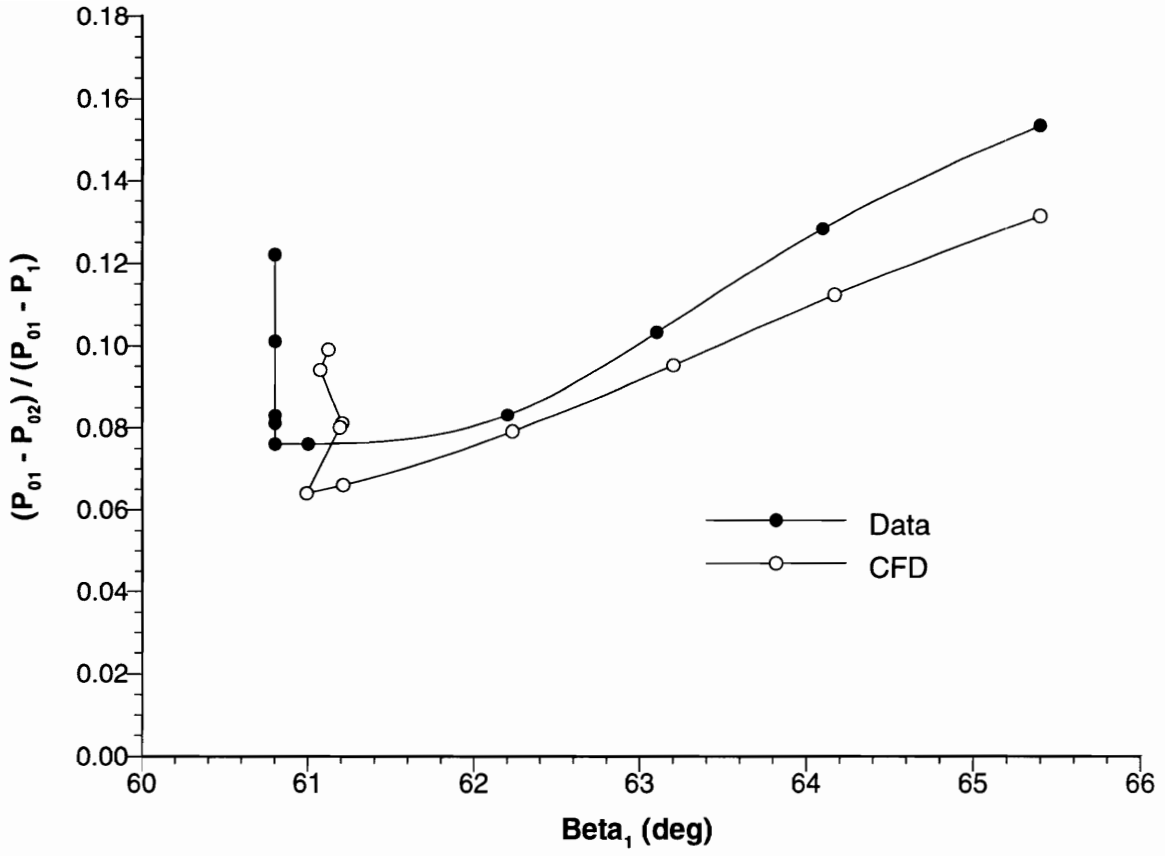

Figure 37. Overall loss measurements for the L030-6 cascade for M_1 = 1.20 compared with CFD predictions (CFD used measured AVDR and M_1 values)

1.26; these variations were included in the Navier-Stokes analyses. The general trends of the loss bucket are reproduced by the CFD, and the magnitude of the differences in loss coefficient are less than 0.013 for all operating points shown except the near-stall and lowest back pressure conditions.

The dramatic increase in loss for the lowest back pressure operating point was not well-reproduced by the CFD, and this was most likely the result of boundary layer separation induced by the second passage shock. As mentioned previously, Navier-Stokes codes are currently unable to accurately calculate loss in regions of separated flow.

Shock-induced boundary layer separation is also believed to contribute to the divergence between the predicted and measured loss curves as stall is approached.

Along the started portion of the characteristic, the variation of inlet flow angle predicted by the CFD was the result of the AVDR specification. Recall that the first captured Mach wave begins on the blade suction surface and extends forward (axially) to the point where the bow shock intersects the stagnation streamline. Because the streamtube contraction was assumed to begin at the blade leading edge, the effective blade height at the rearward-most end (axially) of the first captured Mach wave is smaller than the far-upstream blade height. This decrease in flow area along the first captured Mach wave has the same effect as an increase in blade thickness, and the upstream flow angle increases accordingly.

It is likely that the streamtube convergence has been specified too far upstream for all of the points shown in Figure 37, and that this is at least partially responsible for the consistently low loss predictions. This would be the case if the sidewall suction system employed in the cascade experiment nearly eliminated the sidewall boundary layer growth within the blade passage, and most of the streamtube contraction was confined to the region downstream of the trailing edge. In the present Navier-Stokes analysis, the decreasing flow area between the first captured Mach wave and the passage shock caused the supersonic flow to decelerate, thereby reducing the shock strength and the shock loss. The weaker shock also had a less severe effect on the suction surface boundary layer, thereby reducing the viscous loss.

The preceding comments demonstrate some of the difficulties associated with specifying a variation in streamtube height when the actual variation is not known. Furthermore, no information regarding the AVDR was presented for the shock loss measurements in Figure 26 (page 69). For these reasons, the remainder of the CFD

solutions to be presented were obtained with no variation of streamtube height ($AVDR \equiv 1$). To further isolate the influence of the point-to-point variations of measured inlet Mach number, the variation between points on each CFD loss bucket is limited to $\Delta M_1 \leq 0.001$.

A loss bucket generated with CFD for the L030-6 cascade with $M_1 \equiv 1.200$ and $AVDR \equiv 1$ is compared with the measured losses for $M_1 \cong 1.20$ in Figure 38. By removing the streamtube contraction in the CFD, the agreement with the measured losses has been dramatically improved. This supports the suggestion that the streamtube

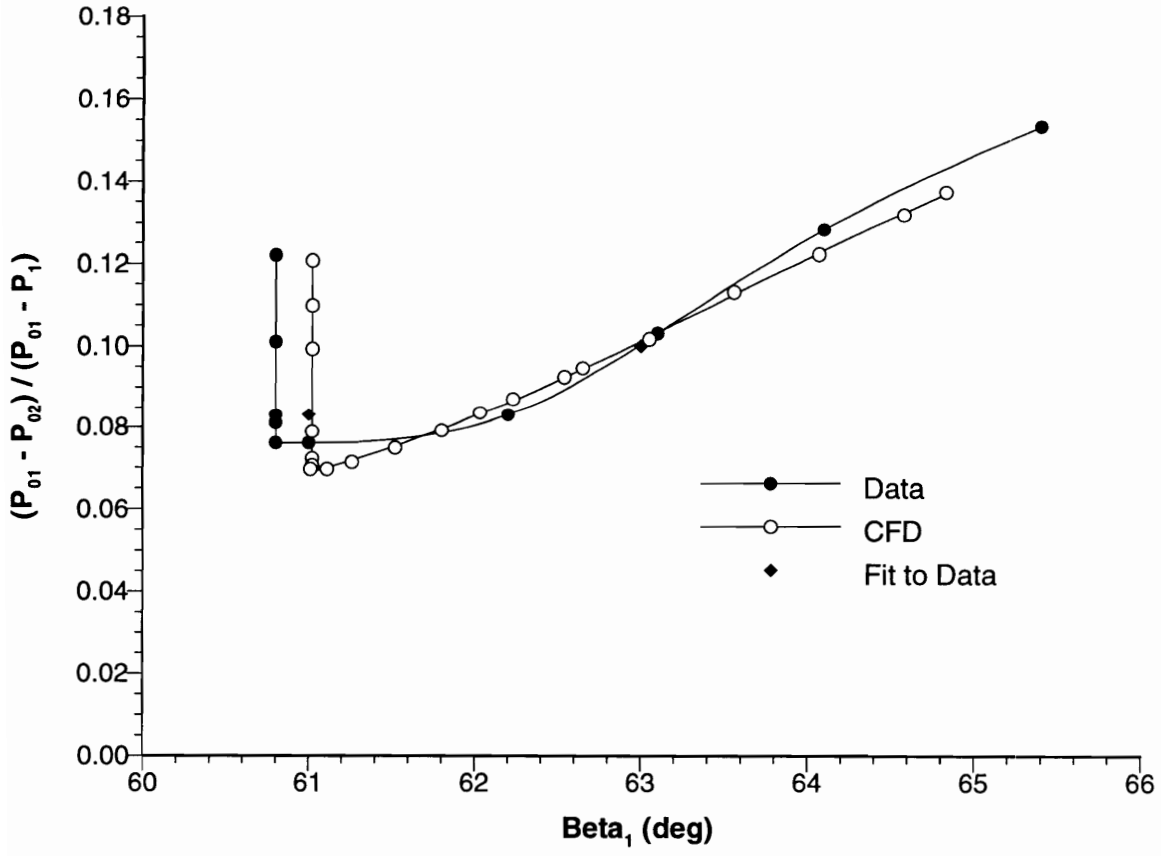

Figure 38. Overall loss measurements for the L030-6 cascade for M_1 = 1.20 compared with CFD predictions (CFD used M_1 = 1.200 and $AVDR$ = 1.000)

contraction in the experiment is likely confined to the region downstream of the blade, although this has not been confirmed through measurements.

In Figure 38, the points labeled "Fit to Data" were obtained by evaluating the solid curves labeled ω_{tot} fit by Schreiber (1987) to the data in Figure 26 (page 69). The overall loss values read from Schreiber's curves for $M_1 = 1.20$ were included to help identify the level of point-to-point variations that are common in the cascade experiments. These variations stem from the manner in which the upstream and downstream boundary conditions are adjusted. The upstream flow angle is specified by physically rotating the cascade to the desired angle prior to operating the wind tunnel. Once the desired inlet Mach number is obtained, the exit-region throttles and tailboards are adjusted to obtain the desired exit pressure and flow periodicity. This is a fairly arduous task because a range of exit pressures can be established for each cascade setting angle, resulting in loss values that span a range of 0.010 to 0.030. Even larger variations are common near stall if boundary layer separations are present.

It is presumed that Schreiber (1987) has exercised appropriate judgment in determining which measurements to present in Figure 26. This discussion has been included, however, to identify the level of scatter that is typical of this type of experiment. This will help to keep the magnitude of the differences between predictions and measurements in perspective.

With this in mind, the CFD solutions appear to provide fairly accurate prediction of the overall loss for the entire operating range of this cascade. This suggests that the RVCQ3D Navier-Stokes analysis tool can be used to supplement the available measurements and that the differences between these predictions and the measurements are likely to be of the same order as the scatter within the measurements.

6. An Engineering Shock Loss Model

An outline of the fluid flow phenomena which exist in supersonic compressor cascades was presented in Chapter 3, although some details were omitted. The present chapter provides the remaining information necessary to obtain a complete shock loss model that is applicable over the entire supersonic flow range of the cascade. Every effort has been made to retain as much of the flow physics as possible, but some simplification and empirical inputs are inevitably required to obtain closure.

The scope of this model is restricted to the total pressure loss produced by the passage shock system that exists in a 2-dimensional supersonic compressor cascade. Viscous effects related to the blade boundary layer and any shock-boundary layer interactions are not addressed. It is not suggested that the viscous mechanisms are unimportant, because they clearly have a significant impact on performance and any ***overall*** performance prediction must include these effects. The scope of the present model, however, is limited to the passage shock mechanism.

The flow upstream of the passage shock is assumed to be steady, inviscid, and supersonic, with a subsonic axial component. The total pressure, total temperature, and Mach number are assumed to be known at the inlet. The present investigation is restricted to stationary cascades, so the total temperature is constant everywhere.

In a cascade with blunt leading edges, the bow shock that stands ahead of each blade extends to infinity and causes some total pressure loss. The vast majority of that loss occurs immediately upstream of the blunt leading edge, where the flow behind the shock is subsonic. For this reason, the left-running characteristics will be curved very near the blade surface and will become more nearly straight as they extend farther from the blade. This curvature of the characteristics is neglected in the present analysis,

although the total pressure loss from the bow shock is included in the continuity equation, as suggested by Starken, et al. (1984).

For all operating conditions, the upstream flow angle, β_1, is obtained by iteratively solving the Prandtl-Meyer and continuity relations, which are duplicated below. The Prandtl-Meyer relation is given by

$$\beta_1 + \nu(M_1) = \beta_A + \nu(M_A) \tag{38}$$

where ν is the well-known Prandtl-Meyer function.

$$\nu(M) = \sqrt{\left(\frac{\gamma+1}{\gamma-1}\right)}\tan^{-1}\sqrt{\left(\frac{\gamma-1}{\gamma+1}\right)(M^2-1)} - \tan^{-1}\sqrt{M^2-1} \tag{39}$$

The continuity relation is given by

$$\dot{m} = \frac{F(M_1)P_{01}s\cos\beta_1}{\sqrt{c_pT_{01}}} = \frac{F(M_A)P_{0A}\left|\overline{AB}\right|\sin\mu_A}{\sqrt{c_pT_{0A}}} \tag{40}$$

where F is the following compressible mass flow function.

$$F(M) = \frac{\dot{m}\sqrt{c_pT_0}}{P_0A} = \frac{\gamma}{\sqrt{\gamma-1}}M\left\{1+\frac{\gamma-1}{2}M^2\right\}^{-\frac{\gamma+1}{2(\gamma-1)}} \tag{41}$$

To complete the incidence calculation, methods must be developed to determine the endpoints of the first captured Mach wave and the properties along this wave. Once the upstream flow angle is known, the shape of the passage shock must be approximated and its performance estimated. These subjects will be treated separately in the following sections.

6.1 A Model for Detached Shocks

A slightly modified form of the method of Moeckel (1949) is used to approximate the shape of the detached shock which stands ahead of the blunt leading edge. Moeckel determined that the shape of an isolated body in a uniform supersonic stream had little effect on the shape of the shock which stands ahead of it. Although experimental results indicated that the shape of the sonic line may depend considerably on the shape of the nose, Moeckel found this variation to be unimportant in determining the shape of the shock. As shown in Figure 39, the sonic line was approximated as a straight line extending from the point where the tangent to the contour of the body is inclined at the wedge angle corresponding to shock detachment, ε_{max}. The shock was then approximated as a hyperbola which is normal to the body at the vertex of the imaginary

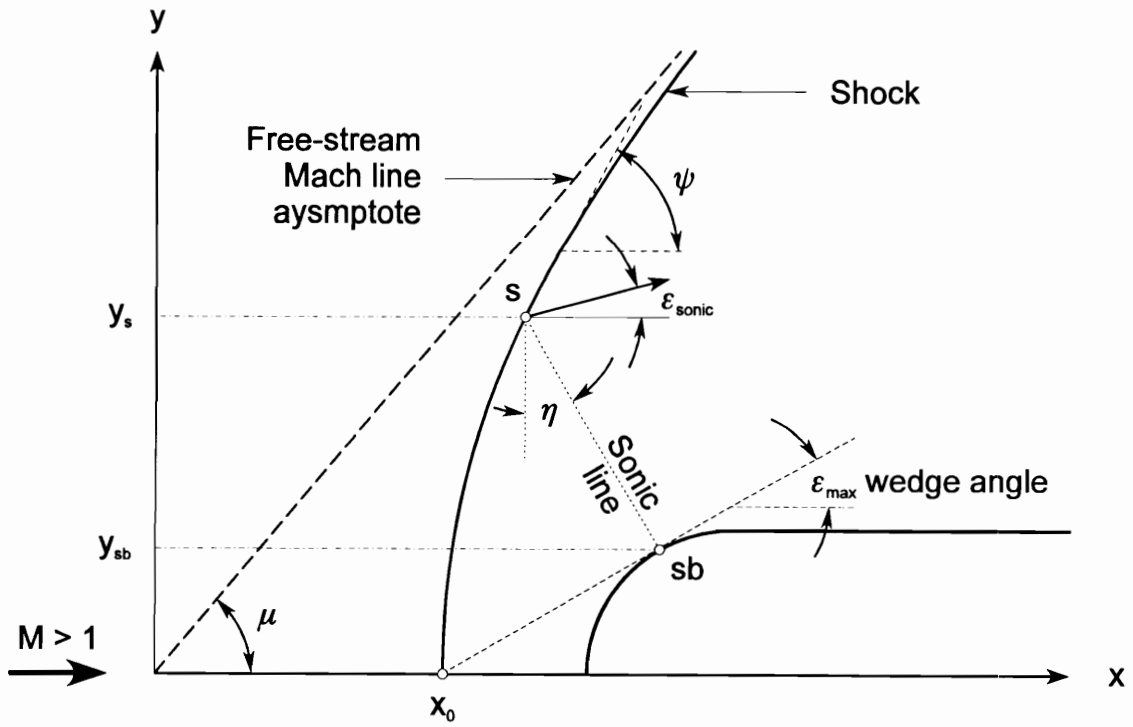

Figure 39. Moeckel (1949) model for detached shocks

wedge and asymptotically approaches the free-stream Mach lines. This hyperbola has the following form.

$$y = \frac{\sqrt{x^2 - x_0^2}}{\sqrt{M^2 - 1}} \tag{60}$$

To solve for the location of the shock vertex, x_0, Moeckel applied the continuity equation to the fluid that passes between the vertex and the sonic point, s, on the shock. Because the distribution of flow properties along the sonic line is unknown, the streamline representing the mass centroid of the flow was chosen as an appropriate "average" value. Because the total temperature is constant everywhere and the total pressure is constant along each streamline behind the shock, the continuity equation can be written as

$$\frac{A_1}{A_s} = \frac{(\rho_s V_s)_c}{\rho_1 V_1} = \left(\frac{P_{0s}}{P_{01}}\right)_c \left[\frac{(\rho V)_{cr}}{\rho_1 V_1}\right] = \left(\frac{P_{0s}}{P_{01}}\right)_c \frac{1}{\sigma} \tag{61}$$

where σ is the contraction ratio required to isentropically decelerate the free stream to sonic velocity. Using the coordinates of the sonic points on the shock and on the body, this can be written as

$$\frac{y_s - y_{sb}}{\cos\eta} = \left(\frac{P_{01}}{P_{0s}}\right)_c \sigma y_s \tag{62}$$

or

$$\frac{y_s}{y_{sb}} = \frac{1}{1 - \left(\frac{P_{01}}{P_{0s}}\right)_c \sigma \cos\eta} \tag{63}$$

The sonic line was assumed to be normal to the "average" flow direction in its vicinity. At the endpoints, the flow directions are ε_{sonic} and $\varepsilon_{\max}$. Because these values differ only slightly, the inclination of the sonic line was simply assumed to be $\eta = \varepsilon_s$.

The total pressure loss in Equation 63 is calculated from oblique shock theory by evaluating the shock slope at the mass centroid. For 2-dimensional flow, the upstream centroid is obviously located at $y_s/2$. Rewriting this in terms of Equation 60 yields

$$y_c = \frac{y_s}{2} = \frac{1}{2}\left(\frac{x_0 \cot\psi_s}{\left(M^2-1\right)\sqrt{\left(M^2-1\right)\cot^2\psi_s}}\right) \tag{64}$$

The slope of the shock wave at any point is given by

$$\frac{dy}{dx} = \tan\psi = \frac{\sqrt{x_0^2 + \left(M^2-1\right)y^2}}{\left(M^2-1\right)y} \tag{65}$$

If the above equation is evaluated at y_c, the x_0 terms cancel and leave the following expression for shock angle at the mass centroid in terms of the shock angle which produces sonic downstream flow.

$$\tan\psi_c = \frac{\sqrt{4\left(M^2-1\right)\tan^2\psi_s - 3}}{M^2-1} \tag{66}$$

A closed-form explicit relation for the shock angle which produces exactly sonic downstream flow is given by Wellmann (Wolf, 1993).

$$\sin^2\psi_s = \frac{1}{2\gamma}\left[\left(\frac{\gamma-3}{2M^2} + \frac{\gamma+1}{2}\right) + \sqrt{\frac{4\gamma}{M^4} + \left(\frac{\gamma-3}{2M^2} + \frac{\gamma+1}{2}\right)^2}\right] \tag{67}$$

The location of the shock vertex is then given by

$$\frac{x_0}{y_{sb}} = \sqrt{M^2 - 1}\left(\frac{y_s}{y_{sb}}\right)\sqrt{\left(M^2 - 1\right)\tan^2 \psi_s - 1} \tag{68}$$

The only term still to be calculated is the location of the sonic point on the body, y_{sb}. Moeckel suggested that this be approximated as the point where the body is inclined at the wedge angle corresponding to shock detachment, as shown in Figure 39, but noted that this method fails in the vicinity of sonic free-stream velocity. Busemann (1949) noted that the sonic line actually lies forward of this tangency point, but did not suggest a method for quantifying its location.

In the present investigation, the sonic point on the body was located at the tangency point for a wedge with half-angle *slightly greater* than the shock detachment angle. The Moeckel method outlined above was implemented with a range of angle increments, and the resulting shock detachment distances were compared with the measurements of Kim (1956). An increment of 1° over the wedge half-angle was found to give suitable agreement with these measurements over the range of Mach numbers presented, as shown in Figure 40. For a blade with a circular leading edge, this yields the following approximation for the sonic point on the body.

$$y_{sb} = \frac{LER}{\cos\left(\varepsilon_{\max} + 1°\right)} \tag{69}$$

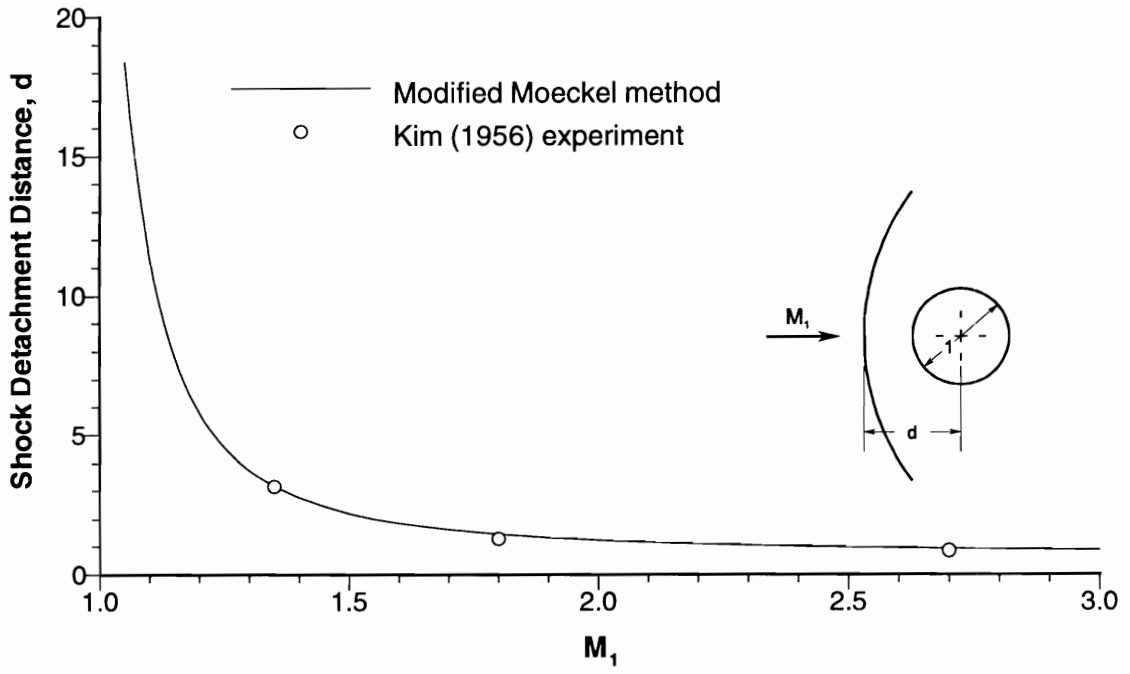

Figure 40. Shock detachment distance as a function of upstream Mach number

A closed-form explicit relation for the maximum shock wave angle which can occur before the shock detaches from the leading edge of a body is given by Wellmann (Wolf, 1993).

$$\cos 2\psi_{max} = \frac{1}{\gamma}\left[\left(\frac{\gamma+1}{2} - \cos 2\mu\right) - \sqrt{(\gamma+1)\left\{\left(\frac{\gamma+1}{2} - \cos 2\mu\right)^2 + \frac{\gamma}{4}(3-\gamma)\right\}}\right] \quad (70)$$

The wedge angle for shock detachment is then calculated from oblique shock theory using $\psi = \psi_{max}$.

$$\tan\varepsilon = 2\cot\psi\left[\frac{M_{1R}^2 \sin^2\psi - 1}{M_{1R}^2(\gamma + \cos 2\psi) + 2}\right] \quad (71)$$

The shape of the bow shock defined in this manner is uniquely defined by the upstream Mach number and the blade leading edge radius. Although this method clearly oversimplifies the known flow physics, the well-known trends are predicted correctly. Figure 41 shows that if Mach number is held fixed, the shock detachment distance and the extent of the strong shock region are both predicted to increase linearly with leading edge radius. Because the Mach number upstream of the body was constant, all of the shocks in this figure approach parallel asymptotes in the far-from-blade region. If the Mach number upstream of the body is increased, the shock detachment distance decreases and the shock asymptotes become more swept relative to the upstream flow. These trends are also predicted by the Moeckel method, as shown in Figure 42.

The slightly modified form of the Moeckel method discussed above is used to estimate the minimum bow shock detachment distance. Specifically, this is used to locate the point where the stagnation streamline intersects the bow shock for started operation

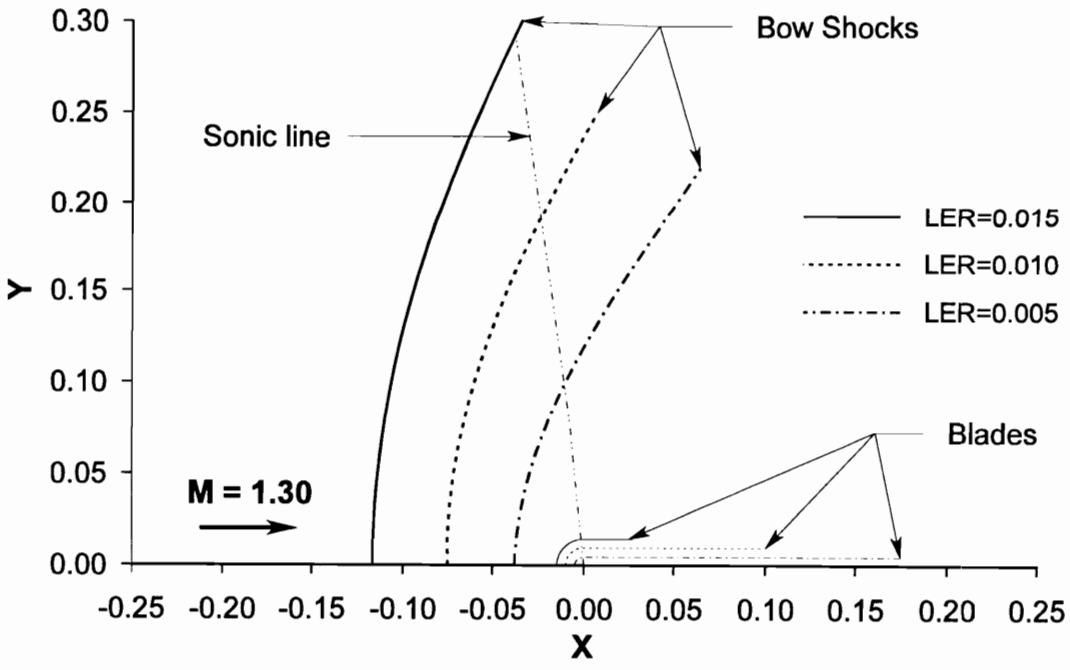

Figure 41. Effect of varying the leading edge radius on the shape of the bow shock predicted by the Moeckel method for $M = 1.30$

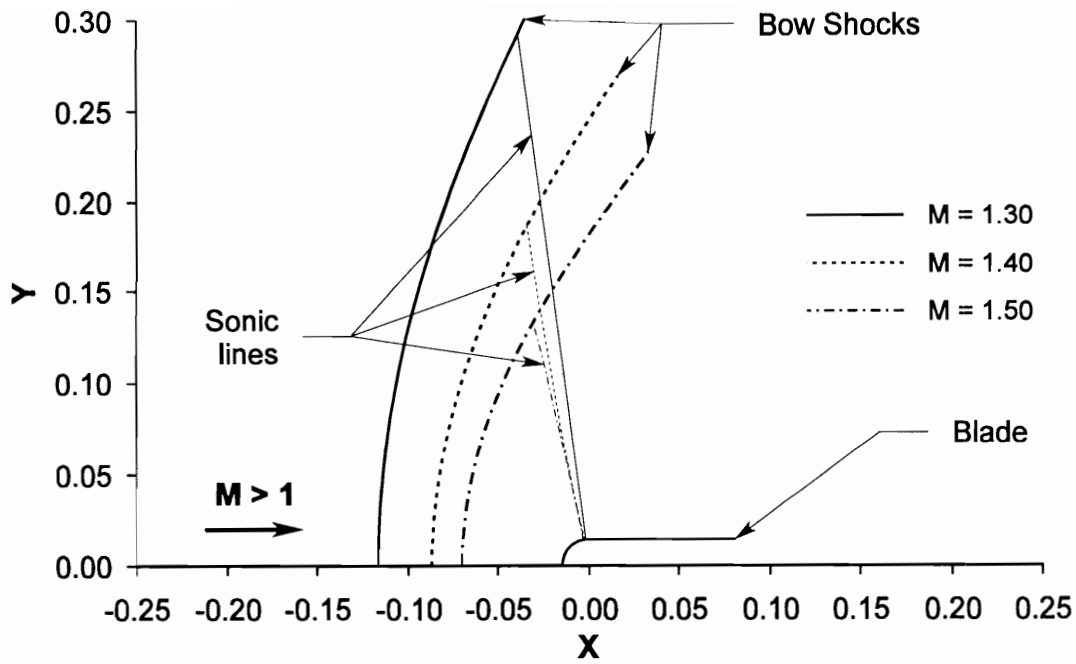

Figure 42. Effect of varying upstream Mach number on the shape of the bow shock predicted by the Moeckel method for *LER* = 0.015

(point B in Figure 43). The stagnation streamline *upstream* of the passage shock will generally follow the curvature of the suction surface, but there is no curvature of the stagnation streamline *downstream* of point B for started operation. To locate point B in physical space for a blade with a circular leading edge, a line of length

$$d = \frac{LER}{\sin(\varepsilon_{max} + 1^\circ)} \tag{72}$$

is extended upstream from the center of the leading edge circle at an angle β_A relative to the axial direction.

Because the Moeckel method was developed for isolated objects, it cannot account for the changes in shock structure which will occur with increased back pressure inside a turbomachine, and an alternate approach must be used for unstarted operation. As discussed in Chapter 3, the bow shock moves upstream and the stagnation streamline

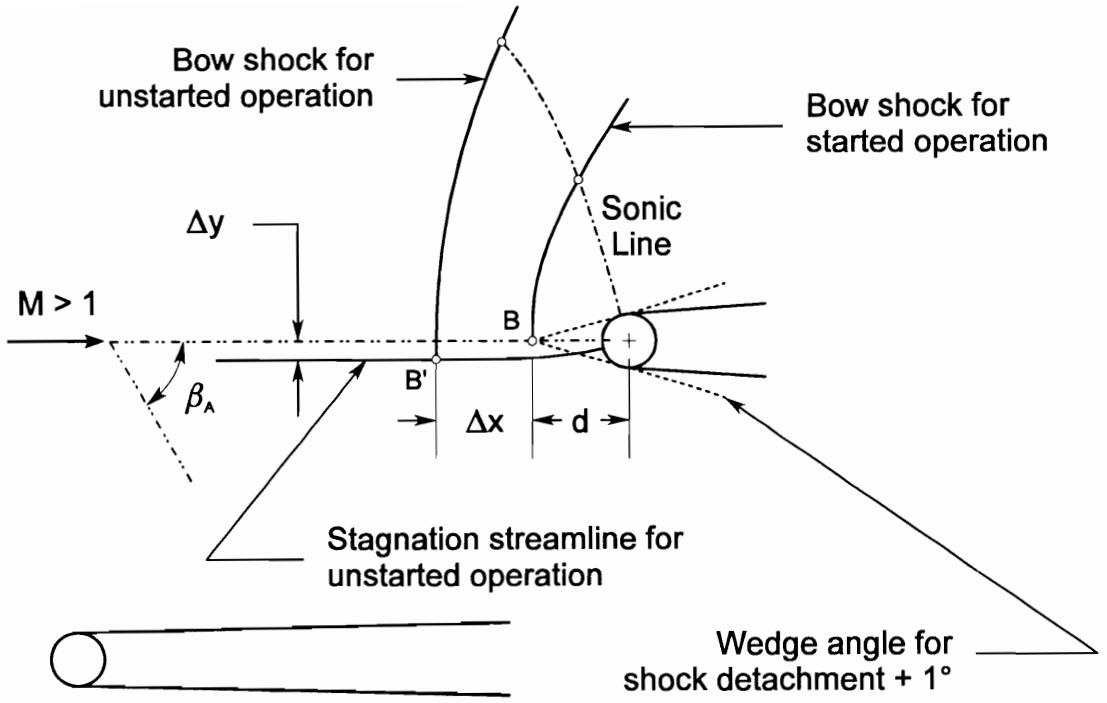

Figure 43. Approximation used to locate the endpoint of the detached bow wave for started and unstarted operation

shifts toward the suction surface as the incidence angle increases. Under these conditions, the stagnation streamline *is* curved downstream of the passage shock. Point B' is then located by extending a line of length $d + \Delta x$ upstream from the center of the leading edge circle at an angle β_A relative to the axial direction and translating normal to this line (toward the suction surface) by an amount Δy.

The relation between Δx and Δy for unstarted operation is not currently described by theory. To gain some understanding of this variation, the stagnation streamline was plotted from the unstarted CFD solutions generated for the L030-6 cascade with inlet Mach numbers of 1.100 and 1.200. This was accomplished by "releasing" a particle at the stagnation point on the blade leading edge and integrating its path ***upstream*** from that point. The variation of Δx and Δy was then scaled from these particle traces and is shown in Figure 44 for the L030-6 cascade with $M_1 = 1.200$. A

similar variation was observed for $M_1 = 1.100$, but with steeper slope, and it is anticipated that this relation will be slightly different for every blade shape and Mach number combination considered. As mentioned in Chapter 3, however, the effect of increasing Δx is much smaller than for increasing Δy and any reasonable variation will likely be within the accuracy of the method. For this reason, the following equation was used to relate the shock detachment distance and the stagnation streamline shift for unstarted operation.

$$\Delta x = 6\Delta y \tag{73}$$

To be clear, it is not suggested that the above relation is generally applicable to all blade profiles. It is suggested, however, that the shock detachment distance has a much smaller effect on the incidence calculation than does the stagnation streamline shift. Indeed, other investigators have neglected the detachment distance entirely (e.g., Starken,

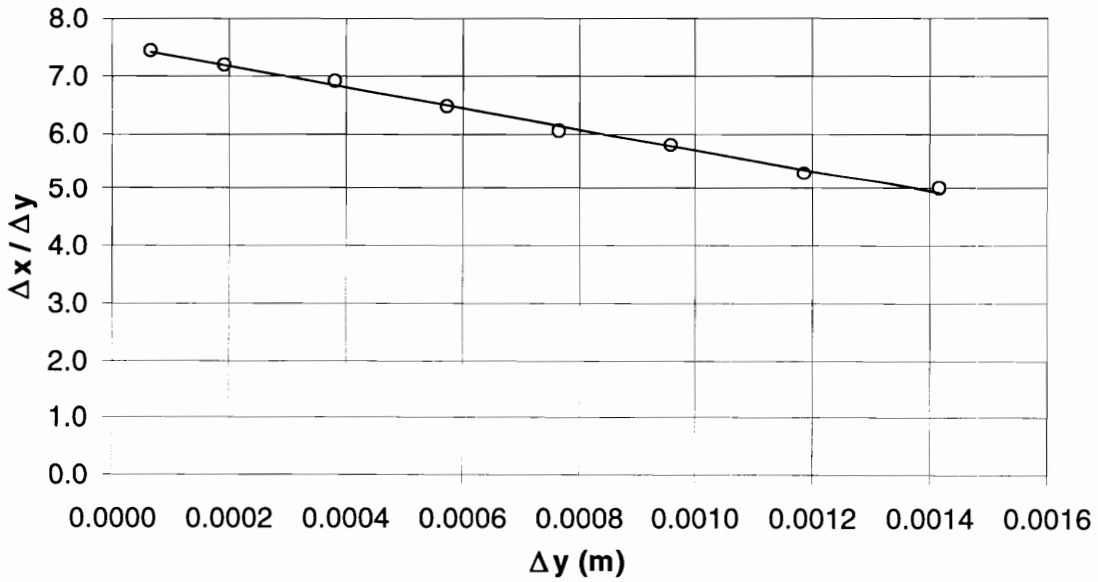

Figure 44. Relation between shock detachment and stagnation streamline shift for the L030-6 cascade with $M_1 = 1.200$ as determined from CFD

1971). Ultimately, however, it was decided to use the above relation as an approximate means to more fully include the effects of suction surface curvature on the length and position of the first captured Mach wave.

6.2 A Model for the Total Pressure Loss Due to the Bow Shock

A model for approximating the shape of the detached bow shock that stands ahead of a blunt object in a supersonic stream was presented in the previous section. Oblique shock theory will now be used to estimate the decrease in total pressure caused by the series of detached bow waves that will exist in front of an infinite cascade, as shown in Figure 45. The resulting total pressure will be used first in the evaluation of the continuity equation at the first captured Mach wave, and later in the calculation of the shock loss coefficient.

It is clear that the fluid entering a blade passage will cross an infinite number of bow waves from the adjacent blades, but the periodicity of the cascade can be used to simplify the calculation. The changes produced by crossing the bow wave originating ahead of the adjacent blade between points 1″ and 2‴ are identical to the changes

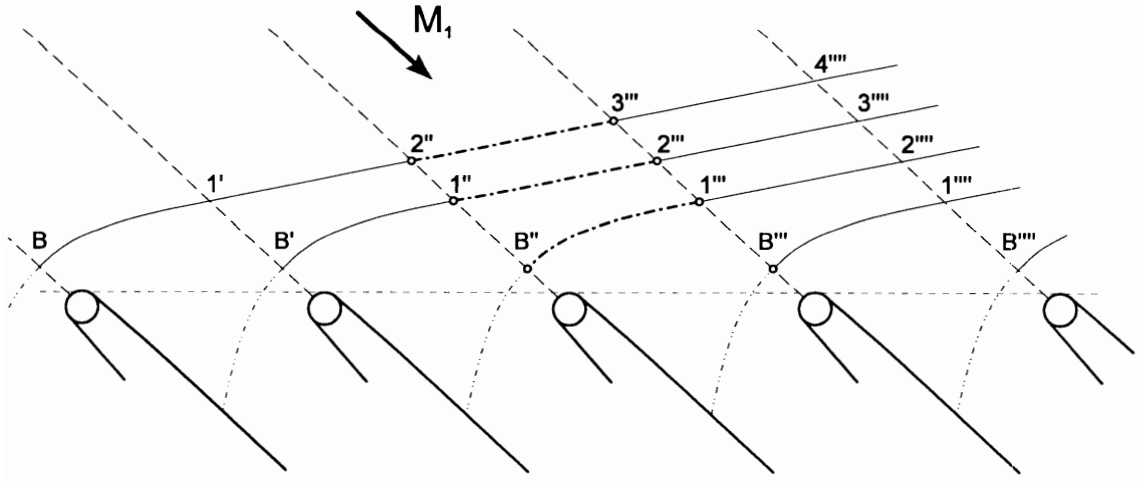

Figure 45. Wave pattern caused by blunt leading edges on an infinite cascade with subsonic axial velocity

produced by the bow wave from the current blade between points $1'''$ and $2''''$. This suggests that the loss produced by all of the upstream bow waves can be calculated by integrating the loss from a single wave between the stagnation streamline, point *B*, and infinity.

While each of the upstream waves will reduce the total pressure and Mach number by some amount, the strength of these waves decreases rapidly with distance ahead of the blade. This suggests that the Mach number changes produced by bow waves extending from the adjacent blades will be small. The curvature of the blade suction surface will also produce Mach number variations along the length of the bow wave, but entrance-region curvature is modest and these variations will be small. For the present analysis, the bow shock is treated as though it were in a uniform stream, and the total pressure drop across it is given by (Klapproth, 1950)

$$\frac{P_{0A}}{P_{01}} = 1 - \frac{\int_0^{\infty} \left(1 - \frac{P_{02}}{P_{01}}\right) dy}{\int_0^{s} dy} \tag{74}$$

where

$$\frac{P_{02}}{P_{01}} = \left[\frac{(\gamma+1)M_A^2 \sin^2\psi}{(\gamma-1)M_A^2 \sin^2\psi + 2}\right]^{\frac{\gamma}{\gamma-1}} \left[\frac{\gamma+1}{2\gamma M_A^2 \sin^2\psi - (\gamma-1)}\right]^{\frac{1}{\gamma-1}} \tag{75}$$

and ψ is obtained from Equation 65 (page 97).

Because the bow shock is upstream of the leading edge, the blade thickness does not appear in the denominator of Equation 74, which reduces to

$$\int_0^{s} dy = s\cos\beta_A \tag{76}$$

For started operation, the numerator in Equation 74 is obtained by numerical integration of the shock described by the modified Moeckel method presented in the previous sections. The spatial increment for integration was chosen as the arbitrarily small value

$$dy = \frac{y_s}{20} \tag{77}$$

and the upper bound of the integration was taken as the point where

$$\left(1 - \frac{P_{02}}{P_{01}}\right) dy < 10^{-10} \tag{78}$$

It is recognized that the above conditions are far more strict than the accuracy of the Moeckel method would suggest is appropriate. Although the method was programmed in double precision and the results computed to 14 decimal places, only the first 3 or perhaps 4 places are significant. The integration step could likely be more than 10 times larger and the loss criteria could clearly be several orders of magnitude larger with negligible change in predicted loss. The program generates a loss bucket with 40 operating points in less than 4 seconds, however, so there is little advantage to increasing these values.

For unstarted operation, the bow shock moves upstream from the blade leading edge and the strong shock region increases, as was shown in Figure 43 (page 102). The bow shock is pushed forward because there is subsonic flow everywhere behind the passage shock and the downstream pressure information can move upstream around the blade leading edge. Although this mechanism is understood in a broad sense, its effects are difficult to quantify and the shape of the unstarted bow shock can only be predicted with difficulty, even if a Navier-Stokes solver is employed.

Because more of the total flow passes through the strong portion of the bow wave during unstarted operation, it is reasonable to anticipate that the loss produced by the bow shock will increase with incidence angle. An approximation of this increased loss has been included in the present research by using an increased "effective leading edge radius" to calculate the bow shock loss for unstarted operation. (The physical coordinates of the blade clearly remain the same, and this increased "effective" leading edge radius is used only in the bow wave loss calculation.)

In the Moeckel method, the blade leading edge radius is used to calculate the height difference between the stagnation streamline and the sonic point on the blade surface. Because this height difference increases by the amount of the stagnation streamline shift during unstarted operation, it is the present author's opinion that the effective leading edge radius used in the bow shock calculation should be proportional to Δy. Examination of the CFD solutions indicated that the sonic line becomes curved after the shock detaches, as represented in Figure 43 (page 102), suggesting that the effective leading edge radius should increase by somewhat less than Δy.

Recognizing this as an empirical input, the effective leading edge radius used in the bow shock calculation was adjusted to provide satisfactory agreement with the shock loss extracted from CFD for a single operating point. The comparison was made for the L030-6 cascade with $M_1 = 1.200$ and $\beta_1 = 64.83°$ (near stall), and resulted in the following approximation.

$$LER_{\substack{bow \\ shock \\ loss}} = LER_{blade} + \frac{\Delta y}{2} \tag{79}$$

This relation provided the effective leading edge radius used to calculate the bow shock loss for all operating conditions. Clearly, this reduces to the actual blade leading

edge radius for started operation, where $\Delta y = 0$. The Moeckel method was used to approximate the shape of the detached bow shock using the Mach number along the first captured Mach wave, M_A, and this "effective leading edge radius." The total pressure loss caused by this wave was then calculated from Equation 74 (page 105).

Before leaving this subject, an important point must be made. While a number of simplifying assumptions have been introduced in the present analysis, Equation 79 represents the only strictly empirical input. The remainder of the present method is obtained by using fundamental fluid mechanics to analyze the known flow physics.

6.3 A Model for Passage Shock Performance

The approximations used for the shape of the passage shock (or shocks) over the entire range of cascade operation are presented in this section, as are the methods used to quantify shock system performance. The started conditions are discussed first, in order of decreasing back pressure. Considering a typical loss bucket, this approach starts at the minimum overall loss point (corresponding to $P_2 = P_{2opt}$) and then moves vertically up the choked portion of the characteristic. This will be followed by a discussion of unstarted operation in order of increasing incidence.

Recall that for started operation, there is supersonic flow downstream of the weak passage shock and that this region of supersonic flow is followed by a nearly normal shock. As the back pressure is increased, the size of this supersonic region decreases until there is purely subsonic flow behind the passage shock. This condition occurs at the point when the cascade unstarts.

Figure 46 shows the approximations used for the passage shock at the cascade start/unstart point. The Moeckel hyperbola is used to represent the curved portion of the passage shock between the vertex, *B*, and the point where the downstream flow is exactly

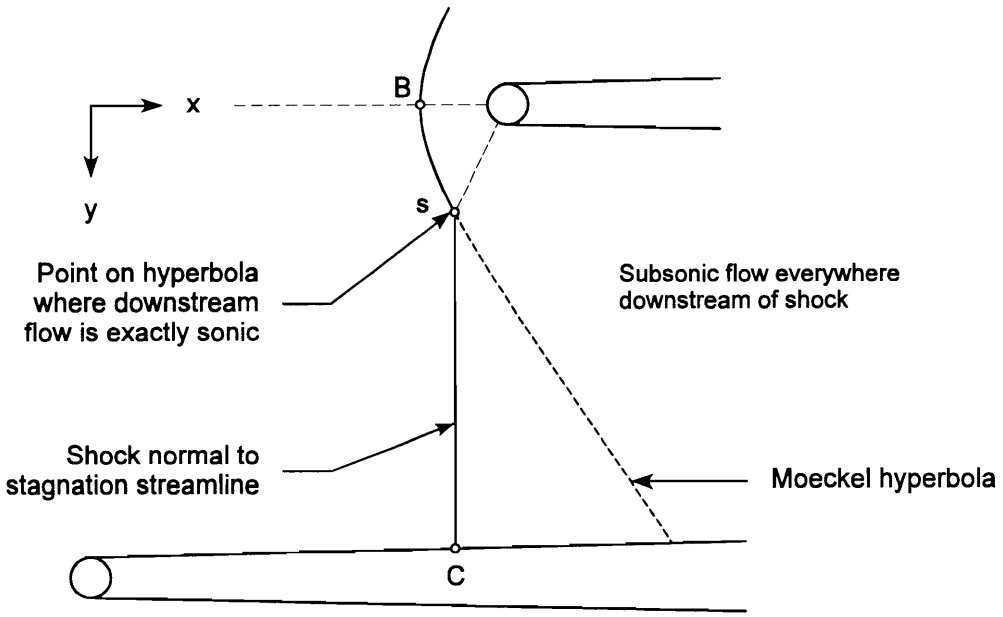

Figure 46. Approximation of passage shock at cascade start/unstart point ($P_2 = P_{2opt}$)

sonic, *s*. From the sonic point to the blade suction surface, the passage shock is approximated by a straight line normal to the stagnation streamline at point *B*.

The decrease in total pressure caused by this shock is mass averaged as follows.

$$\frac{\overline{P}_{02}}{P_{0A}} = \frac{\int_B^C \rho V_x \frac{P_{02}}{P_{0A}} dy}{\int_B^C \rho V_x dy} \tag{80}$$

where P_{02}/P_{0A} is obtained from oblique shock theory (Equation 75, page 105). The numerator in the above equation is numerically integrated using 200 points across the passage. The integration steps are determined by equally dividing the axial distance between the blade suction surface coordinate at the first captured Mach wave and at the passage shock intersection point. At each point along the blade surface, the Mach number is calculated as a Prandtl-Meyer expansion from the upstream condition and the

Mach line is extended to the passage shock. The number of points used in this integration is clearly not justified on the basis of the assumed accuracy of the method, but was chosen to allow accurate physical-space location of the shock transition point, *s*. To simplify the evaluation of the shock surface angle in Equation 75, this integration is performed in a coordinate system aligned with the stagnation streamline at point *B* (the Moeckel coordinates shown in Figure 39, page 95).

Because the blade suction surface is not completely flat, in general, there will be some variation in Mach number and flow angle upstream of the passage shock between points *B* and *C*. The Mach number variations are included directly in the evaluation of Equation 75 at each point along the shock. The relative flow angle variations appear in the calculation of the shock angle used in Equation 75. For points along the hyperbola, the shock angle is given by

$$\psi = \tan^{-1}\left(\frac{\sqrt{x_0^2 + \left(M^2 - 1\right)y^2}}{\left(M^2 - 1\right)y}\right) + \beta - \beta_A \tag{81}$$

where β is the flow angle upstream of the current point on the shock. For points along the straight section, the shock angle is given by

$$\psi = 90° + \beta - \beta_A \tag{82}$$

The denominator in the Equation 80 is known from the conditions along the first captured Mach wave.

$$\int_B^C \rho V_x dy = \frac{F\left(M_A\right) P_{0A} \left|\overline{AB}\right| \sin \mu_A}{\sqrt{c_p T_{0A}}} \tag{83}$$

The mass-averaged shock loss coefficient is then given by

$$\omega_{shock} = \frac{1 - \frac{\overline{P}_{02}}{P_{0A}} \frac{P_{0A}}{P_{01}}}{1 - \frac{P_1}{P_{01}}} \tag{84}$$

As the back pressure is reduced below P_{2opt} (into the "medium back pressure" regime), the normal portion of the shock moves downstream and there is supersonic flow behind the weak shock. This is modeled by shifting the shock transition point farther along the Moeckel hyperbola toward the suction surface, as shown in Figure 47. The supersonic flow region behind the weak shock is bounded on the downstream end by a nearly normal shock. This is modeled as an exactly normal shock with an upstream Mach number equal to the Mach number that exists downstream of the weak shock at the assumed transition point, *T*.

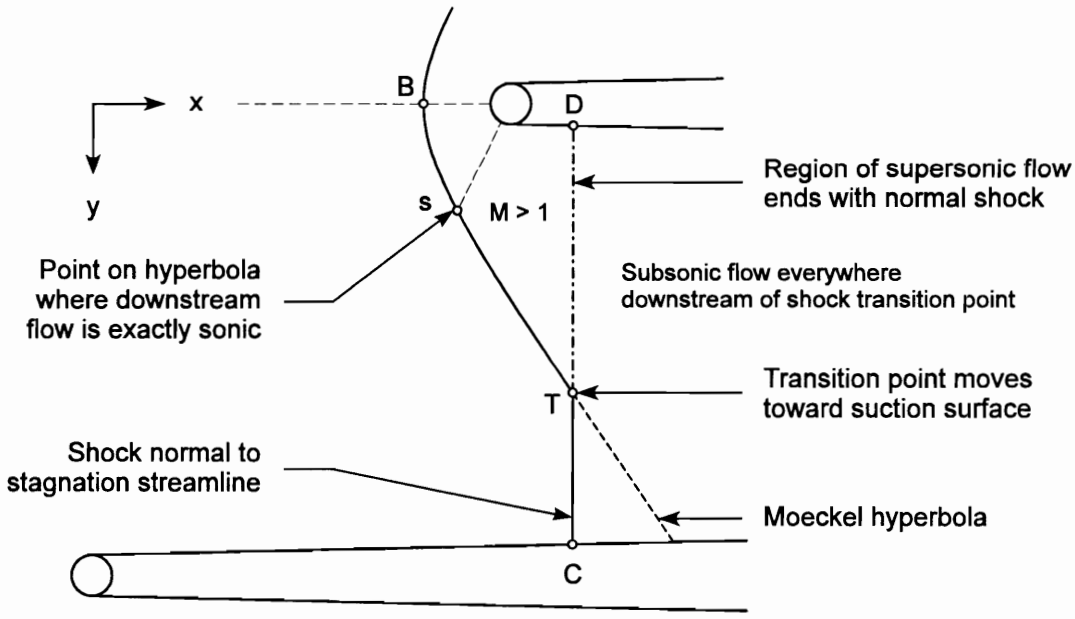

Figure 47. Approximation of passage shock system for "medium back pressure" operation

For the "medium back pressure" flow regime, Equation 80 is used to calculate the total pressure loss along the path *B-T-C*. The loss from the normal shock between points *D* and *T* is then included in the overall total pressure ratio.

$$\frac{\overline{P}_{03}}{\overline{P}_{02}} = \frac{\dot{m}_{BT}\dfrac{P_{03}}{\overline{P}_{02}} + \dot{m}_{TC}(1)}{\int_{B}^{C} \rho V_x dy} \tag{85}$$

where $\dot{m}_{BT}$ is the mass flow passing through the normal shock between points *D* and *T* and $\dot{m}_{TC}$ is the mass flow not passing through this shock. The total pressure ratio in the numerator of this equation is the standard normal shock relation.

$$\frac{P_{03}}{\overline{P}_{02}} = \left[\frac{(\gamma+1)M^2}{(\gamma-1)M^2+2}\right]^{\frac{\gamma}{\gamma-1}}\left[\frac{\gamma+1}{2\gamma M^2-(\gamma-1)}\right]^{\frac{1}{\gamma-1}} \tag{86}$$

The mass-averaged shock loss coefficient is then given by

$$\omega_{shock} = \frac{1-\dfrac{\overline{P}_{03}}{\overline{P}_{02}}\dfrac{\overline{P}_{02}}{P_{0A}}\dfrac{P_{0A}}{P_{01}}}{1-\dfrac{P_1}{P_{01}}} \tag{87}$$

If the back pressure is reduced even further, into the "low back pressure" regime, 2 distinct passage shocks will exist. The weak shock extends across the entire blade passage, although it may transform into a Mach reflection to satisfy the continuity requirement near the suction surface. The size of a Mach reflection is typically small, however, and this possibility is ignored in the present method. The weak passage shock is approximated by extending the Moeckel hyperbola all the way to the suction surface, as shown in Figure 48.

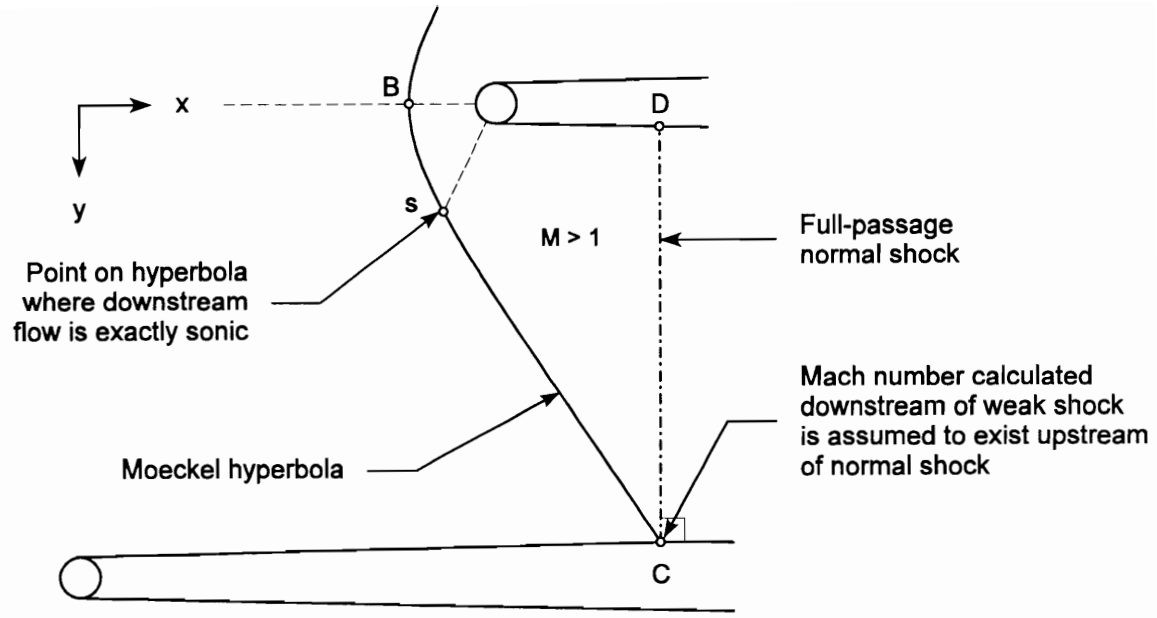

Figure 48. Approximation of passage shock system at boundary between "low back pressure" and "medium back pressure" regimes

Just as in the "medium back pressure" regime, the supersonic flow region behind the weak shock is bounded on the downstream end by a nearly normal shock. In the "low back pressure" regime, however, the normal shock extends across the entire blade passage. As before, this is modeled as an exactly normal shock. For the operating condition shown in Figure 48, the Mach number upstream of the normal shock is approximated as the Mach number that exists downstream of the weak shock at the suction surface intersection point, *C*.

As the back pressure is reduced further, the second passage shock moves downstream and the Mach number ahead of this shock increases. Estimation of this Mach number is not straightforward, however, because transonic flows are extremely sensitive to even modest changes in boundary conditions. The suction surface boundary layer thickens near the first passage shock impingement point, *C*, reducing the available flow area for the free-stream fluid. In the case of a Mach reflection, which has subsonic

flow downstream, this mechanism provides the area contraction required to reaccelerate the flow to supersonic. Depending on the strength of the first passage shock, the suction surface boundary layer may separate and, if it does, it may or may not reattach downstream. Prediction of this shock-boundary layer interaction is beyond the scope of the present research (and beyond the current state-of-the-art).

Although the increase in upstream Mach number that occurs as the second passage shock moves downstream cannot be predicted exactly, a rough approximation for the trend is included in the present method. This approach allows the Mach number ahead of the second passage shock to increase continuously from the value downstream of point *C* in Figure 48, thereby avoiding any discontinuity of the predicted loss coefficients between the "medium" and "low" back pressure regimes. Before the Mach number downstream of point *C* can be estimated, however, the flow angle at point *C* must be approximated.

Continuity requires that the flow near the blade be aligned with the blade surface. The potentially large suction surface boundary layer downstream of the weak shock, however, can produce a substantial variation between the free-stream flow angle and the blade surface angle. Because these boundary layer-induced variations cannot currently be predicted, the pressure-surface blade angle was chosen as a more suitable "average" flow angle upstream of the second passage shock. A line is extended normal to the suction surface, as shown in Figure 48, and the pressure surface blade angle at point *D* is chosen as the "representative" flow angle along line *CD*.

It is recognized that this method will generally over-predict the flow angle at point *C* by a modest amount, and that some combination of the pressure- and suction-surface blade angles might make a more appropriate average here. Near the blade trailing edge, however, the suction surface curvature is more pronounced and suction surface boundary

layer separations are more likely. It is in this region that the pressure surface blade angle is likely to be more representative of the "average" flow angle.

Both the flow angle and Mach number at point *C* have been specified in this approach, which leads to a violation of the continuity equation. To resolve this, a fictitious "effective" blade height is calculated to satisfy continuity. Recalling that line *CD* is normal to the blade suction surface, this effective blade height is obtained be rearranging the continuity equation.

$$\frac{h_{effective}}{h_{actual}} = \frac{\dot{m}\sqrt{c_p T_{02C}}}{F(M_{2C})P_{02C}\left|\overline{CD}\right|\cos\left(\beta_{ps,D} - \beta_{ss,C}\right)} \tag{88}$$

where P_{02C} is the total pressure downstream of the weak shock at point C (recall that total temperature is constant for a stationary cascade).

The flow conditions at point *C* are now completely specified, and the calculations for the remainder of the "low back pressure" regime can be made. As shown in Figure 49, the second passage shock moves downstream to point *E* and a line is extended normal to the suction surface. The "representative" flow angle along this line is assumed to be the pressure surface blade angle at point *F*. The Mach number ahead of the second passage shock for this condition is obtained by calculating an isentropic expansion from point *C* and using the effective blade height to solve the continuity equation.

$$F(M_E) = \frac{\dot{m}\sqrt{c_p T_{02C}}}{P_{02C}\dfrac{h_{effective}}{h_{actual}}\left|\overline{EF}\right|\cos\left(\beta_{ps,F} - \beta_{ss,E}\right)} \tag{89}$$

The approach outlined above is clearly not a rigorous treatment of the flow conditions in the "low back pressure" regime. These flow conditions defy simple analysis because the viscous effects cannot be ignored. Although the present method provides a

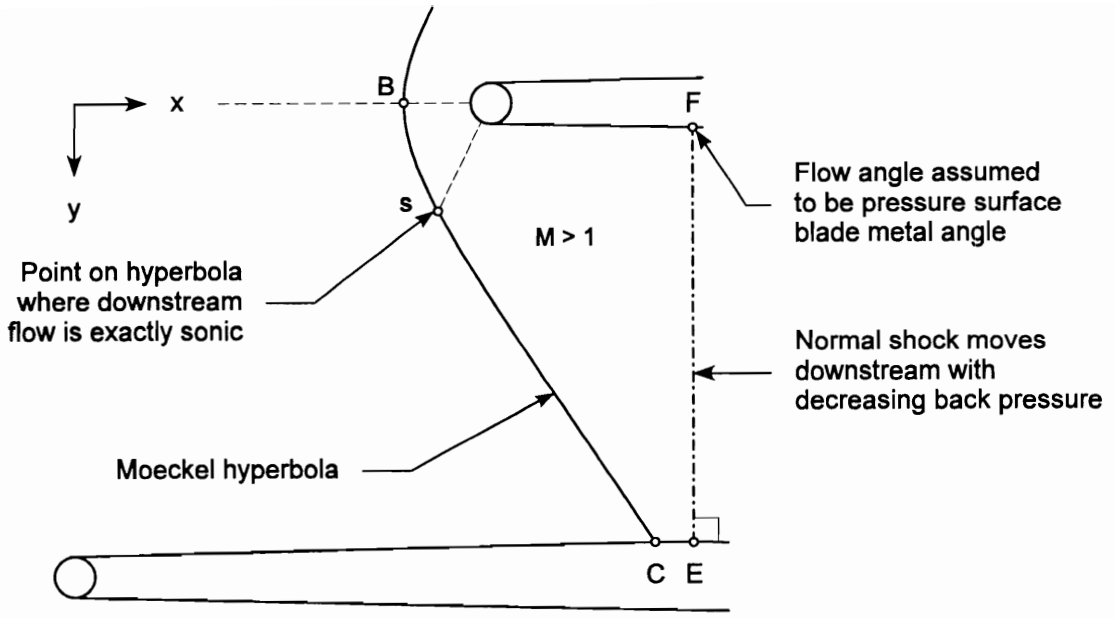

Figure 49. Approximation of passage shock system for "low back pressure" operation

very crude approximation for this flow regime, it does predict the correct trend of increasing upstream Mach number as the second passage shock moves downstream to the blade trailing edge. As shown in Chapter 3, further reduction in exit pressure causes a dove-tail shock to stand at the trailing edge and this shock transforms into a normal shock near the pressure surface. Operation with a dove-tail shock is not considered in the present analysis because it corresponds to extremely undesirable rotor operating conditions which are of little value to the turbine engine community.

For the "low back pressure" flow regime, Equation 80 (page 109) is used to calculate the total pressure loss from the weak shock along the path *B*-*C*. The loss from the second passage shock, which extends across the entire passage between points *E* and *F*, is then calculated from the standard normal shock relation (Equation 86, page 112). Finally, Equation 87 is used to obtain the shock loss coefficient, ω_{shock}.

Attention is now focused on the shape of the passage shock for unstarted operation. At the cascade start/unstart point, the passage shock is approximated as curved between the vertex and the sonic point, and as a straight line between the sonic point and the blade suction surface. This was discussed at the beginning of this section, and is shown again in Figure 50.

As the incidence angle increases, the shock detachment distance increases by an amount Δx and the stagnation streamline shifts by an amount Δy. The vertex of the Moeckel hyperbola is assumed to follow these translations from point B to point B' so that it is always located where the stagnation streamline intersects the bow/passage shock. The curved portion of the shock is reduced by moving the shock transition point forward of the new sonic point, s', by an amount Δx. When the shock transition point reaches the vertex of the hyperbola, the entire shock is approximated as a straight line normal to

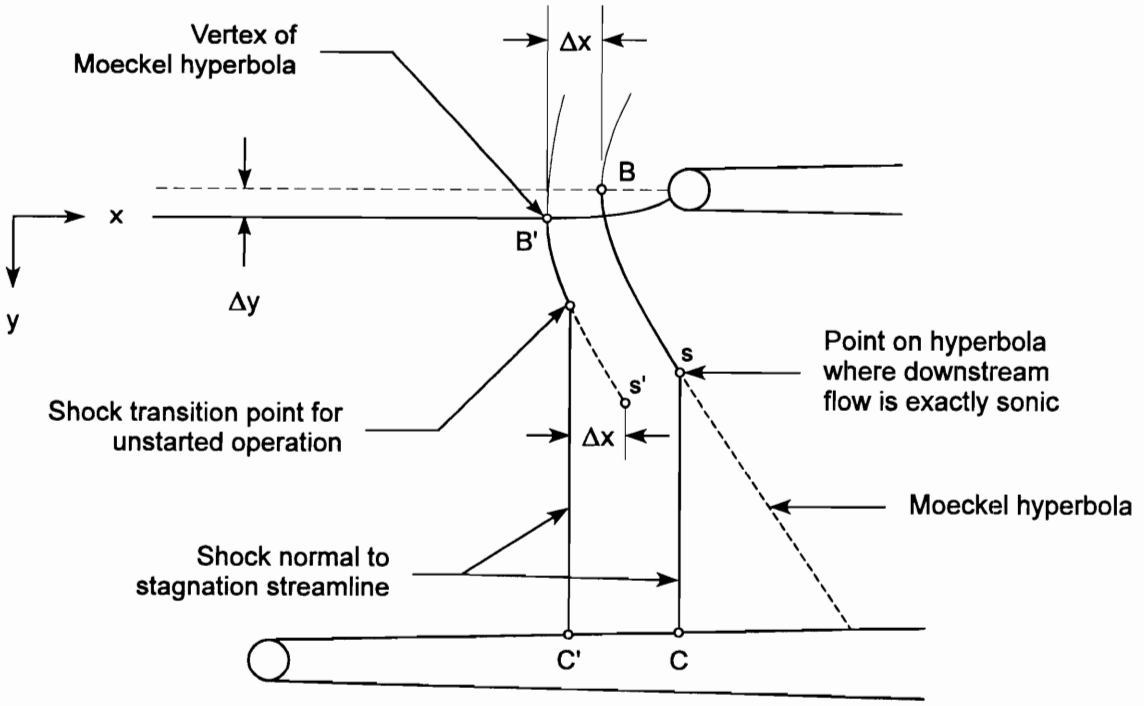

Figure 50. Assumed shape of passage shock for unstarted operation

the stagnation streamline at point B'. The total pressure ratio across the passage shock for unstarted operation is given by Equation 80 (page 109), and the shock loss coefficient is given by Equation 84 (page 111).

6.4 Inputs Required for Implementation

In the previous sections, detailed models were presented for the various mechanisms which govern supersonic 2-dimensional cascade flow. This section identifies the few user inputs required by the computer program that implements this prediction method.

Blade geometry is specified by an arbitrary number of (x, y) coordinates along the pressure and suction surfaces, by the leading edge radius, and by the blade spacing. Surface coordinates along the leading edge are described by the equation for a circle, and splines are fit to the surface coordinates downstream of the leading edge. The cascade stagger angle is used to provide initial guesses for some of the root finders, but it has no effect on the final solution.

The only aerodynamic input that is *required* is the inlet Mach number, M_1. Values are input for inlet total pressure and total temperature, but these have no effect on the predicted shock loss coefficients. If the blade coordinates and inlet properties are specified in SI units, however, prediction of static properties upstream of the passage shock and of the mass flow will be obtained.

7. Results and Discussion

In this chapter, the shock loss predictions obtained from the present method are compared with the available validation tools. To ensure that the cascade start/unstart point is predicted correctly, minimum-incidence angle comparisons are made first. This will be followed by a discussion of shock losses during unstarted operation and started operation, in that order. The results of the present analysis are presented first, followed by a discussion of the significance of the results and the limitations of the present method. The chapter is concluded with a demonstration that the present method can be used as the basis of an overall loss prediction method.

7.1 Minimum Inlet Flow Angle

A comparison of the minimum inlet flow angles for the L030-4 and L030-6 cascades is shown as a function of inlet Mach number in Figure 51. The lines in this figure were obtained from the present analysis, the experimental values were reported by Schreiber (1980, 1981), and the CFD values were obtained from the RVCQ3D code. The largest difference between the present predictions and the measured values is 0.15°, while the largest difference between the present predictions and the values obtained from CFD is 0.31°. Since the facility inlet flow angle measurement uncertainty is 0.5° for 95% confidence (Schreiber and Tweedt, 1987), this can be considered quite good agreement.

Accurate prediction of cascade mass flow is one of the fundamental requirements of any performance prediction system. This is especially critical for the analysis of supersonic flows where the mass flow can be limited by choking of the blade row. The vertical portion of a transonic fan or compressor characteristic simply cannot be predicted without first determining the choke-limited mass flow. The common use of a parabola to correlate loss with incidence (e.g., Çetin, et al., 1987) does not consider the cascade

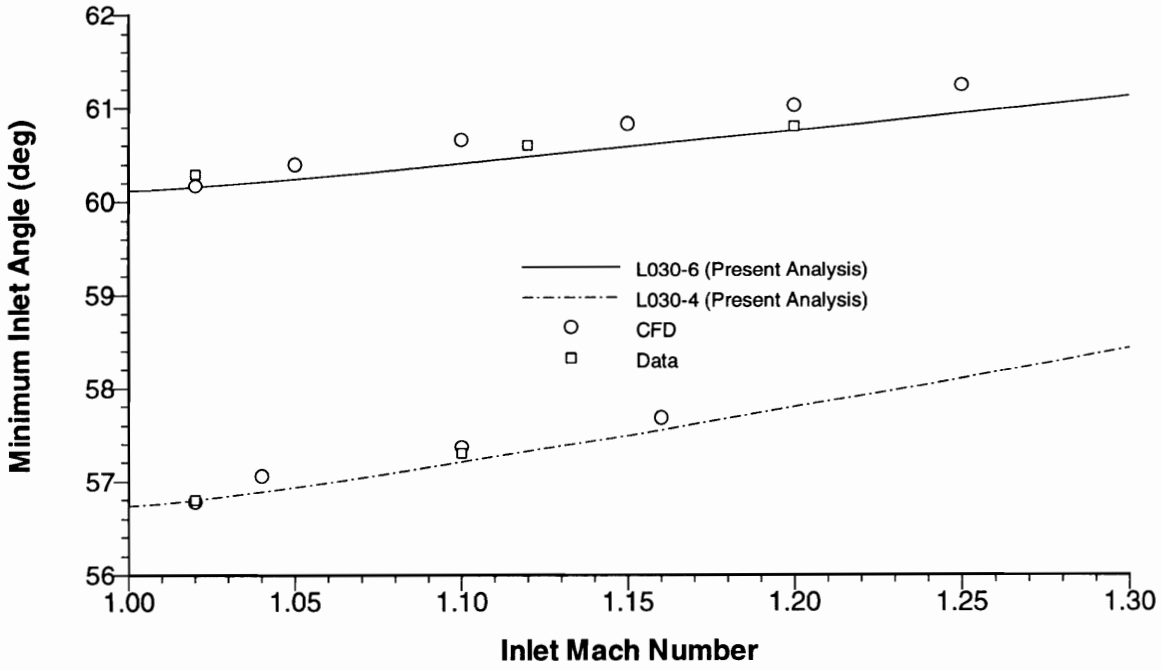

***Figure 51.* Predicted minimum inlet flow angle as a function of Mach number for L030-4 and L030-6 cascades**

choke point, making the approach poorly suited to supersonic cascade analysis. The present physics-based method clearly provides an accurate estimation of the choking value of inlet flow angle. While this is not an original contribution, it is an essential feature of a transonic loss prediction technique.

7.2 Unstarted Cascade Results

The total pressure loss coefficients for unstarted operation of the L030-6 cascade with an inlet Mach number of 1.20 are shown in Figure 52. As stated in the Chapter 5, the CFD solutions were obtained with no sidewall variation ($AVDR \equiv 1$). The points labeled "Fit to Data" were obtained by evaluating the dashed curves labeled ω_{shock} fit by Schreiber (1987) to the data in Figure 26 (page 69). Although comparisons during started

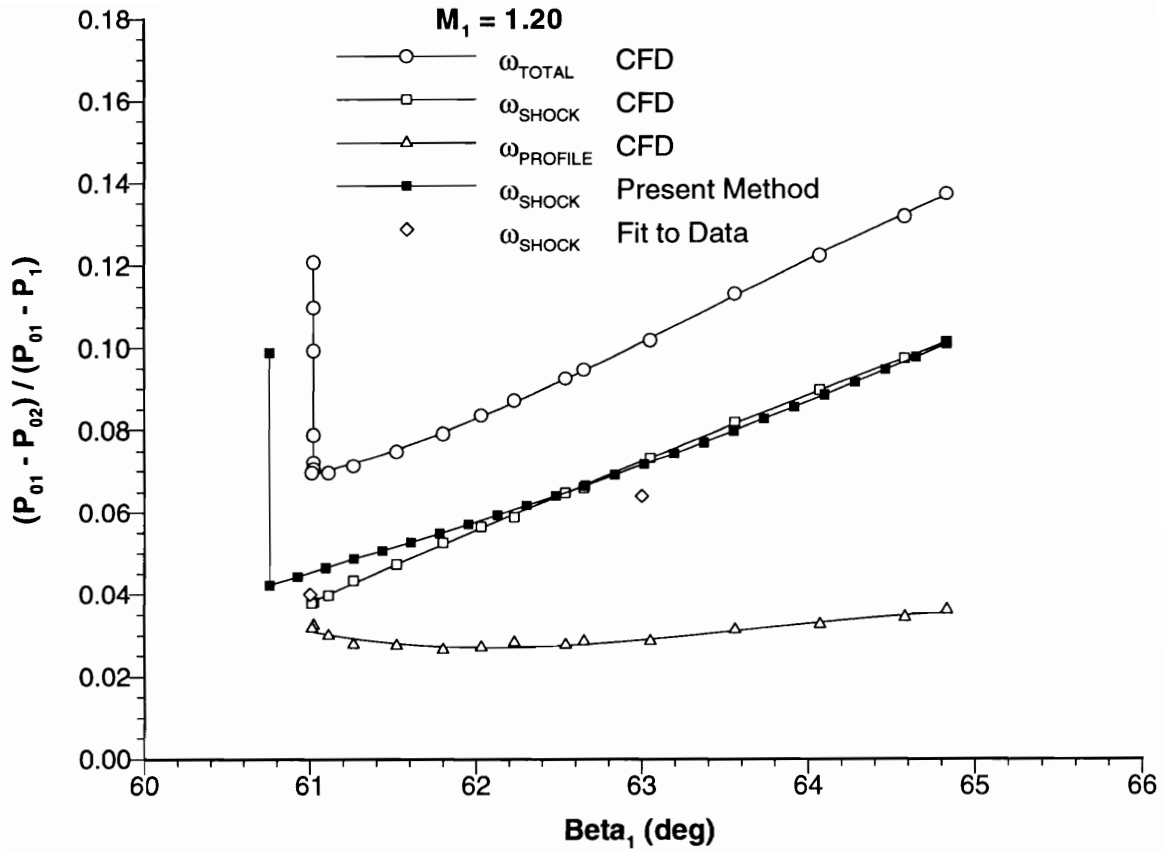

Figure 52. Loss coefficient comparison for unstarted operation of the L030-6 cascade with M_1 = 1.20

operation are deferred until a later section, the minimum-incidence condition predicted both by the CFD and by the present method are identified.

The most significant point made by this figure is the dramatic increase in shock loss as the inlet flow angle increases. This is shown clearly by the data, by the CFD solutions, and by the model predictions. The viscous profile loss predicted by the CFD is seen to be nearly constant over the entire unstarted operating range, with a variation of less than 0.01 between the minimum and maximum unstarted loss coefficients. The actual viscous loss is likely to be slightly larger near stall than indicated by the CFD solutions, which show a suction surface boundary layer separation downstream of the

passage shock. It is the author's opinion, however, that the actual variation of viscous loss between stall and choke will still be significantly smaller than the variation of shock loss over the same operating range.

The maximum difference between the shock loss coefficients predicted by the present method and by the CFD was 0.006 for this Mach number and occurred at $\beta_1 = 61.0°$ (the cascade start/unstart point predicted by the CFD). There was negligible difference between these predictions at the stall point, but this is to be expected since this was the single operating condition used to assign the empirical constant in the bow shock model. The maximum difference between the present predictions and the measured data was 0.007 and occurred at $\beta_1 = 63.0°$.

To understand the significance of the level of accuracy demonstrated in this figure, it is helpful to consider the recent ASME turbomachinery CFD "blind" test case (Strazisar and Denton, 1995). As part of this study, turbomachinery designers at several industrial concerns were asked what level of accuracy they would like to see from a CFD simulation before feeling confident about using it to guide a new design. Among other things, accuracy of ±1-2% in pressure rise and of ±1% in efficiency were desired. To obtain these values for NASA Rotor 37, the subject of that investigation, the predicted total pressure loss coefficient must be accurate within 0.01 (Dunham, 1995). The accuracy of the loss coefficient required to obtain the desired accuracy in pressure rise and efficiency will obviously depend on the configuration considered, but this gives an indication of the level of accuracy which is typically needed. Although the viscous loss has not been addressed in the present research, the accuracy of the predicted shock loss coefficients in Figure 52 clearly falls within the desired range.

The total pressure loss coefficients for unstarted operation of the L030-6 cascade with inlet Mach number of 1.15 are shown in Figure 53. The dramatic increase in shock

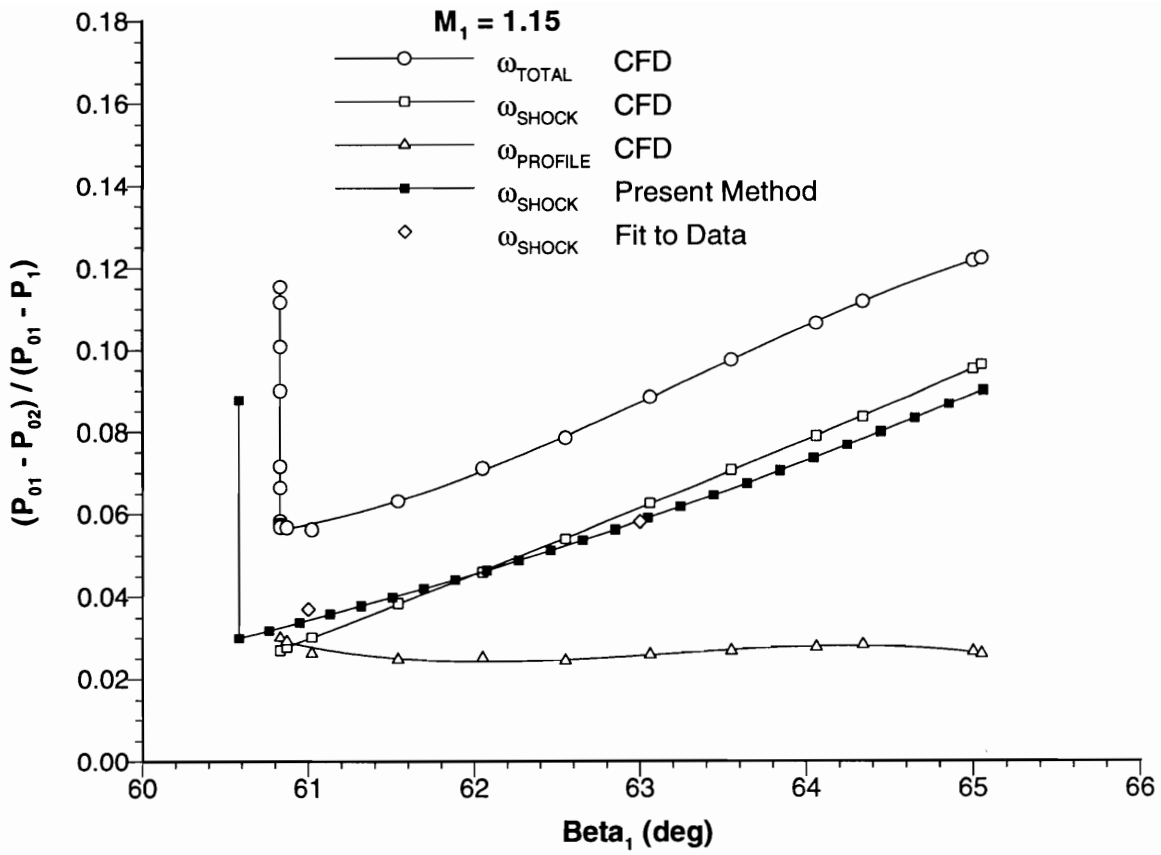

Figure 53. Loss coefficient comparison for unstarted operation of the L030-6 cascade with M_1 = 1.15

loss with increasing incidence is clear, while the viscous profile loss is again nearly constant (0.006 difference between minimum and maximum). The maximum difference between the shock loss coefficients predicted by the present method and by the CFD was 0.006 for this Mach number as well, but it occurred at the near-stall point ($\beta_1 = 65.0°$).

Figure 54 shows the total pressure loss coefficients for unstarted operation of the L030-6 cascade with an inlet Mach number of 1.10. As before, there is a significant increase in shock loss with incidence and the viscous profile loss is nearly constant (0.007 difference between maximum and minimum). The agreement between the present predictions and the CFD is better for this case, with a maximum difference of 0.004 at the

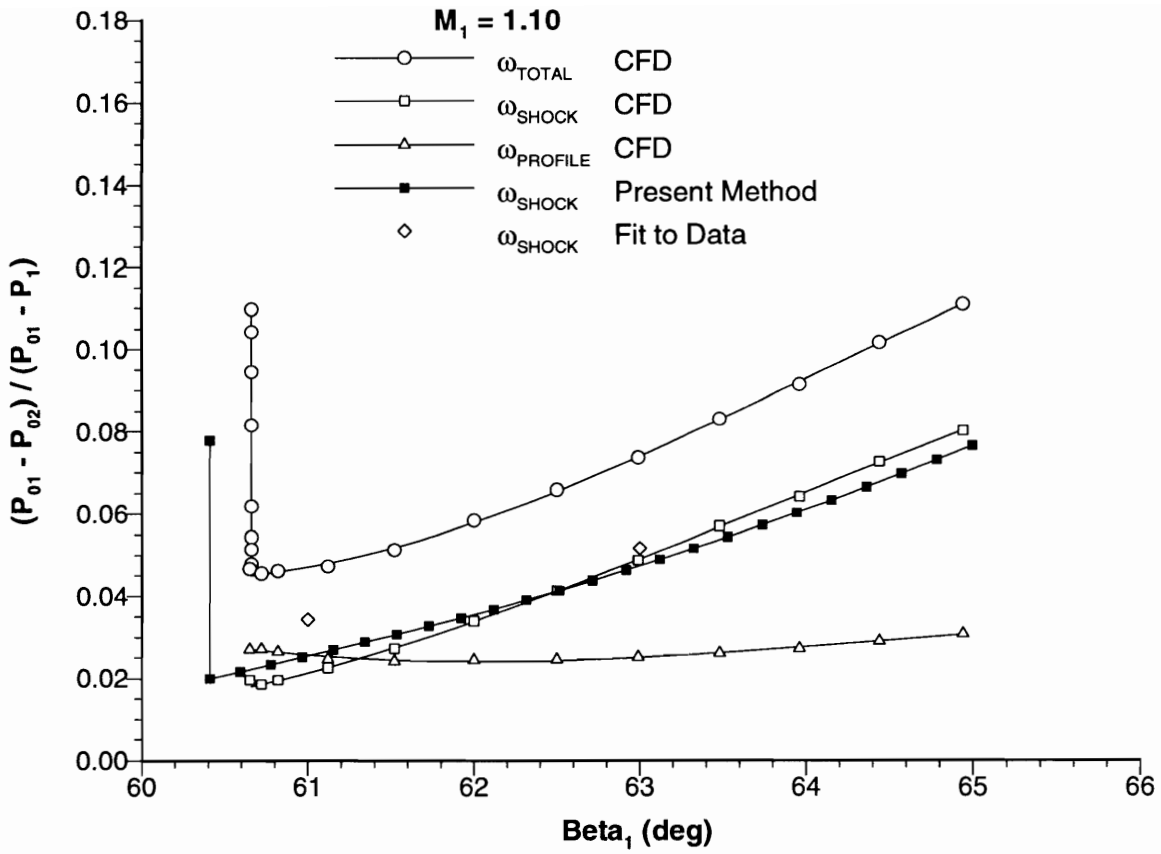

Figure 54. Loss coefficient comparison for unstarted operation of the L030-6 cascade with $M_1 = 1.10$

near-stall point, but the discrepancy with the measured data increased to 0.009 at $\beta_1 = 61.0°$.

To illustrate another trend shown in the 3 previous figures, the shock loss and viscous profile loss coefficients obtained from CFD for the L030-6 cascade are plotted in Figure 55. The shock loss is clearly much more sensitive to Mach number than is the profile loss. For the Mach number range considered, the increase in shock loss with Mach number is 3 to 18 times as large as the increase in profile loss (assuming β_1 is held fixed). This observation supports Schreiber's (1987) conclusion that the increase in total

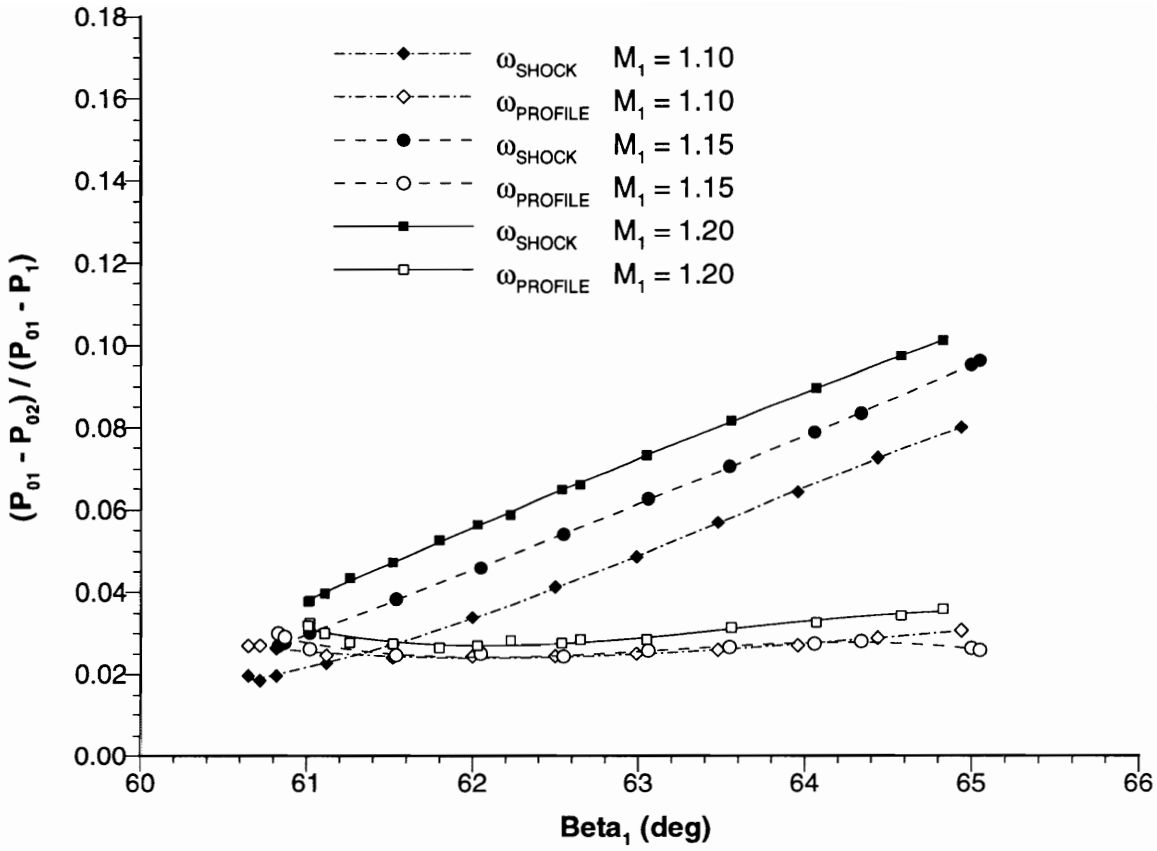

Figure 55. Comparison of the shock loss and viscous profile loss coefficients obtained from CFD for the L030-6 cascade

pressure loss that occurs with increasing Mach number is predominantly caused by an increase in shock loss. This is also shown by Schreiber's data in Figure 26 (page 69).

The present shock loss predictions have shown good agreement with both the experimental measurements and the CFD results for unstarted operation of the L030-6 cascade over the range of inlet Mach numbers considered. Agreement with this data set alone, however, cannot be considered as proof of the general applicability of the method because the empirical constant in the bow shock model was adjusted to match the performance of this cascade (although at a single near-stall condition). To further establish the validity of the present shock loss model, the performance of the L030-4

cascade was predicted. Because there are significant differences in profile shape and blade angles between these 2 configurations, the L030-4 cascade can be considered a "blind" test case to evaluate the accuracy of the present method.

The total pressure loss coefficients for unstarted operation of the L030-4 cascade with an inlet Mach number of 1.10 are shown in Figure 56. The CFD solutions show a strong increase in shock loss with increasing inlet flow angle, as was shown for the L030-6 solutions. Although the measurements indicate an similar increase, the slope of the experimental shock loss curve is smaller than suggested by the CFD.

The maximum difference between the shock loss coefficients predicted by the

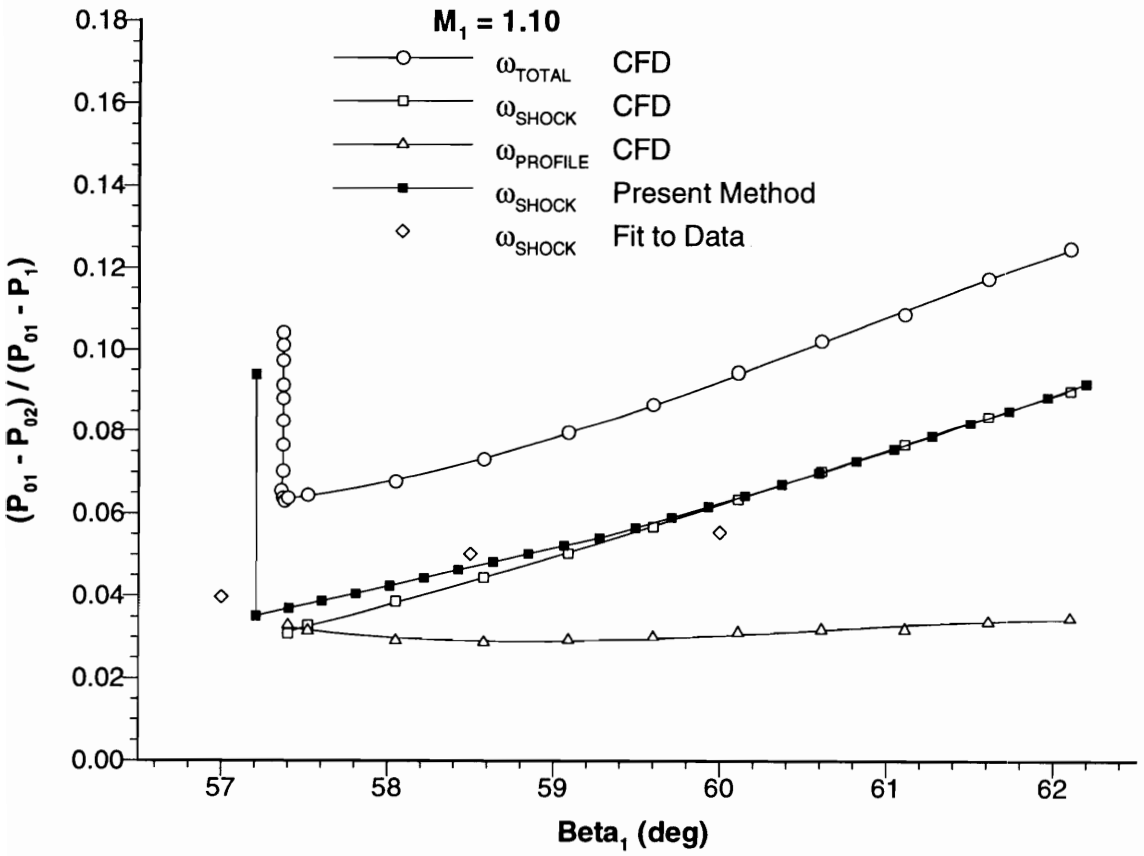

Figure 56. Loss coefficient comparison for unstarted operation of the L030-4 cascade with M_1 = 1.10

present method and by the CFD was 0.006 for this Mach number and occurred at $\beta_1 = 57.4°$ (the cascade start/unstart point predicted by the CFD). For inlet flow angles greater than 60°, there was negligible difference between the model predictions and the shock loss obtained from the CFD. The maximum difference between the present predictions and the measured shock loss coefficients was 0.007 and occurred at $\beta_1 = 58.5°$.

The shock loss coefficients predicted by the present method for the L030-4 cascade operating with an inlet Mach number of 1.02 are compared to the measurements *only* in Figure 57. Although CFD solutions were generated for this low Mach number,

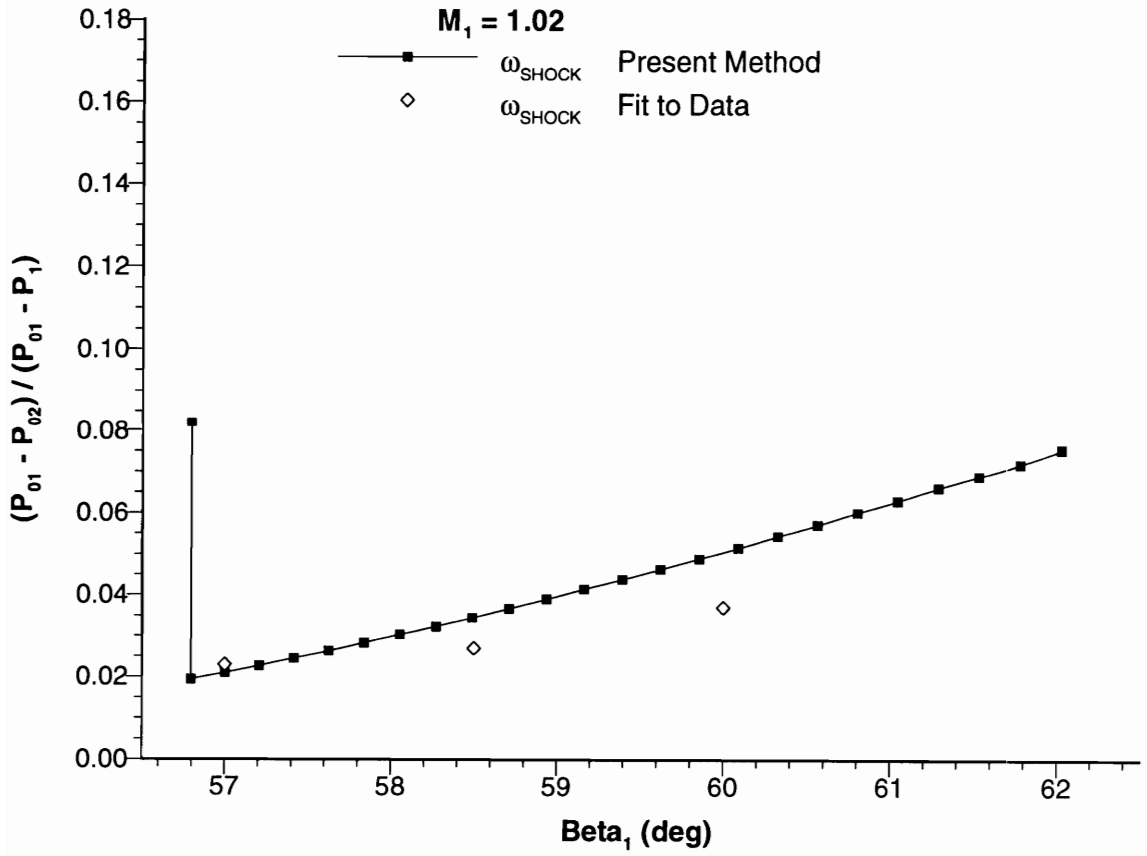

Figure 57. Loss coefficient comparison for unstarted operation of the L030-4 cascade with $M_1 = 1.02$

the author does not believe that they accurately represent the actual cascade flow field and they are not presented. The low supersonic flow regime poses an exceptional challenge for Navier-Stokes solvers because the bow waves extend a significant distance upstream of the blade. As discussed in Chapter 4, the strong portion of these bow waves crosses the periodic boundary of the computational domain and cannot be resolved because of poor grid quality. The inability of CFD to accurately predict this flow regime should be viewed as a *limitation* of the Navier-Stokes method, however, not as a contradiction.

The predicted shock loss coefficients compare favorably with the measurements near the cascade start/unstart point, but the slope of the measured shock loss curve is again smaller than the slope of the predicted curve. For $\beta_1 = 60°$, the difference between the present prediction and the measured shock loss coefficient was 0.014. While this was the largest prediction error noted among all of the unstarted comparisons made in the present investigation, the author still considers this to be a reasonably accurate estimate.

7.3 Discussion of Unstarted Shock Loss Prediction

The present shock loss prediction method considers separately the effects of the detached bow shock and of the passage shock. For unstarted operation, the curved portion of the passage shock is small and the entire passage shock can be reasonably approximated as a normal shock. Miller, et al. (1961) used this approximation and calculated the loss from a normal shock with an upstream Mach number that was the arithmetic average of the Mach number at the leading-edge and at the suction surface shock impingement point. Wennerstrom and Puterbaugh (1984) assumed a normal passage shock and used a 3-point numerical integration of the loss. The upstream Mach number and shock obliqueness angle were assumed to vary linearly across the passage, however, and not as a direct result of suction surface curvature.

In both of the above models, the Mach number at the blade leading edge (pressure side of the passage) was assumed to be the upstream value rather than the value along the first captured Mach wave. Because the flow undergoes a Prandtl-Meyer expansion around the blade leading edge, the Mach number along the first captured Mach wave is generally higher than the upstream value and the above methods will slightly under-predict the loss. In the present investigation, both the upstream Mach number and the shock obliqueness angle are determined by extending a Mach line from the suction surface to the passage shock at 200 locations. This approach allows a more accurate inclusion of the nonlinear effects of Mach number and shock angle on total pressure loss than do the previously published methods. The improved agreement obtained from the present method is shown in Figure 58 for the start/unstart point of the L030-6 cascade operated over a range of Mach numbers. (Off-design comparisons are not possible because the Miller, et al. (1961) and the Wennerstrom and Puterbaugh (1984) shock loss models are applicable only at the minimum overall loss point).

The present prediction method also considers the total pressure deficit that is produced by the detached shock waves that stand ahead of the cascade. While Starken, et al. (1984) suggested this effect be included in the continuity equation for the minimum-incidence calculation, it has not been included in previously published shock loss models. To demonstrate the significance of the bow shock loss as a fraction of the present shock loss prediction, the following bow shock loss coefficient is defined.

$$\omega_{bow} = \frac{1 - \frac{P_{0A}}{P_{01}}}{1 - \frac{P_1}{P_{01}}} \tag{90}$$

where P_{0A}/P_{01} is the total pressure reduction caused by the detached bow shock and is

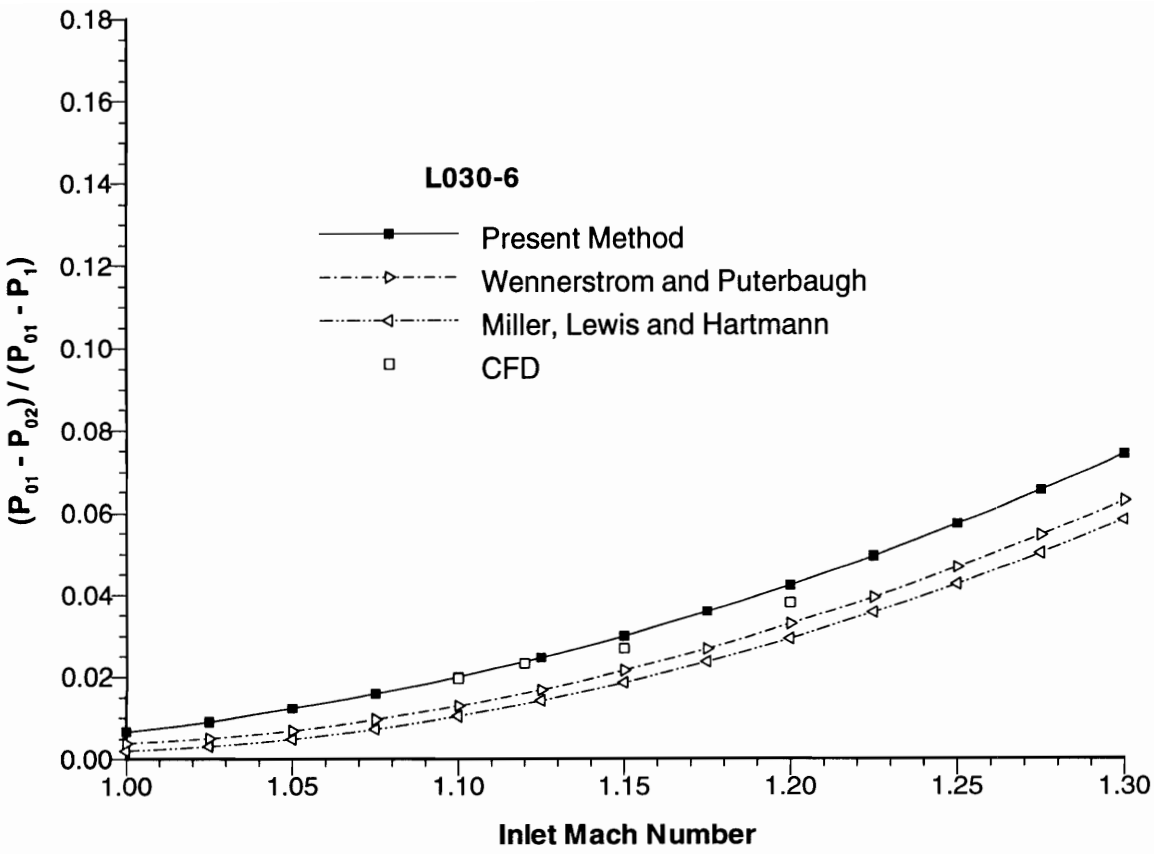

Figure 58. Comparison of shock loss prediction methods for the L030-6 cascade start/unstart point as a function of inlet Mach number

obtained from the method presented in Section 6.2. A passage shock loss coefficient is then defined as the difference between the predicted shock loss coefficient and the bow shock loss coefficient.

$$\omega_{passage} = \omega_{shock} - \omega_{bow} \tag{91}$$

Figures 59 through 63 identify the bow-shock and passage-shock loss components of the present prediction method for all of the unstarted operating conditions that were

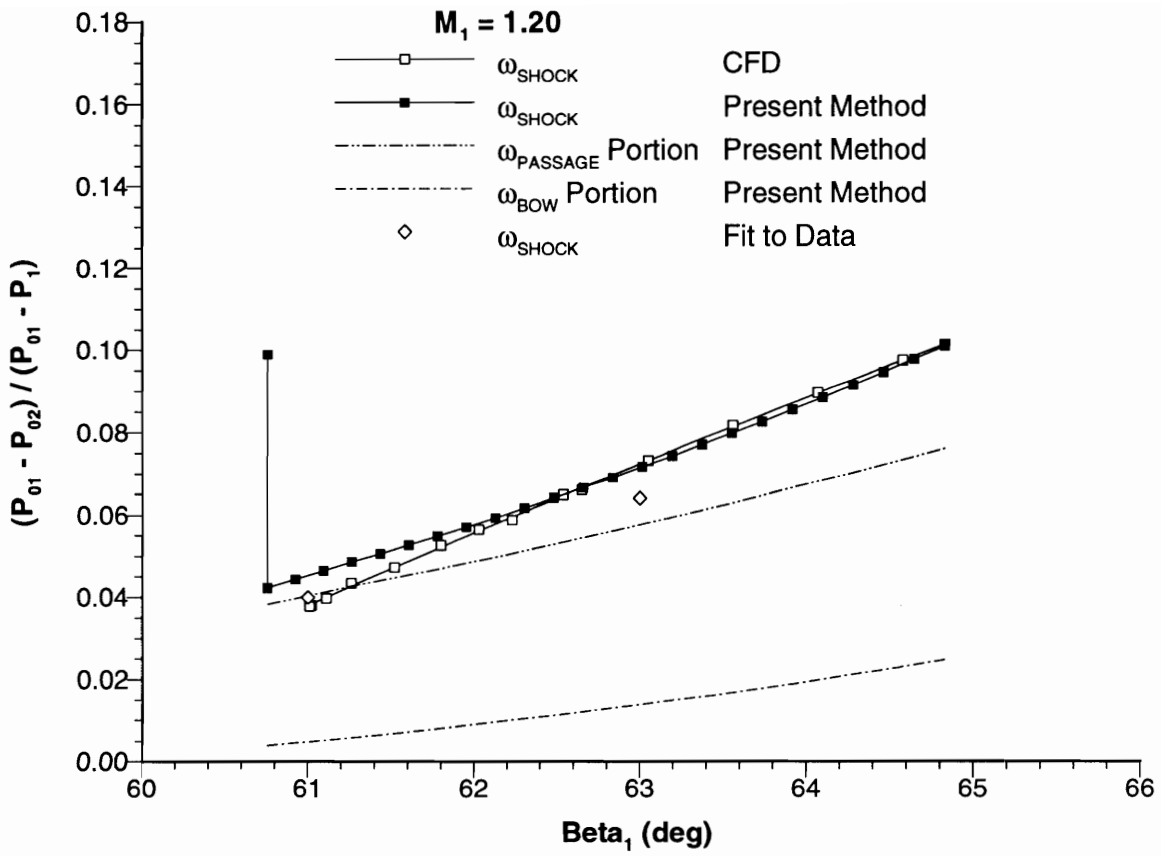

Figure 59. Identification of loss attributed to passage shock and to bow wave for unstarted operation of the L030-6 cascade with M_1 = 1.20

presented in the previous section.[1] The measured shock loss coefficients and the values obtained from CFD are included for comparison, but the overall loss and the viscous loss obtained from CFD are omitted from these figures for clarity.

The bow shock loss is shown to be small at the cascade start/unstart point, with values ranging from 0.003 to 0.004. This is consistent with observations of the started CFD solutions which indicate that the rotational effects of the bow shock are small and, except for a small region near the blade surface, that the entrance-region characteristics

[1] Symbols are omitted from the bow shock and passage shock loss curves in Figures 59 through 63 to indicate that these are only a *portion* of the present shock loss prediction method and should not be considered separately.

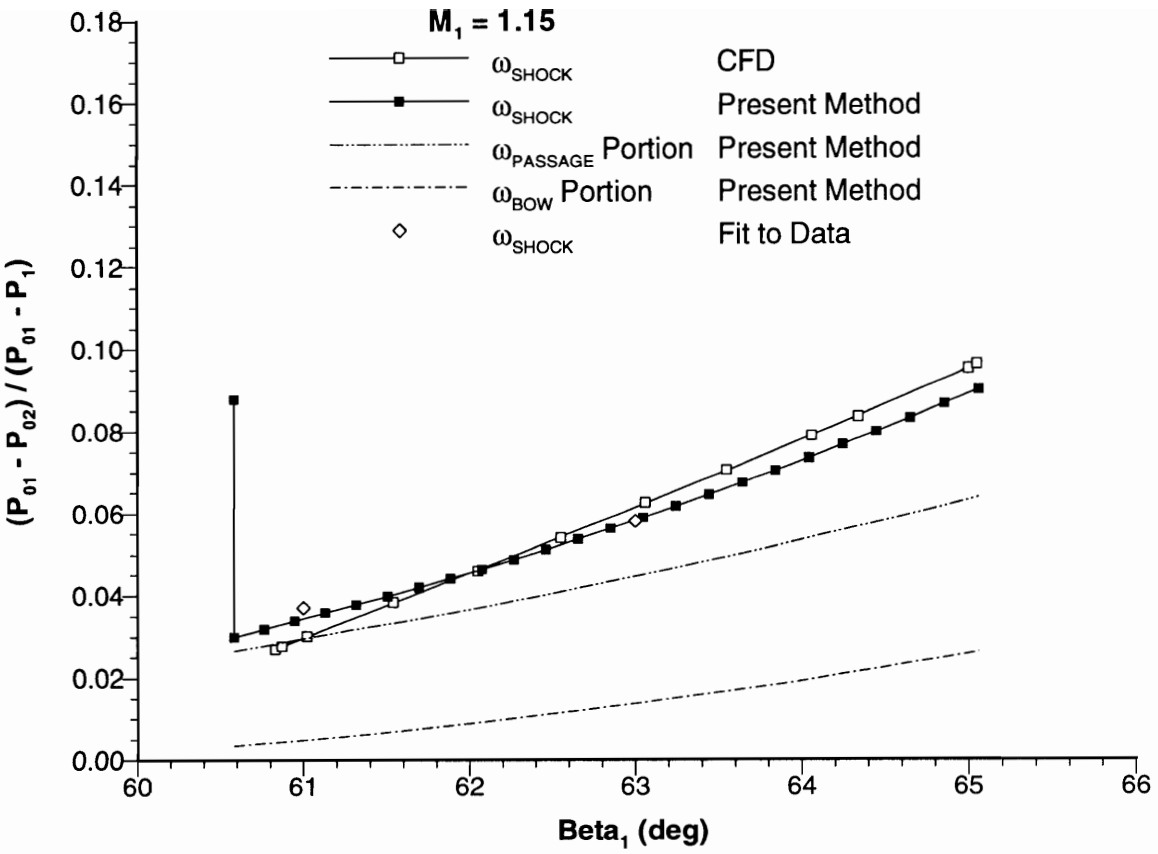

Figure 60. Identification of loss attributed to passage shock and to bow wave for unstarted operation of the L030-6 cascade with M_1 = 1.15

are nearly straight. The bow shock loss increases significantly with incidence, and is about 0.025 near stall for all of these configurations. This is again consistent with the CFD solutions, which indicate that the strong portion of the bow wave extends farther from the blade as incidence increases.

The present bow wave calculation has 2 significant effects on the predicted shock loss coefficients, and these are unique contributions of the present approach. The first (and most obvious) of these is that the predicted shock loss directly reflects this total pressure deficit. While this effect is small at the start/unstart point, it is clearly important as stall is approached. This suggests that the bow shock produces a significant fraction of

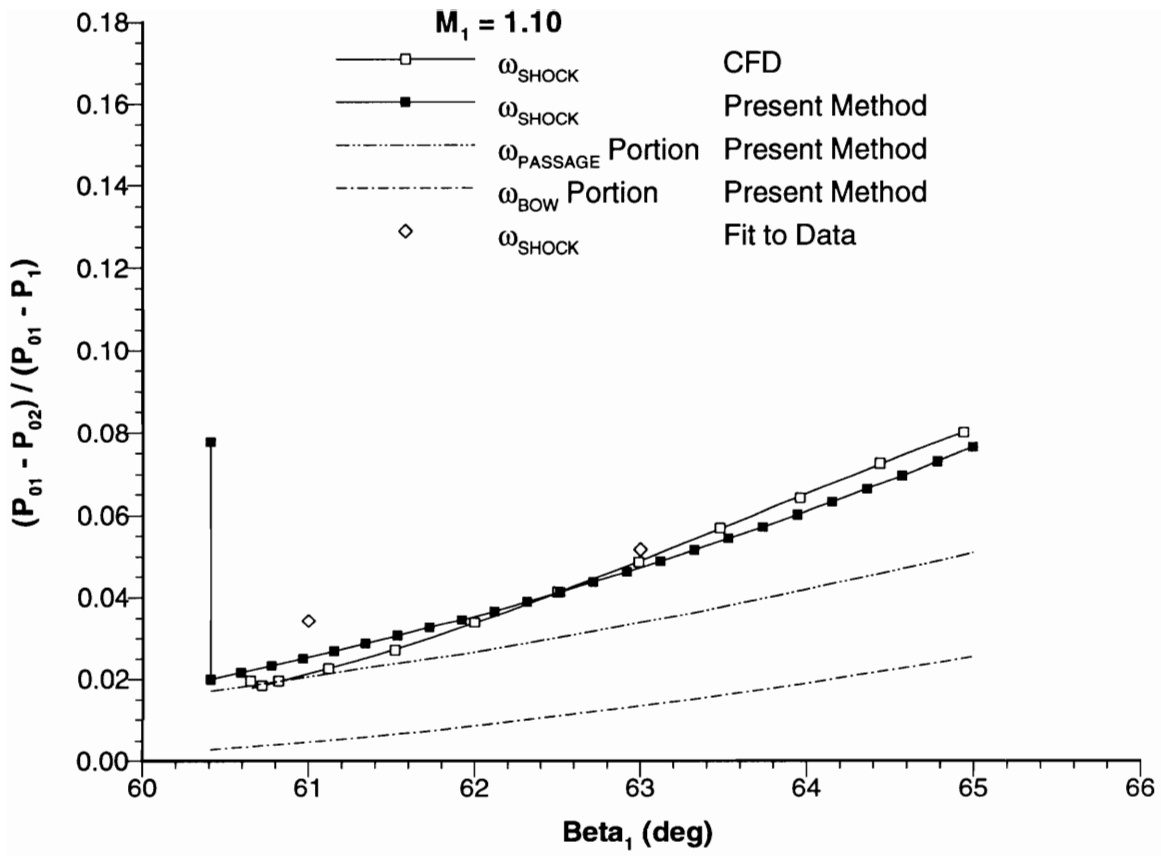

Figure 61. Identification of loss attributed to passage shock and to bow wave for unstarted operation of the L030-6 cascade with M_1 = 1.10

the shock loss during unstarted operation, and that this mechanism must be included in an off-design performance model. The second effect is that inclusion of the bow shock loss in the continuity equation results in a slightly higher Mach number along the first captured Mach wave. This higher Mach number then produces passage shock loss coefficient that is between 0.002 and 0.010 larger than if the bow wave loss were neglected.

The differences between the assumed (straight) inlet-region characteristics and the actual curved characteristics will clearly increase with incidence, as the spatial extent of the rotational flow region increases, but this is considered unimportant to the present analysis. The goal of the present method is to obtain an engineering shock loss model,

not an exact prediction of point-to-point flow properties. Although the present model involves certain simplifying assumptions, it is a physics-based approach with a minimum of empiricism and good agreement with the available validation tools has been obtained.

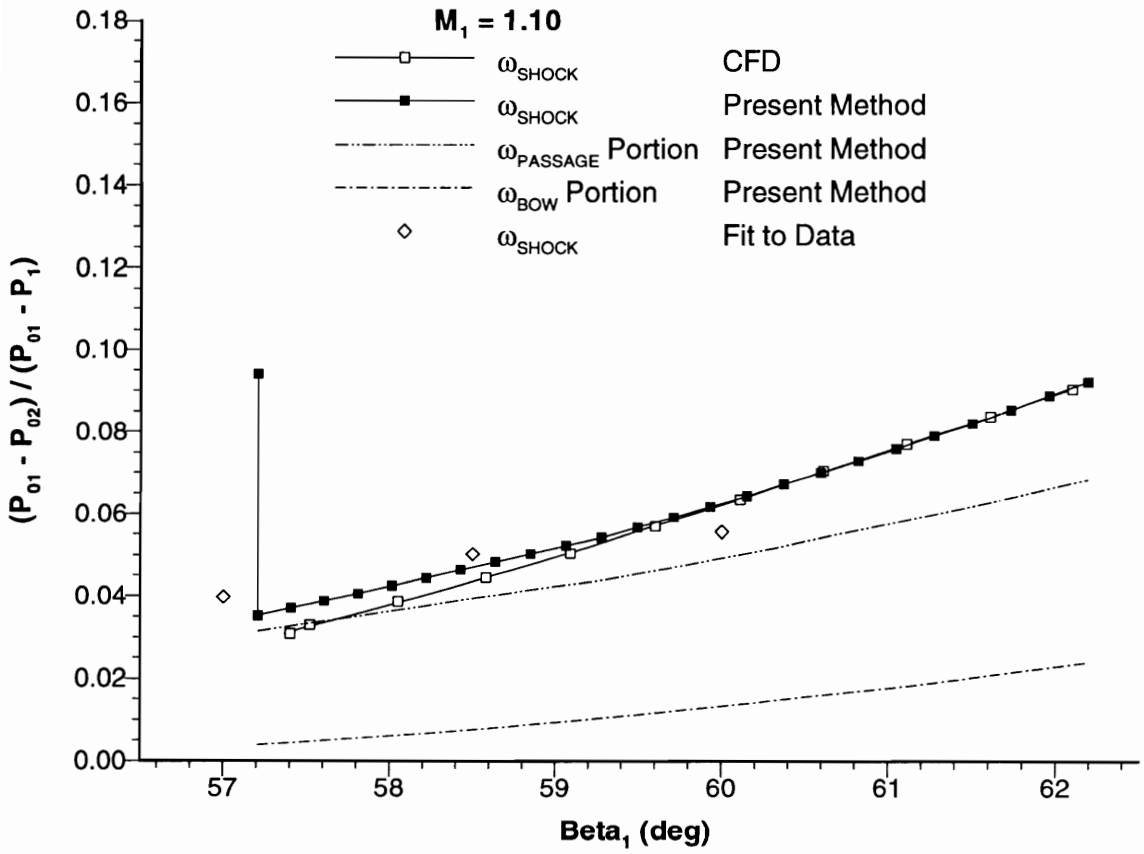

Figure 62. Identification of loss attributed to passage shock and to bow wave for unstarted operation of the L030-4 cascade with M_1 = 1.10

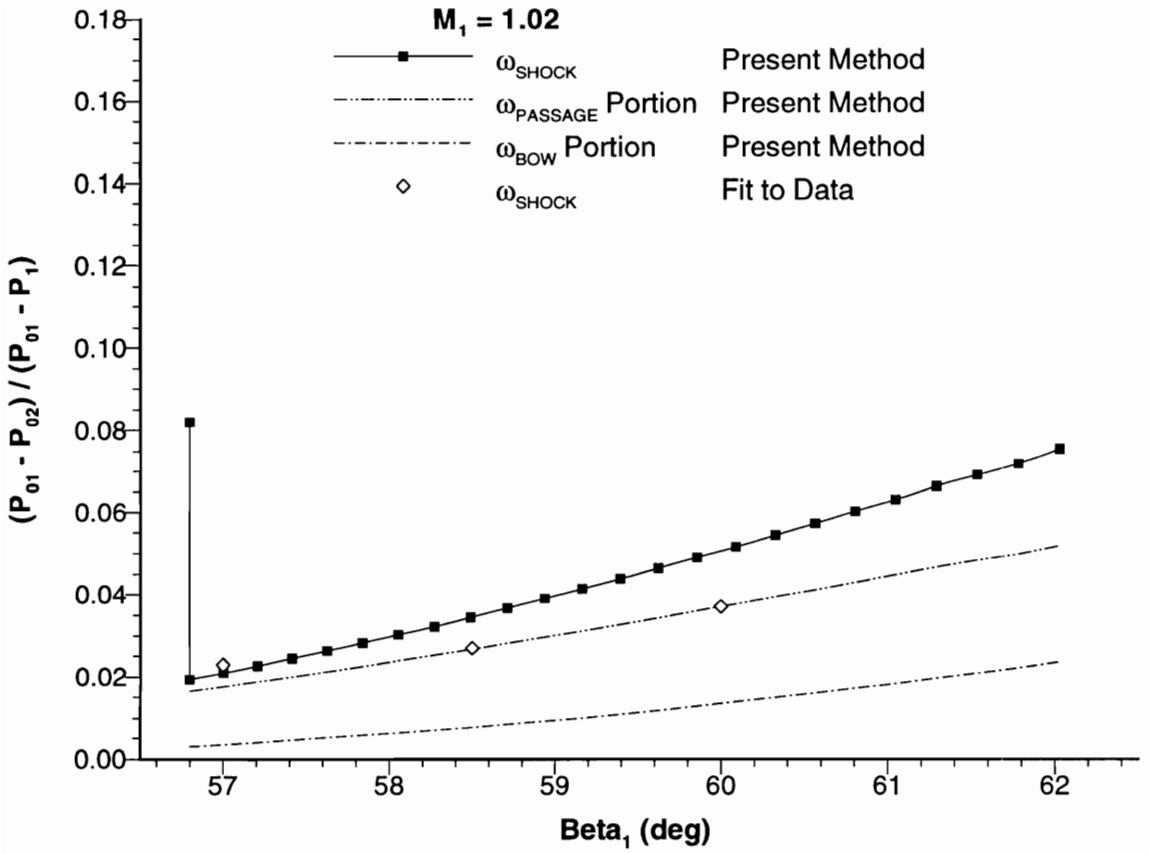

Figure 63. Identification of loss attributed to passage shock and to bow wave for unstarted operation of the L030-4 cascade with M_1 = 1.02

7.4 Started Cascade Results

Started cascade performance is typically plotted with exit static pressure as the abscissa because, for a fixed inlet Mach number, this is the parameter that has the largest effect on the flow field. Presentation of experimental data in this manner is fairly straightforward because the exit pressure is a measured quantity. This poses a significant challenge for a prediction method, however, because the downstream static pressure is strongly influenced by the total pressure loss and the exit flow angle. Because the flow deviation angle and the viscous portion of the total pressure loss are not addressed in the

present investigation, the downstream pressure cannot be predicted and an alternate presentation method must be used.

The total pressure loss coefficients for started operation of the L030-4 cascade with an inlet Mach number of 1.10 are presented in Figure 64. The abscissa in this figure is the axial coordinate of the suction surface shock impingement point, which is a known quantity from the present loss model. (This shock impingement point is point *C* from Figure 46 (page 111) for "medium" back pressure operation, and point *E* from Figure 48 (page 116) in the "low" back pressure regime.) For the CFD solutions, this coordinate was approximated by extending the nearly-straight portion of the sonic Mach contour from the free-stream passage flow to the blade surface, ignoring the curvature of the

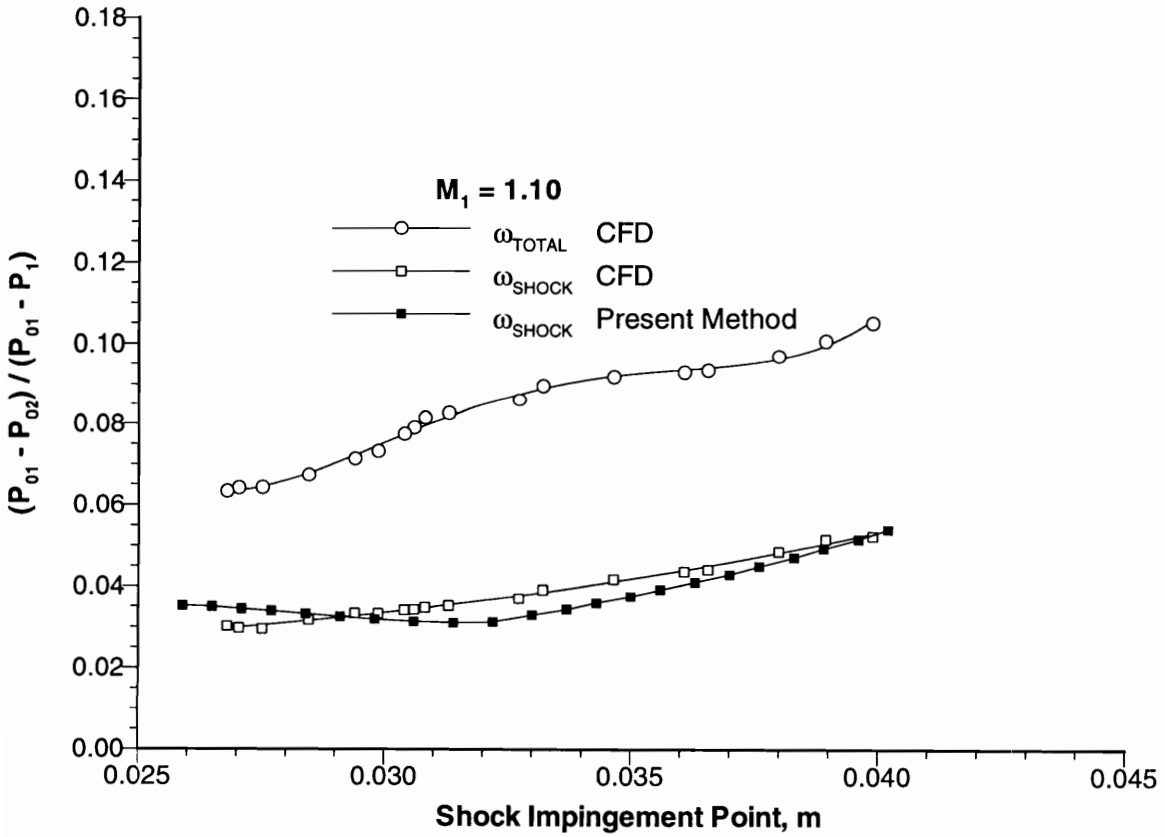

Figure 64. Loss coefficient comparison for started operation of the L030-4 cascade with M_1 = 1.10

Mach contours in the boundary layer. This is clearly not an exact method, but it does capture the general trend of the shock moving downstream during started operation.

The overall total pressure loss coefficients obtained from the CFD are included in this figure to correlate the shock position with overall cascade performance. Although the viscous profile loss coefficients obtained from the CFD have similar magnitude to the shock loss values, the former showed no clear trends during unstarted operation. To avoid unnecessarily cluttering this and later figures, the viscous losses are omitted. No started shock loss measurements were presented by Schreiber (1987), so the CFD solutions are the only available validation tool for the L030-4 and L030-6 cascades in this flow regime.

The suction surface shock impingement coordinate predicted by the present method for the cascade start/unstart point is within 0.9mm of that obtained from the CFD solutions. Since both the L030-4 and L030-6 cascades had 90mm chord length, this can be considered reasonable agreement. A minor improvement in the predicted shock position could be made by including the effects of suction surface boundary layer growth on the flow angle along each characteristic, but it is unlikely that this would have a significant effect on the predicted shock loss.

Referring to Figure 64 (page 136), the agreement between the shock loss coefficients predicted by the present method and those obtained from CFD is fairly good, with a maximum difference of 0.006. In the "medium" back pressure regime, the present model predicts a small decrease in shock loss coefficient as the normal portion of the shock moves downstream and the flow diffusion is more evenly distributed across 2 shocks. The minimum shock loss for this configuration is predicted at the intersection of the "medium" and "low" back pressure flow regimes, when the shock impingement point is at $x = 32.2\,\text{mm}$. The shock loss is then predicted to increase steadily as the second

passage shock moves downstream from this point and the Mach number ahead of this shock increases. Although the CFD indicates an initial decrease in shock loss in the "medium" back pressure regime, this decrease is negligible and the shock loss then increases gradually as the shock moves downstream.

The shock loss coefficients predicted by the present method for started operation of the L030-6 cascade with an inlet Mach number of 1.10 are compared to those obtained from CFD in Figure 65. The agreement is again seen to be reasonably good, with a maximum difference of 0.007. As with the previous comparison of L030-4 performance, the minimum predicted shock loss occurs at the intersection of the "medium" and "low" back pressure flow regimes ($x = 31.6\,\text{mm}$). The CFD solutions again indicate a minor

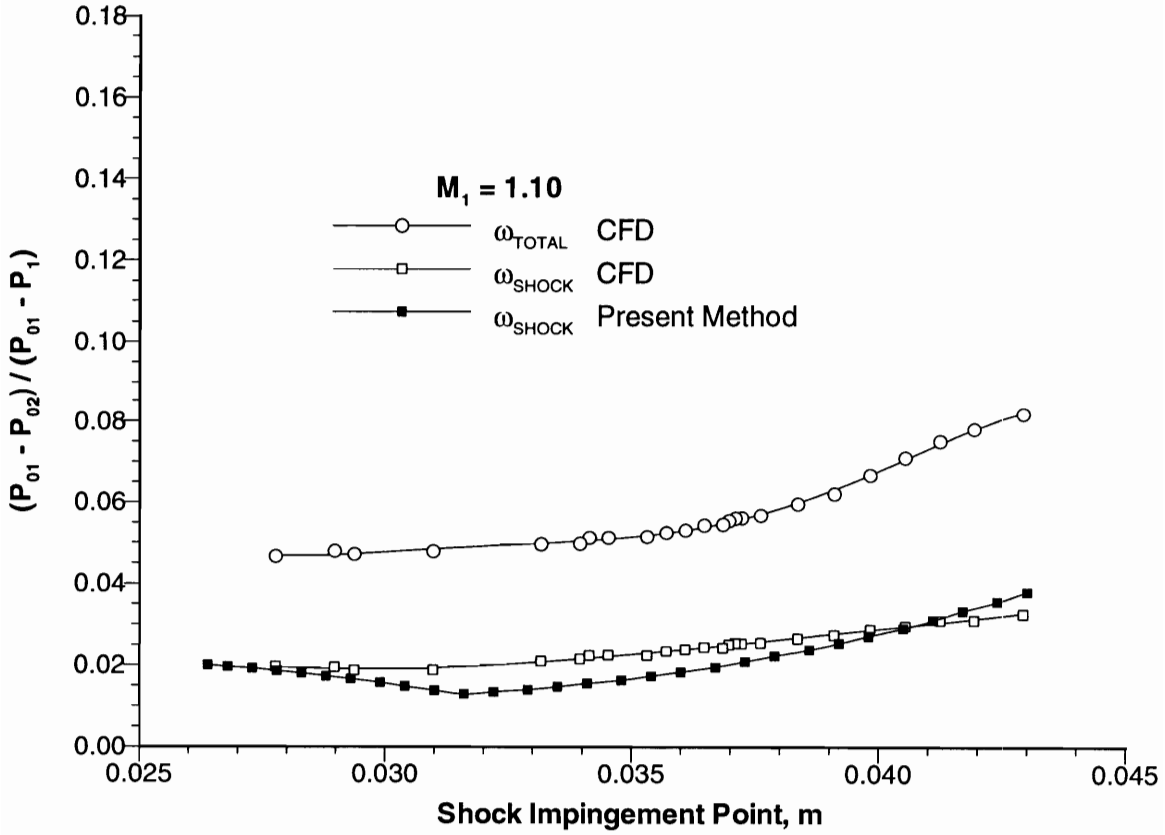

Figure 65. Loss coefficient comparison for started operation of the L030-6 cascade with $M_1 = 1.10$

decrease in shock loss followed by a gradual increase as the shock moves downstream.

The shock loss coefficients predicted by the present method for started operation of the L030-6 cascade with an inlet Mach number of 1.15 are compared to those obtained from CFD in Figure 66. In the "medium" back pressure regime, with a shock impingement coordinate forward of $x = 34.3\,\text{mm}$, the agreement between the present shock loss predictions and the values obtained from CFD is quite good, with a difference of 0.002 or less. As the shock moves downstream into the "low" back pressure regime, the slope of the predicted shock loss curve is again steeper than suggested by the CFD.

The agreement between the present shock loss predictions and the values obtained from CFD for started operation of the L030-6 cascade with an inlet Mach number of 1.20

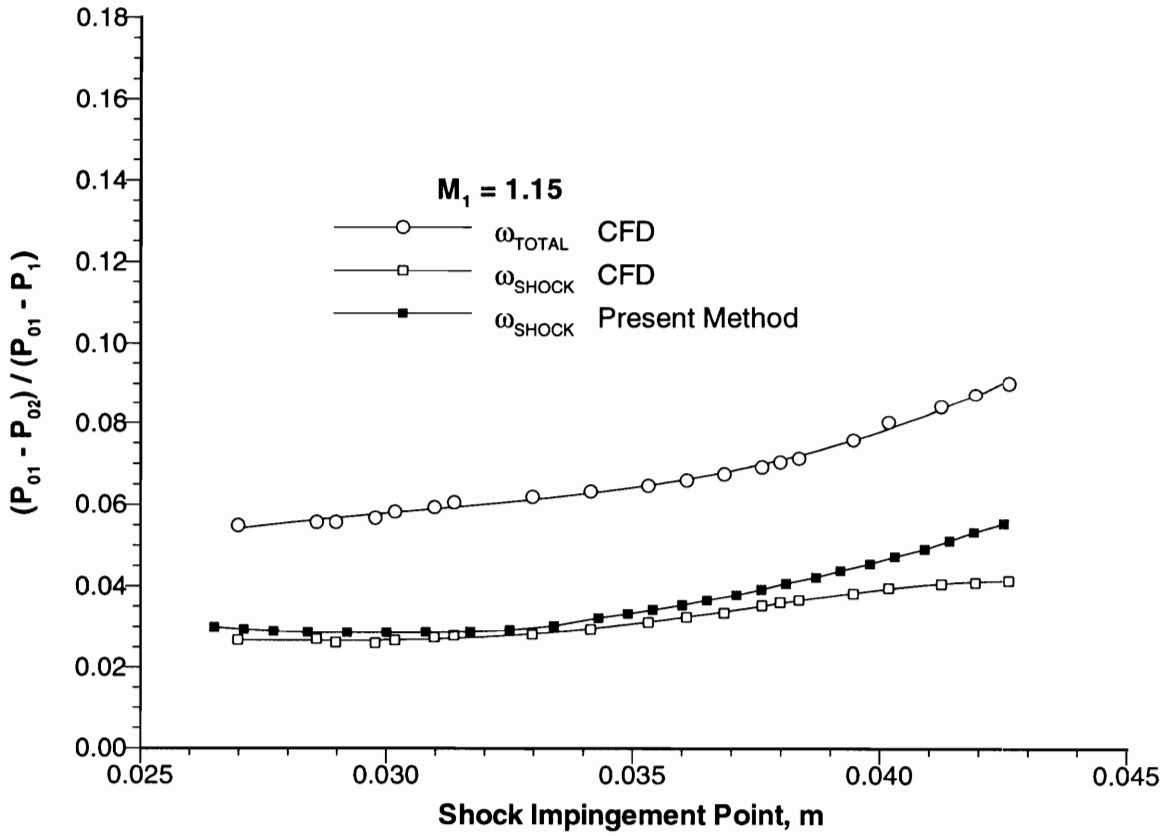

Figure 66. Loss coefficient comparison for started operation of the L030-6 cascade with $M_1 = 1.15$

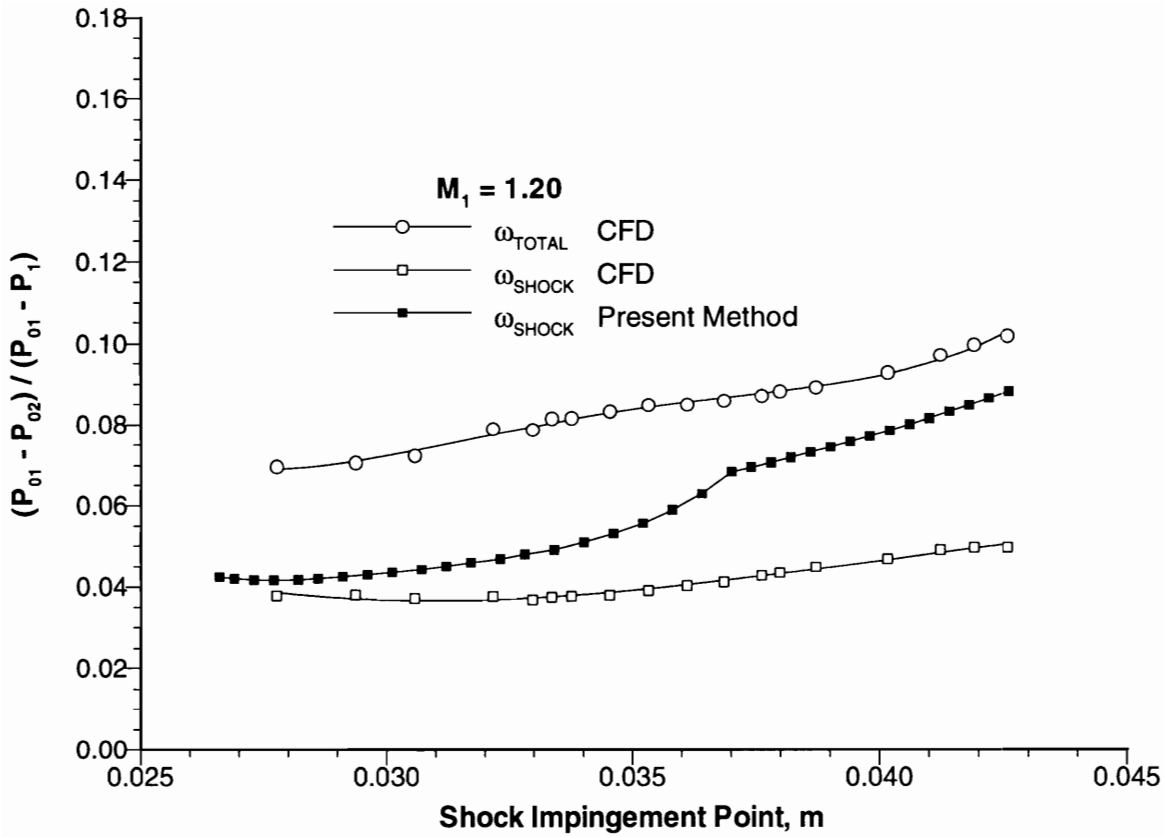

Figure 67. Loss coefficient comparison for started operation of the L030-6 cascade with M_1 = 1.20

is shown in Figure 67. The present model produces a reasonable prediction near the cascade start/unstart point, with a difference of 0.005. As the shock moves downstream, however, the agreement within the "medium" back pressure regime becomes marginal and the agreement in the "low" back pressure regime is poor.

7.5 Discussion of Started Shock Loss Prediction

In the "medium" back pressure regime, the passage shock structure consists of a weak shock that spans a portion of the blade passage and a normal shock that spans the entire passage. The weak portion of this shock is approximated in the present investigation by the Moeckel (1949) method, which is a near-field analysis of the

detached shock standing ahead of an isolated object in a supersonic stream. (In this context, the term "near-field" refers to the flow between the vertex and the sonic point on the shock.) This method predicts a shock shape that is reasonably accurate within several diameters of the body, but that approaches the free-stream Mach lines too rapidly in the far-field region (Moeckel, 1949; 1950).

Near the cascade start/unstart condition, the transition point between the weak portion of the passage shock and the normal shock (point *T* in Figure 46, page 111) is near the sonic point on the weak shock, *s*. Under these conditions, the present method has been shown to provide very reasonable shock loss predictions. As the shock transition point moves closer to the blade suction surface, however, insufficient diffusion is predicted across the weak shock and the Mach number predicted ahead of the normal shock is then too high. For the lower inlet Mach numbers considered, the Mach number downstream of the weak shock is only slightly supersonic, and the resulting error in the present loss predictions is small. This is why good agreement between the present method and the shock loss extracted from the CFD is good in Figures 64 through 66. The loss attributed to the normal shock increases rapidly with Mach number, however, causing the substantial over-predictions shown in Figure 67.

For all of the "low" back pressure comparisons presented in Figures 64 through 67, the slope of the predicted shock loss curve is steeper than suggested by the CFD, and there are 2 apparent reasons for this. In this flow regime, the passage shock system consists of a weak full-passage shock followed by a nearly normal shock. As discussed above, too little diffusion is calculated across the weak shock, and the predicted Mach number ahead of the normal shock at the intersection of the "low" and "medium" back pressure regimes is too high. Even if the exact pre-shock Mach number were known here, however, the present method neglects the viscous effects in the downstream region,

and this causes too much expansion to be calculated between the weak and normal shocks. This can be seen by writing the continuity relation in the following form.

$$F(M) = \frac{\dot{m}\sqrt{c_p T_0}}{P_0 A} \tag{92}$$

The viscous blade boundary layers in an actual cascade produce a continuous decrease in stagnation pressure between the inlet and exit, so the correct "average" P_0 will undoubtedly be smaller than the value assumed from an isentropic expansion. Furthermore, the blockage produced by these boundary layers will reduce the available flow area. Both of these effects cause the Mach number ahead of the normal shock in an actual cascade to be lower than predicted by the present method. This, in turn, causes the slope of the predicted "low" back pressure shock loss curve to be too steep.

While the present method for predicting started shock system performance is clearly oversimplified, it is the most comprehensive choked-operation, multiple-shock model in the open literature.

7.6 Implementation of an Overall Loss Prediction Method

To further demonstrate the significance of the present analysis, it has been used as the basis of a simplified overall loss prediction method. As mentioned previously, the total pressure loss produced by the profile boundary layers is not addressed in the present method, so an estimate for the viscous loss must be obtained from another source. It was shown in Figures 52 through 56 (pages 121 through 126) that the profile loss is nearly constant for unstarted operation. Although these figures suggest that a reasonable overall loss prediction might be obtained by adding a constant value to the unstarted shock loss predictions, they offer little guidance on which value to add. In an industrial setting, this

quantity would likely be obtained from a proprietary version of Lieblein's (1956) loss as a function of diffusion factor, D. For the present demonstration, however, the constant value of viscous loss coefficient was obtained from the CFD solution at the cascade start/unstart point for each Mach number considered.

To be clear, it is not suggested that a useful overall loss model can be obtained if CFD solutions must be run to obtain the viscous loss component. If this were the case, the overall loss could be obtained directly from the CFD. It is simply stated that an accurate estimate of the profile loss must be included in this proof-of-concept demonstration, and that CFD provides the most accurate profile loss estimate available to the present author.

In Figure 68, the overall loss coefficients obtained by adding a constant value to the present unstarted shock loss predictions are compared to the measured performance of the L030-6 cascade with an inlet Mach number of 1.20. The prediction for the choked portion of the characteristic was obtained by extending a vertical line upward from the cascade start/unstart point by an arbitrary amount. The agreement shown in this figure can be considered quite good, with the maximum difference between measured and predicted loss coefficients of less than 0.01 over the entire unstarted range of operation.

The overall loss coefficients obtained in the manner described above for the L030-6 cascade with an inlet Mach number of 1.12 are presented in Figure 69. For inlet flow angles up to 63.0°, the agreement between the predictions and the measured performance is good, with a maximum difference of 0.012. Near stall, the agreement is fair, with a maximum difference of 0.028. Although an entire speedline of CFD solutions was not obtained for this Mach number, the solutions run for $M_1 = 1.10$ and 1.15 suggest that the significant increase in measured loss near stall is the result of a shock-induced boundary layer separation.

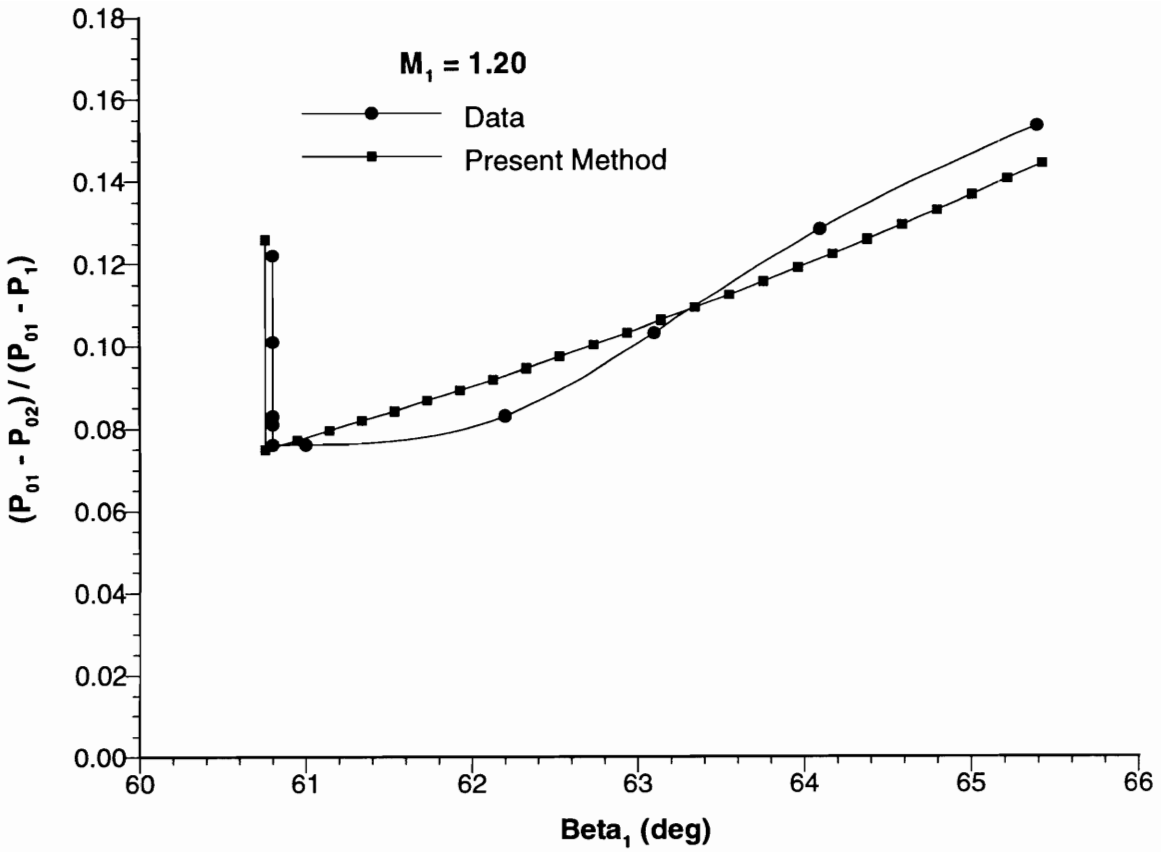

Figure 68. Comparison of measured overall loss coefficients and those obtained by adding a constant profile loss value to the present shock loss predictions for the L030-6 cascade with M_1 = 1.20

The overall loss coefficients obtained in the manner described above for the L030-4 cascade with an inlet Mach number of 1.10 are presented in Figure 70 (page 146). For inlet flow angles up to about 61.3°, the agreement between the predictions and the spline that connects the measured loss coefficients is good, with a maximum difference of 0.012. For larger incidence angles, the measured loss increases dramatically and the agreement is poor. Again, the CFD solutions suggest this is the result of a shock-induced boundary layer separation.

The line extending above and to the right of the measured loss coefficient for $\beta_1 = 61.5°$ implies a measured near-stall condition ($\beta_1 = 63.1°$, $\overline{\omega} = 0.190$) which is off

the scale of the figure. Although it is possible to operate this cascade with an inlet flow angle greater than 61.5°, it is clearly undesirable to do so because the efficiency would be very low. The 4° range of incidence between the cascade start/unstart point and $\beta_1 = 61.3°$ represents the most useful operating region of the cascade, and agreement on this portion of the characteristic is of greatest practical importance to a compressor designer.

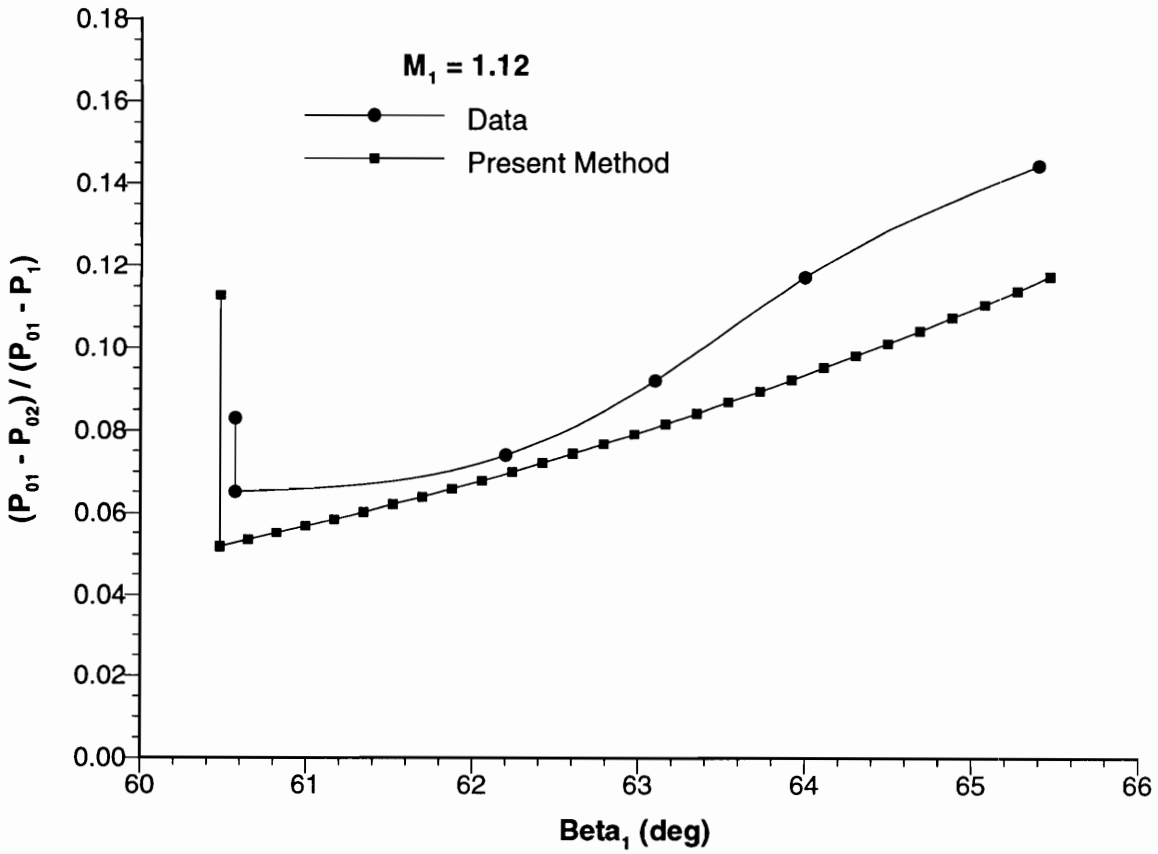

Figure 69. Comparison of measured overall loss coefficients and those obtained by adding a constant profile loss value to the present shock loss predictions for the L030-6 cascade with M_1 = 1.12

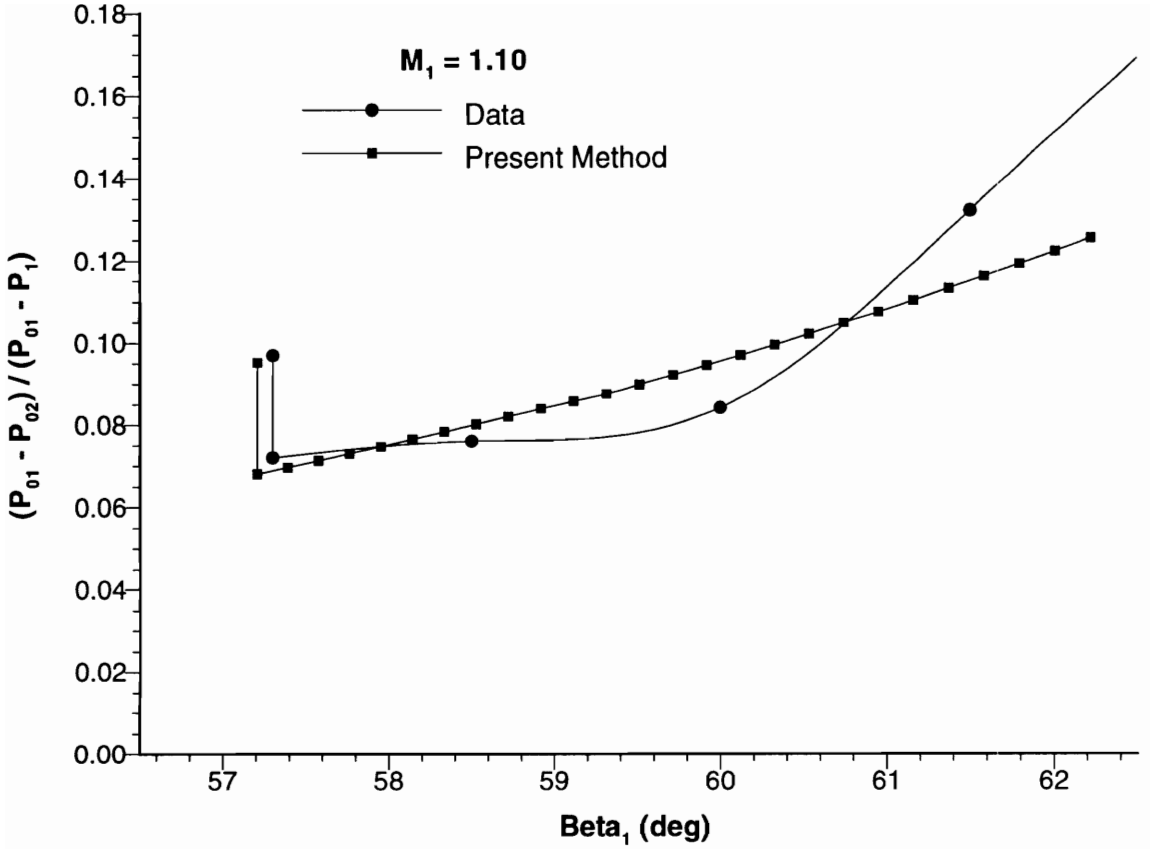

Figure 70. Comparison of measured overall loss coefficients and those obtained by adding a constant profile loss value to the present shock loss predictions for the L030-6 cascade with M_1 = 1.10

8. Summary and Conclusions

The existing literature on compressor loss modeling has been reviewed, and the limitations of the various methods have been identified by including the salient details of their development. The physical mechanisms that affect the flow in two-dimensional supersonic compressor cascades have been reviewed, including the changes in shock geometry that will occur with back pressure for both started and unstarted operation. Compressible fluid mechanics has been applied to the known shock geometry to obtain a physics-based engineering shock loss model that is applicable over the entire supersonic operating range of the cascade.

The flow upstream of the passage shock is assumed to be steady, inviscid, and supersonic, with a subsonic axial component. The curvature of the left-running characteristics in the entrance region is neglected, although the rotational effects of the detached bow shock are included in the continuity equation in an approximate way, as suggested by Starken, et al. (1984). Unlike other methods (e.g., Freeman and Cumpsty, 1992), the present model requires no measured information about the exit flow properties, and predicts the entire shock loss characteristic directly from blade geometry and inlet Mach number.

The total pressure loss produced by the shock system is estimated by considering separately the effects of the detached bow shock and of the passage shock(s). For started operation, the method of Moeckel (1949) is used to approximate the shape of the bow shock, and its performance is numerically integrated as though it were in a uniform stream, as suggested by Klapproth (1950). For unstarted operation, the effects of the increased bow shock detachment distance are approximated by applying the Moeckel method with a leading edge radius that is larger than the actual size. This is a unique

contribution of the present method and is shown to have a significant effect on the shock performance predictions.

The performance of the passage shock is also integrated numerically, but the variation of flow properties immediately upstream of the shock is included directly by extending a Mach line from the suction surface to each integration point on the shock. The method of Wennerstrom and Puterbaugh (1984) includes a numerical integration of the passage shock, but assumes a linear variation of Mach number and shock angle between the leading edge and the suction surface. The present approach is an improvement over the previously published method and allows a more accurate inclusion of the nonlinear effects that these quantities have on the total pressure loss.

The L030-4 and L030-6 supersonic compressor cascade tests (Schreiber, 1987) have been used to examine the accuracy of the proposed shock loss model. Because the experimental results for these cascades were presented for 3 or fewer inlet flow angles, a Navier-Stokes analysis was conducted to identify the qualitative trends expected to exist between the measured conditions.

The present fundamentally-based model accurately captures the shock loss trends and magnitudes for unstarted operation of both cascades for the range of inlet Mach numbers considered, and the following conclusions can be drawn from this investigation.

- The dramatic increase in overall loss with increasing inlet flow angle is primarily the result of increased shock loss. For a given Mach number, the viscous profile loss is nearly constant over the entire unstarted operating range of the cascade, unless a shock-induced boundary layer separation occurs near stall.
- Much of the increased total pressure loss that occurs with increasing incidence is caused by the detached bow shock.
- Shock loss is much more sensitive to inlet Mach number than is viscous profile loss.

For started operation, insufficient diffusion is calculated across the weak passage shock approximated by the Moeckel (1949) method, and the Mach number predicted immediately ahead of the normal shock is too high. For low inlet Mach numbers, this has only a modest effect on the predicted shock loss, but this is the source of significant error as the inlet Mach number increases.

For "low" back pressure operation, the viscous effects downstream of the weak passage shock have a considerable influence on the Mach number that exists upstream of the normal shock. Accurate prediction of this shock-boundary layer interaction is beyond the current state-of-the-art, and is not considered in the present method. Accordingly, the Mach number ahead of the second passage shock, and the loss produced by this shock, is predicted to increase too rapidly as the second passage shock moves downstream.

The present shock loss model has been used as the basis for an overall loss prediction method by adding a constant value, representative of the viscous profile loss, to the predicted unstarted shock loss coefficients. For the present investigation, this constant value of viscous loss coefficient was obtained from the CFD solution at the cascade start/unstart point for each Mach number considered, although any suitable profile loss model could be used. The started portion of the loss characteristic was established by extending a vertical line upward from the cascade start/unstart point obtained as stated above. The overall loss characteristics obtained in this manner showed good agreement with the experimental values over the most useful operating range of the cascade.

9. Recommendations

Two-dimensional cascades provide a useful way to study certain phenomena that exist in turbomachinery flows because the cascade can be constructed to isolate the desired mechanism(s) in a way that is either impossible or impractical in a rotor test. Once the flow physics are understood, a mathematical model can be developed and validated against these experiments. The ultimate goal of these models, however, is to aid the design of a better turbomachine, and it is important to understand the differences between the cascade and rotor flows so that the latter can be more accurately modeled.

In a started 2-dimensional cascade, the flow is choked and the inlet flow angle is independent of the exit pressure. The downstream pressure information cannot influence the inlet flow until the passage shock is pushed forward of the blade leading edge and purely subsonic flow exists downstream. At the start/unstart point, the cascade passage shock is nearly a normal shock. It has been shown, however, that transonic fan rotors can operate with supersonic relative flow downstream of an oblique passage shock for a portion of the unchoked operating range (Pierzga and Wood, 1985; Bloch, et al., 1995).

In a rotor test there is always subsonic flow in the casing boundary layer, even when the rotor is choked. As the rotor is throttled, the downstream pressure information moves upstream through the casing boundary layer, as shown in Figure 71. Once the pressure information reaches the leading edge of the blade tip, it moves radially toward the hub in the subsonic region between the detached bow shock and the blade leading edge. It is the present author's opinion that this is the mechanism that causes the shock system to move upstream from the blade, allowing unstarted operation of the rotor. This may also be the reason why rotor loss characteristics exhibit a smooth transition between started and unstarted operation, unlike cascade characteristics which have a sharp corner at the start/unstart point, as shown in Figure 72.

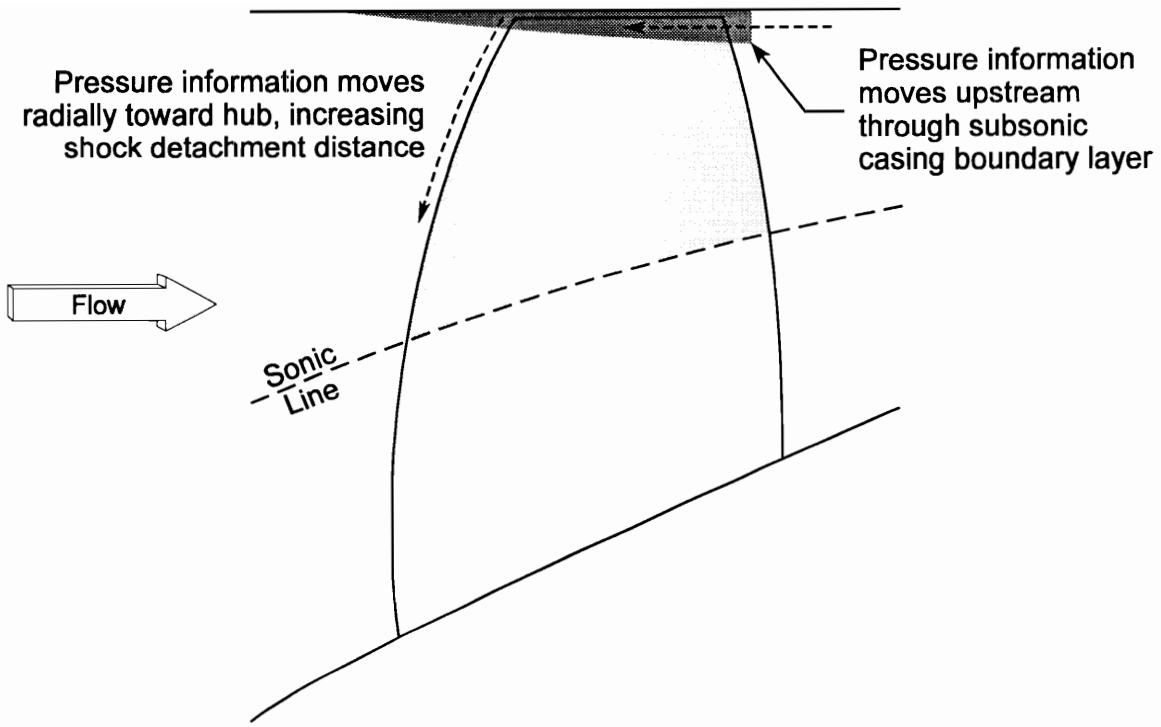

Figure 71. Influence of downstream static pressure on passage shock detachment for transonic rotor

The precise variation of shock geometry with detachment distance, Δy, is not immediately clear for rotor operation, and this needs to be investigated. The relative total pressure and relative total temperature upstream of the passage shock will no longer be constant (in general) because of the radial shift of the streamlines, and this effect must be included in a shock loss model for rotors. Furthermore, the streamtube convergence will provide some nearly isentropic diffusion upstream of the passage shock that must be considered.

Once the above effects have been included in a fully 3-dimensional shock loss model, some means must be obtained to assess the accuracy of the model. After the model has been validated, it must be incorporated into a compressor design system to allow an engineer to design for part-speed efficiency.

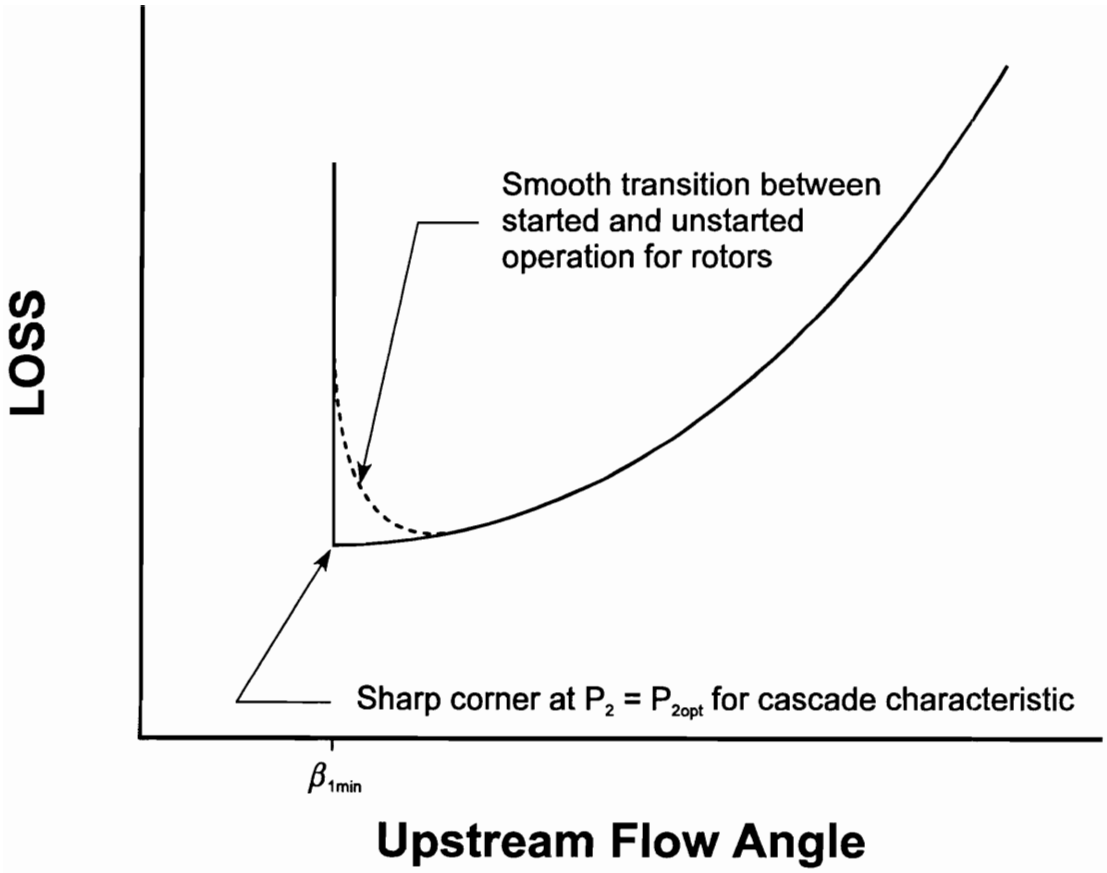

Figure 72. Fundamental difference in the shape of a cascade loss characteristic as compared to a rotor loss characteristic

References

Balzer, R. L., 1971, "A Method of Predicting Compressor Cascade Total Pressure Losses When the Inlet Relative Mach Number is Greater than Unity," ASME *Journal of Engineering for Power*, Vol. 93, No. 1, pp. 119-125.

Bloch, G. S., Copenhaver, W. W., and O'Brien, W. F., 1995, "Development of an Off-Design Loss Model for Transonic Compressor Design," AGARD CP-571, Paper 16.

Boxer, E., 1969, "A Method for Predicting the Performance of High Reaction Supersonic Compressor Blade Sections," Presented at the AIAA Fifth Propulsion Specialist Conference, Colorado Springs, CO.

Boyer, K. M., and O'Brien, W. F., 1989, "Model Predictions for Improved Recovery of a Multistage Axial-Flow Compressor," AIAA Paper 89-2687.

Broichhausen, K. D., and Gallus, H. E., 1982, "Theoretical and Experimental Analysis of the Flow Through Supersonic Compressor Rotors," AIAA *Journal* Vol. 20, No. 8 pp. 1097-1103.

Broichhausen, K. D., and Gallus, H. E., 1987, "Influence of Shock and Boundary-Layer Losses on the Performance of Highly Loaded Supersonic Axial Flow Compressors," AGARD CP-401, Paper 9.

Busemann, A., 1949, "A Review of Analytical Methods for the Treatment of Flows with Detached Shocks, NACA TN 1858.

Carman, C. T., Myers, J. R., Wennerstrom, A. J., and Steurer, J. W., 1968, "Experimental Investigation of Two Blunt Trailing Edge Supersonic Compressor Rotors of Different Blade Thickness and With Circular Arc Camber Line," AEDC TR-68-197.

Casey, M. V., 1994a, "Computational Methods For Preliminary Design And Geometry Definition In Turbomachinery," AGARD LS-195, Paper 1.

Casey, M. V., 1994b, "Industrial Use of CFD in the Design of Turbomachinery," AGARD LS-195, Paper 6.

Çetin, M., Üçer, A. Ş., Hirsch, C., and Serovy, G. K., 1987, "Application of Modified Loss and Deviation Correlations to Transonic Axial Compressors," AGARD R-745.

Chima, R. V., 1987, "Explicit Multigrid Algorithm for Quasi-Three-Dimensional Viscous Flows in Turbomachinery," AIAA *Journal of Propulsion and Power*, Vol. 3, No. 5, pp. 397-405.

Chima, R. V., March 1996, private communication.

Chima, R. V., Turkel, E., and Schaffer, S., 1987, "Comparison of Three Explicit Multigrid Methods for the Euler and Navier-Stokes Equations," NASA TM-88878.

Davis, M. W., Jr., and O'Brien, W. F., 1991, "Stage-by-Stage Poststall Compression System Modeling Technique," AIAA *Journal of Propulsion and Power*, Vol. 7, No. 6, pp. 997-1005

Denton, J. D., 1993, "Loss Mechanisms in Turbomachines," ASME *Journal of Turbomachinery*, Vol. 115, No. 4, pp. 621-656.

Denton, J. D., 1994, "Designing in Three Dimensions," AGARD LS-195, Paper 3.

Dowler, C. A., Boyer, K. M., and Poti, N., 1989, "Model Predictions of Fan Response To Inlet Temperature Transients and Spatial Temperature Distortion," AIAA Paper 89-2686.

Dunham, J., "Aerodynamic Losses in Turbomachines," AGARD CP-571, Keynote Address.

Dunker, R. J., et al., 1978, "Experimental Study of the Flow Field within a Transonic Axial Compressor Rotor by Laser Velocimetry and Comparison with Through-Flow Calculations," Transactions of the ASME , Series A, Vol. 100, p.279.

Dunker, R. J, and Hungenberg, H. G., 1980, "Transonic Axial Compressor Using Laser Anemometry and Unsteady Pressure Measurements," AIAA Journal, Vol. 18, pp. 973-979.

Dunker, R. J., 1987, "Shock Loss Model for Supercritical Subsonic Flows in Transonic Axial Flow Compressors," AGARD CP-401, Paper 27.

Erwin, J. R.; Savage, M.; and Emery, J. C., 1953, "Two-Dimensional Low-Speed Cascade Investigation of NACA Compressor Blade Sections Having a Systematic Variation in Mean-Line Loading," NACA RM L53I30b.

Freeman, C., and Cumpsty, N. A., 1992, "A Method for the Prediction of Supersonic Compressor Blade Performance," AIAA *Journal of Propulsion and* Power, Vol. 8, No. 1, pp. 199-208.

Hale, A. A., January 1996, private communication.

Herrig, L. J.; Emery, J. C.; and Erwin, J. R., 1951, "Systematic Two-Dimensional Cascade Tests Of NACA 65-Series Compressor Blades At Low Speeds," NACA RM L51G31.

Hirsch, C., and Denton, J. D., 1981, "Propulsion and Energetics Panel Working Group 12 on Through Flow Calculations in Axial Turbomachines," AGARD AR-175.

Jansen, W., and Moffatt, W. C., 1967, "The Off-Design Analysis of Axial-Flow Compressors," ASME *Journal of Engineering for Power*, Vol. 89, pp. 453-462.

Jenions, I. K., 1994, "The Role of CFD in the Design Process," AGARD LS-195, Paper 8.

Kantrowitz, A., 1950, "The Supersonic Axial-Flow Compressor," NACA Report 974.

Kim, C.-S., 1956, "Experimental Studies of Supersonic Flow past a Circular Cylinder," *Journal of the Physical Society of Japan*, Vol. 11, No. 4, pp. 439-445.

Klapproth, J. F., 1950, "Approximate Relative-Total-Pressure Losses of an Infinite Cascade of Supersonic Blades With Finite Leading-Edge Thickness," NACA RM E9L21.

Klapproth, J. F., 1954, "General Considerations of Mach Number Effects on Compressor-Blade Design," NACA RM E53L23a.

Koch, C. C., and Smith, L. H., 1976, "Loss Sources and Magnitudes in Axial-Flow Compressors," ASME *Journal of Engineering for Power*, Vol. 98, pp. 411-424.

Koch, C. C., November 1994, private communication.

Koch, C. C., 1995, "Loss Mechanisms and Unsteady Flows in Turbomachines," AGARD CP-571, Technical Evaluation Report.

Law, C. H, April 1994, private communication.

Law, C. H, and Puterbaugh, S. L., 1982, "A Computer Program for Axial Compressor Design," AFWAL TR-82-2074.

Levine, P., 1956, "The Two Dimensional Inflow Conditions for a Supersonic Compressor With Curved Blades," Wright Air Development Center TR 55-387.

Lichtfuß, H. -J., and Starken, H., 1974, "Supersonic Cascade Flow," DFVLR Sonderdruck Nummer 376, reprinted in *Progress in Aerospace Science*, Pergammon Press Ltd., Volume 15.

Lieblein, S.; Schwenk, F. C.; and Broderick, R. L., 1953, "Diffusion Factor for Estimating Losses and Limiting Blade Loadings in Axial-Flow Compressor Blade Elements," NACA RM E53D01.

Lieblein, S., 1954, "Review of High-Performance Axial-Flow Compressor Blade Element Theory," NACA RM E53L22.

Lieblein, S., 1956, "Aerodynamic design of axial-flow compressors, Volume 2; Chapter 6, Experimental flow in 2-D cascades," NACA RM E56B03a.

Lieblein, S., and Roudebush, W. H., 1956a, "Theoretical Loss Relations for Low-Speed Two-Dimensional Cascade Flow," NACA TN 3662.

Lieblein, S., and Roudebush, W. H., 1956b, "Low-Speed Wake Characteristics of Two-Dimensional Cascade and Isolated Airfoils," NACA TN 3771.

Lieblein, S., 1957, "Analysis of Experimental Low-Speed Loss and Stall Characteristics of Two-Dimensional Compressor Blade Cascades," NACA RM E57A28.

Lieblein, S., 1959, "Loss and Stall Analysis of Compressor Cascades," ASME *Journal of Basic Engineering*, Vol. 81, pp. 387-400.

Mayhew, E. R., and Eisenhauer, J. M., 1995, "Compressor Exit Temperature Analysis, Part III," AIAA Paper 95-3029.

Miller, G. R., Lewis, G. W., Hartmann, M. J., 1961, "Shock Losses in Transonic Compressor Blade Rows," ASME *Journal of Engineering for Power*, Vol. 83, pp. 235-242.

Moeckel, W. E., 1949, "Approximate Method for Predicting Form and Location of Detached Shock Waves Ahead of Plane or Axially Symmetric Bodies," NACA TN 1921.

Moeckel, W. E., 1950, "Experimental Investigation of Supersonic Flow With Detached Shock Waves for Mach Numbers Between 1.8 and 2.9," NACA RM E50D05.

Novak, R. A., 1967, "Streamline Curvature Computing Procedures for Fluid-Flow Problems," ASME *Journal of Engineering for Power*, Vol. 93, pp. 478-490.

Pianko, M., and Wazelt, F., 1983, "Propulsion and Energetics Panel Working Group 14 on Suitable Averaging Techniques in Non-Uniform Internal Flows," AGARD AR-182.

Pierzga, M. J., and Wood, J. R., 1985, "Investigation of the Three-Dimensional Flow Field Within a Transonic Fan Rotor: Experiment and Analysis," ASME *Journal of Engineering for Gas Turbines and Power*, Vol. 107, pp. 436-449.

Prince, D. C., 1980, "Three-Dimensional Shock Structures for Transonic/ Supersonic Compressor Rotors," AIAA *Journal of Aircraft*, Vol. 17, pp. 28-37.

Puterbaugh, S. L., 1994, "Tip Clearance Flow-Shock Interaction in an Advanced, Transonic, Axial-Flow Compressor Rotor," Doctoral Dissertation, University of Dayton.

Saravanamuttoo, H. I. H., and Fawke, A. J., "Simulation of Gas Turbine Dynamic Performance," ASME Paper 70-GT-23.

Schreiber, H.-A., 1980, "Untersuchungen am Verdichtergitter L 030-6 im transsonischen Machzahlbereich von M_1=0,8 bis 1,24 - Schaufelschnitt des Transsonikverdichter-Laufrades 030 bei 68% Schaufelhöhe" DFVLR IB 352-80/2.

Schreiber, H.-A., 1981, "Experimentelle Untersuchung des Verdichtergitters L030-4 mit Variation des axialen Massenstromdichteverhältnisses im transsonischen Machzahlbereich," DFVLR IB 325l4l1981.

Schreiber, H.-A., 1987, "Experimental Investigations on Shock Losses of Transonic and Supersonic Compressor Cascades," AGARD CP-401, Paper 11.

Schreiber, H.-A. and Starken, H., 1981, "Evaluation of Blade Element Performance of Compressor Rotor Blade Cascades in Transonic & Low Supersonic Flow Range," Fifth International Symposium on Airbreathing Engines, Paper 67, Bangalore, India.

Schreiber, H.-A., and Tweedt, D. L., 1987, "Experimental Investigation and Analysis of the Supersonic Compressor Cascade ARL-2DPC," DFVLR IB-325-02-87.

Smith, L. H., 1954, "A Note on the NACA Diffusion Factor," General Electric Internal Note.

Sorenson, R. L., 1981, "A Computer Program to Generate Two-Dimensional Grids About Airfoils and Other Shapes by the Use of Poisson's Equation," NASA TM-81198.

Starken, H., 1971, "Untersuchung der Strömung in ebenen Überschallverzögerungsgittern (Investigation of the Flow in Planar Supersonic Compressor Cascades)," DVFLR FB 71-99.

Starken, H., Zhong, Y., and Schreiber, H.-A., 1984, "Mass Flow Limitation of Supersonic Blade Rows Due to Leading Edge Blockage," ASME paper 84-GT-233.

Stewart, W. L., 1955, "Analysis of Two-Dimensional Compressible-Flow Loss Characteristics Downstream of Turbomachinery Blade Rows in Terms of Basic Boundary-Layer Characteristics," NACA TN 3515.

Strazisar, A. J., 1995, currently unpublished summary of the results of the ASME CFD "blind" test case presented at the 1994 IGTI conference, to be published in the ASME *Journal of Turbomachinery.*

Strazisar, A. J., and Denton, J. D., 1995, "CFD Code Assessment in Turbomachinery - A Progress Report," IGTI *Global Gas Turbine News.*

Suder, K. L., and Celestina, M. L., 1994, "Experimental and Computational Investigation of the Tip Clearance Flow in a Transonic Axial Compressor Rotor," ASME Paper 94-GT-365, Selected for publication in the ASME *Journal of Turbomachinery.*

Swan, W. C., 1961, "A Practical Method of Predicting Transonic Compressor Performance," ASME *Journal of Engineering for Power*, Vol. 83, pp. 322-330.

Tweedt, D. L., Schreiber, H. A., and Starken, H., 1988, "Experimental Investigation of the Performance of a Supersonic Compressor Cascade," NASA TM 100879.

Vuillez, C., and Petot, B., 1994, "New Methods, New Methodology: Advanced CFD in the SNECMA Turbomachinery Design Process," AGARD LS-195, Paper 7.

Wennerstrom, A. J., and Puterbaugh, S. L., 1984, "A Three-Dimensional Model for the Prediction of Shock Losses in Compressor Blade Rows," ASME *Journal of Engineering for Gas Turbines and Power*, Vol. 106, No. 2 pp. 295-299.

Wennerstrom, A. J., and Stavros, O., 1966, "A Theoretical Analysis of the Blunt-Trailing Edge Supersonic Compressor and Comparison with Experiment," ARL-66-0236.

Wolf, T., 1993, "A Comment on "Approximate Formula of Weak Oblique Shock Wave Angle"," AIAA *Journal*, Vol. 31, No. 7, p. 1363.

Vita

The author, Gregory S. Bloch, was born in Quonset Point, Rhode Island on December 17, 1963. As the son of a U. S. Navy pilot, he traveled around the country during his childhood. The author entered Virginia Polytechnic Institute in the Fall of 1981 and squeezed a four year program into eight short years, receiving his B. S. in Mechanical Engineering in May 1989.

Mr. Bloch entered the Graduate School at V. P. I. in July 1989 and received his M. S. in Mechanical Engineering in August 1991. After completion of the M. S. program, he worked at the U. S. Air Force Compressor Research Facility in Dayton Ohio for 1 year. Always a glutton for punishment, Mr. Bloch returned to the Graduate School at V. P. I. in August 1992 to pursue his Ph.D. at taxpayer expense. After completion of his course work requirements, he returned to Dayton, Ohio to conduct research at the U. S. Air Force Compressor Aero Research Laboratory.

During his first year in Dayton, Mr. Bloch met the most wonderful human being on the face of the planet and on April 9, 1994 she became Mrs. Bloch.

Upon completion of his Ph.D., the author will continue to work at the Compressor Aero Research Laboratory where he is owned by the U.S. taxpayers well into the next millennium. More importantly, however, Mr. Bloch will have the rest of his life to devote to making his wife the happiest woman in the world.

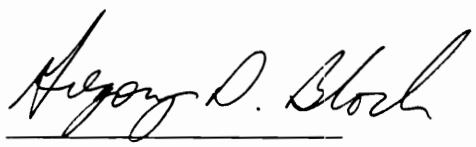

Gregory S. Bloch